Design of a Non-Scaling Fixed Field Alternating Gradient Accelerator for Charged Particle Therapy

Suzanne L. Sheehy

Lady Margaret Hall

University of Oxford

Thesis submitted in fulfilment of the requirements for the degree of Doctor of Philosophy at the University of Oxford

Trinity Term, 2010

Design of a Non-Scaling Fixed Field Alternating Gradient Accelerator for Charged Particle Therapy

Suzanne L. Sheehy, Lady Margaret Hall, University of Oxford

Thesis submitted in fulfilment of the requirements for the degree of Doctor of Philosophy at the University of Oxford

Trinity Term, 2010

Abstract

This thesis describes the design a novel type of particle accelerator for charged particle therapy. The accelerator is called a non-scaling, Fixed Field Alternating Gradient (ns-FFAG) accelerator, and will accelerate both protons and carbon ions to energies required for clinical use. The work is undertaken as part of the PAMELA project.

An existing design for a ns-FFAG is taken as a starting point and analysed in terms of its ability to suit the charged particle therapy application. It is found that this design is particularly sensitive to alignment errors and would be unable to accelerate protons and carbon ions at the proposed acceleration rate due to betatron resonance crossing phenomena.

To overcome this issue, a new type of non-linear ns-FFAG is developed which avoids resonance crossing and meets the requirements provided by clinical considerations. Two accelerating rings are required, one for protons up to 250 MeV and fully stripped carbon ions to 68 MeV/u, the other to accelerate the carbon ions up to 400-430 MeV/u. Detailed studies are undertaken to show that this new type of accelerator is suitable for the application. An alignment accuracy of 50μm will not have a detrimental effect on the beam and the dynamic aperture for most lattice configurations is found to be greater than $50\,\pi$ mm mrad normalised in both the horizontal and vertical plane.

Verification of the simulation code used in the PAMELA lattice design is carried out using experimental results from EMMA, the world's first ns-FFAG for 10-20 MeV electrons built at Daresbury Laboratory, UK.

Finally, it is shown that the described lattice can translate into realistic designs for the individual components of the accelerator. The integration of these components into the PAMELA facility is discussed.

This thesis is dedicated to Bill, whose life was tragically cut short by cancer in 2010.

Acknowledgements

"Let me tell you a story..." To my supervisor, Ken, I can't thank you enough for your advice, support and the opportunities you've thrown my way. Oh, and of course that boisterous laugh that means I can locate you from anywhere within a mile radius. I promise I will learn not to unwittingly split infinitives one day.

Thanks must go to my colleagues at Oxford, especially Holger Witte and Takei Yokoi, for their advice and support. A huge thank you to Shinji Machida, David Kelliher and the other ASTeC staff at the Rutherford Laboratory for their incredibly valuable collaboration. I would also like to thank the EPSRC who have supported this work through the PAMELA grant, and the Royal Commission for the Exhibition of 1851 for the honour of having their support for my journey in accelerator physics for the next three years.

Thank you to my good friends and colleagues at the University of Melbourne, without whose encouragement and support I would never have undertaken this challenge. Especially to Roger, Viv, Max, Dave, Bryn and the rest of the crew. Thanks to my family, especially my twin sister Megan for helping to keep me grounded; the opposite side of the Earth sure is a long way from home.

I was once told that if a relationship can withstand a PhD, it can withstand just about anything. John, you helped me to believe I could do this. Now I have, you don't have to proof read any more!

Contents

Chapter 1

Introduction

This thesis describes the development of a novel type of particle accelerator, called a non-scaling Fixed Field Alternating Gradient accelerator (ns-FFAG) and its application to Charged Particle Therapy (CPT), as part of the PAMELA (Particle Accelerator for MEdicaL Applications) project [1, 2, 3]. The most substantial original contributions to knowledge outlined in this thesis are the understanding of the effects of alignment errors in ns-FFAG lattices in Chapter 2 and the subsequent development and optimisation of a novel ns-FFAG lattice design in Chapter 3 and Chapter 4.

The introductory chapter will give a historical overview of radiation therapy and the development of CPT including clinical requirements of relevance for accelerators. The underlying physics of the treatment of patients with charged particles is reviewed and complemented by an introduction to relevant radio-biological concepts.

Chapter 2 focuses on the design of a particle accelerator for CPT. The most commonly used accelerators for CPT are synchrotrons and cyclotrons, the advantages and disadvantages of which are discussed. Recent developments in accelerator technology have produced another option for CPT, combining a magnetic field which does not vary with time, as in a cyclotron, with the strong alternating gradient focusing employed in a synchrotron; this is the ns-FFAG. An existing ns-FFAG design for CPT

is described and its sensitivity to alignment errors studied.

Results from this work prompted the development of a novel type of ns-FFAG lattice, which is covered in Chapter 3. The lattice dynamics and error sensitivities show a substantial improvement compared with the original linear ns-FFAG. This new lattice design is developed for the PAMELA project for a proton and low-energy carbon ring which would be appropriate for full energy proton CPT and biological studies using low-energy fully-stripped carbon ions. Extending this work the lattice design is scaled up to a full treatment-energy carbon ring in Chapter 4 and optimised for this scenario.

PAMELA is one of three work packages of the CONFORM (COnstruction of a Non-scaling FFAG for Oncology, Research and Medicine) project carried out by the British Accelerator Science and Radiation Oncology Consortium (BASROC). The CONFORM project also encompasses the construction of the world's first ns-FFAG, EMMA (Electron Model for Many Applications), at Daresbury Laboratory, UK. Commissioning of EMMA is ongoing and initial results from EMMA were used in the verification of the ZGOUBI simulation code, outlined in Chapter 5.

Chapter 6 concerns the integration of the PAMELA lattice design with the rest of the CPT facility from the ion source through to the rotating treatment gantry. Proposed engineering solutions for components are discussed.

1.1 Motivation for charged particle therapy

There are over 17,400 particle accelerators in the world, around half of which are used for medical applications. While the majority of medical accelerators are used to produce X-rays for radiotherapy or for radioisotope production, an increasing number are used to accelerate beams of protons and ions for the treatment of cancer using particle beams. The use of charged particle beams in cancer treatment has evolved during the

last two decades into an effective, well-established treatment method, particularly in the case of protons. However, in early treatments the particle accelerators were not designed specifically for this purpose. In many cases these were existing machines in physics laboratories, adapted for the purpose of treating patients. Naturally, from the perspective of both clinician and patient, it is preferable for this kind of treatment to take place in a hospital, rather than a laboratory. This has led to a heightened need for accelerators tailored to CPT in a hospital environment.

The worldwide total of accelerators and their applications was reviewed in 2003 by W. Maciszewski and W. Scharf [4, 5] as shown in Table 1.1. Of the accelerators for medical applications, small linear electron accelerators to produce photons for radiotherapy are by far the predominant type. These machines have been almost constantly improved since the first X-ray treatments 100 years ago, driven by developments in accelerator science which allowed for smaller, more accurate and cheaper linear accelerators for X-ray radiotherapy [6]. It is clear that progress in the design of particle accelerators can have a significant impact in delivering new developments in medicine.

Application	**Number in use**
Radiotherapy accelerators	7500
Ion implanters, modification of surfaces and matter in bulk	7000
Accelerators for industrial processing and research	1500
Low energy accelerators for research (incl. biomedicine)	1000
Medical radioisotope production	200
High energy accelerators for research (E>1GeV)	120
Synchrotron radiation sources	100
Total	>17400

Table 1.1: Applications of accelerators in the world as of 2003 [4, 5, 7]. Only accelerators with beam energies of 1 MeV or more are included.

X-ray radiotherapy is central to the cancer treatment strategies of most developed nations [8]. However, a single beam of X-rays has the fundamental disadvantage of depositing more dose in the surrounding healthy tissue than in the cancerous target

volume. While this problem has been partially overcome by the use of sophisticated delivery techniques, further improvements would be obtained by using a beam which has a better ratio between between dose deposited in cancerous tissue and unwanted dose deposited in normal, healthy cells.

This improvement can be achieved using charged particles such as protons and light ions instead of X-rays and is referred to here as 'Charged Particle Therapy' (CPT)[1]. As in the case of X-ray radiotherapy, this type of treatment requires a sophisticated particle accelerator. However, due to the nature of the particles and energies required, the accelerators for CPT are necessarily larger and more complex than those for X-ray radiotherapy.

Despite this, presently there are 33 operational facilities for CPT, including one low energy cyclotron-based facility in the UK at the Clatterbridge Centre for Oncology [9], used only for the treatment of ocular tumours. It is clear that further developments in accelerator science for CPT will necessarily improve the availability and cost effectiveness of this treatment modality.

1.2 Radiotherapy

1.2.1 Overview

In the UK more than one in three people will develop some form of cancer in their lifetime and one in four deaths is caused by cancer. These statistics are representative of cancer incidence and mortality rates in most developed countries. Thankfully, being diagnosed with cancer is no longer necessarily fatal. With current treatment methods the five year survival rate of people diagnosed with cancer is approximately 50% and the ten year survival rate has improved by a factor of two since the 1970s, to

[1]It should be noted that CPT is commonly referred to as 'hadron therapy' in Germany, Switzerland, Italy and France.

46.2% [10].

No single definitive treatment for cancer exists. Modern medicine employs many methods of treatment including surgery, radiotherapy, chemotherapy, hormone therapy, immunotherapy, gene therapy and other specialized treatments. A patient's treatment plan is selected by doctors, usually employing multiple treatment methods to achieve a greater effect. Of these methods, radiotherapy is one of the most commonly used. It is estimated that around "50% of all patients who are diagnosed with cancer in the world would currently benefit at some stage of their illness from radiotherapy" [8].

The use of ionising radiation in the treatment of cancer is not new, having a long history starting almost immediately upon the discovery of X-rays by W. Roentgen in 1895 [11]. While many advancements have been made in delivery methods over the last 100 years, all radiotherapy using X-rays is limited by the fundamental nature of the interaction of radiation with matter.

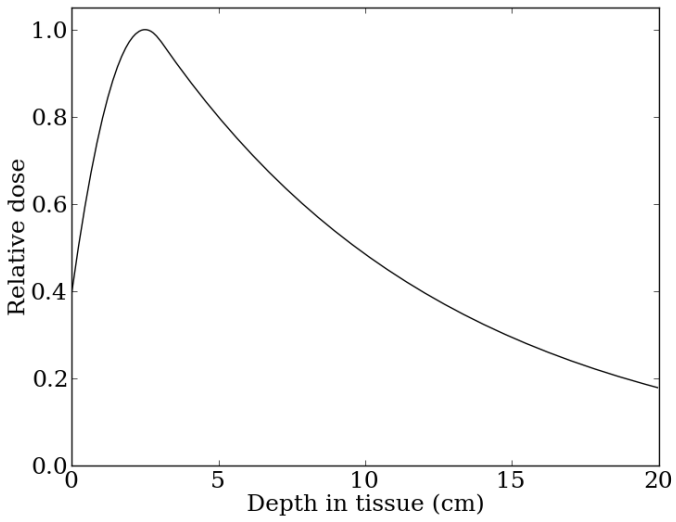

Figure 1.1: Depth-dose profile of a 20 MV X-ray radiotherapy beam.

In the case of X-rays in the MV range, that is X-rays produced by electrons with energies of more than an MeV, the interaction in tissue is dominated by Compton

scattering on loosely bound electrons [12]. The Compton effect is the most common clinical scenario, with most X-ray radiotherapy treatments being performed with beams between 6 and 20 MV. Higher energy X-rays over about 25 MV result in pair production, from which the positron ionises until it further annihilates with a free electron resulting in two lower-energy photons.

These physical effects lead to most of the energy being deposited close to the surface and an exponential attenuation thereafter, giving the depth-dose profile shown in Fig. 1.1. The main features of this distribution include a significantly larger dose on the proximal (near) side of the target volume than in the target volume itself and a considerable dose on the distal (far) side of the target volume.

1.2.2 Advances in radiotherapy

Developments in radiotherapy in the last 100 years have come from two main areas. First, an increase in computational power has led to 3D dose planning, better predictions of biological response, 3D imaging for tumour localisation and therapy monitoring. The second area involves developments in the technology used for radiotherapy, including advanced linear accelerator technology, multi-leaf collimators for automatic beam shaping and robotic patient tables for absolute positional control.

State-of-the-art treatments employ techniques known as 'Conformal Radiotherapy' (CRT) and 'Intensity Modulated Radiation Therapy' (IMRT) which are based on these developments [13]. CRT aims to tailor the region of high-dose to that of the target volume in the patient, while maintaining a relatively low dose in surrounding healthy tissue. The shape of the beam of radiation is determined by using a multi-leaf collimator in addition to employing multiple beams. This allows the shape of the radiation beam to match the profile of the tumour volume from the specific angle of irradiation, resulting in a reduction of radiation to the surrounding normal tissues. Going one step further, IMRT involves modulation of the beam intensity in order to

conform the dose more precisely to the target tumour volume.

The use of CRT and IMRT with advanced treatment planning utilising multiple beams has refined the use of radiotherapy to deliver the best possible treatment with this type of radiation. Further significant improvements may only be achievable with the use of a different type of radiation: in particular the use of charged particles.

1.3 Charged particle therapy

1.3.1 History

It was not until the development of particle accelerators which could produce protons of the order 150 to 400 MeV that the first proposal of the application of charged particles to the treatment of cancer was made. This occurred in 1946 when R. R. Wilson published the first proposal of CPT in the medical journal Radiology, commenting that with this new technology for higher energy protons "it must have occurred to many people that the particles themselves now become of considerable therapeutic interest"[14].

Prior to this, in 1904, Bragg and Kleeman had discovered that, unlike X-rays, protons and other light charged ions deposit most of their energy at the very end of their range, exhibiting a so-called Bragg peak. It was this property of the interaction of protons and ions with tissue which R. R. Wilson was keen to exploit, as he saw the potential to increase damage to cancerous tissue, while reducing damage to healthy tissue.

A typical depth-dose distribution of protons in tissue (adapted from [15]) is shown in Fig. 1.2. The main features of the distribution include a relatively small dose as the beam enters the tissue in the so-called 'plateau region', a large dose deposition at a precise depth (the Bragg peak) determined by the incoming beam energy and little or no dose in the region beyond the Bragg peak. These features are common

to all charged particle beams including protons (p^+), helium (He^{2+}), carbon (C^{6+}) and neon (Ne^{10+}), but excluding electrons (e^-) which interact in a similar manner to photons due to their high charge to mass ratio. Throughout this thesis charged particle beams should be taken to mean fully stripped ions unless otherwise stated.

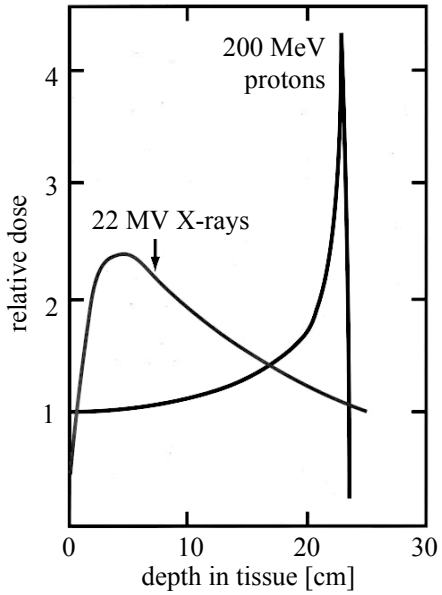

Figure 1.2: Relative depth-dose distribution of photon (X-ray) radiation compared with proton CPT. The depth at which the Bragg peak occurs is dependent on the energy of the incoming proton beam.

1.3.2 Physics of charged particle therapy

The Bragg peak is caused by the relationship between the charged particle's energy loss and the square of its velocity. Most of the particle's energy is lost in collisions with atomic orbital electrons in the tissue, however, due to the heavy mass of the particle, its path remains straight as small interactions cause it to slow down and eventually stop. This process is described in the relativistic regime by the Bethe-Bloch formula in Eqn. 1.1.

$$-\frac{dE}{dx} = \frac{4\pi}{m_e c^2} \cdot \frac{nZ^2}{\beta^2} \cdot \left(\frac{e^2}{4\pi\epsilon_0}\right)^2 \cdot \left[\ln\left(\frac{2m_e c^2\beta^2}{I \cdot (1-\beta^2)}\right) - \beta^2\right] \tag{1.1}$$

where $\beta = v/c$, x is the distance travelled by the particle, n is the electron density of the target, I is the mean excitation potential of the target and all other symbols have their usual meanings. The electron density of the material can be found using Eqn. 1.2, where ρ is the density of the material, Z, A are the atomic number and mass number of the material and N_A is the Avogadro number.

$$n = \frac{N_A \cdot Z \cdot \rho}{A} \tag{1.2}$$

In practice this means that a proton beam of 250 MeV will penetrate tissue to a depth of around 34 cm.

1.3.3 Terminology of radiobiological performance measures

The efficacy of CPT as a treatment modality relies on not only the physical interaction of charged particles in tissue, but also the biological response of cells to this type of radiation. The radiobiological performance measures relevant to CPT are outlined here. For clarity, these concepts are directly compared with the equivalent concept in physics.

Dose in gray (Gy) and gray equivalent (GyE)

The gray is an SI unit which describes the absorbed radiation dose in matter due to ionising radiation such as X-rays. It corresponds to the absorption of one joule of energy by one kilogram of matter.

$$1 \text{ Gy} = \frac{1 \text{ J}}{\text{kg}} = 1 \text{ m}^2 \cdot \text{s}^{-2} \tag{1.3}$$

The dose in gray represents only the absorbed dose and does not give an accurate representation of the equivalent dose in biological tissue when radiation other than

X-rays is used. This equivalent dose is instead measured[2] in gray equivalent (GyE) as in Eqn. 1.4, where 'RBE' is the Relative Biological Effectiveness.

$$1\text{GyE} = \text{RBE} \cdot 1\text{Gy} \tag{1.4}$$

Relative Biological Effectiveness (RBE)

The biological effects of charged particle therapy differ substantially from those of X-ray radiotherapy. Charged particles directly damage the DNA of cancer cells, which are more vulnerable than normal cells to DNA damage. This leads to the fraction of cells surviving a given dose of X-irradiation being higher than for the same dose of charged particles [16]. This difference is characterised by the 'Relative Biological Effectiveness' or RBE. The RBE is specific to the beam used and is a key indicator of the performance of a radiological treatment method.

Due to the large amount of clinical experience with X-rays, the gray equivalent (GyE) is used in CPT treatment plans to describe the prescribed dose delivered to the patient. In the case of X-ray radiotherapy, an RBE of 1.0 is given as a standard against which to measure other treatment modalities. The RBE of charged particles such as protons, helium ions, carbon ions and others is always $\geq$1.0. Generally, a value of 1.1 is used for the RBE of protons. For carbon ions the RBE is more difficult to determine, but in practice a value of 3 is usually adopted [17]. This higher RBE for carbon leads to an increased probability of tumour control in addition to the benefit of a conformal dose distribution.

Linear energy transfer (LET)

The energy loss of charged particles in matter is governed by the Bethe formula of Eqn. 1.1. This is a measure of the energy loss of the incident particle rather than

[2]The sievert (Sv) is the same as GyE.

the energy gained by the absorbing medium. The Linear Energy Transfer (LET) in radiobiology refers to the energy gained by the absorbing medium per unit track length of the incident charged particle [16].

In radiobiology, particle species generally fall into one of two categories: high-LET and low-LET radiation. Low-LET includes photons and light charged particles including both electrons and protons. High-LET is generally considered to include fully stripped helium (He^{2+}), carbon (C^{6+}), oxygen (O^{8+}), neon (Ne^{10+}) and other ions of greater atomic number.

The biological mechanisms of cell damage for high and low-LET radiation will not be discussed here. However, in practice the principal difference between the two types of LET radiation is the cell survival as a function of dose. As shown in Fig. 1.3 (data from Ref. [18]), the surviving fraction of cells for low-LET radiation is higher than for the equivalent dose of high-LET radiation.

The LET is not a constant for a particular particle, and increases as the velocity of the particle decreases towards the end of its range. The region of maximum energy transfer is the Bragg peak. As the LET increases, the RBE also changes. The region in which the RBE is increased is specific to each type of particle, as shown in Fig. 1.4 (see Refs. [19, 20] for original data).

The clinical implementation of CPT relies on accurate experimental data tables of RBE, LET and Bragg peak depths in order to develop precise treatment plans for each patient.

1.3.4 CPT facility layout

CPT requires many different components in addition to the accelerator, each of which needs to be carefully considered in planning a new facility. Naturally, spaces in the facility are required to house patient facilities such as consultation rooms and imaging facilities, and for administration and training areas. These will not be considered here.

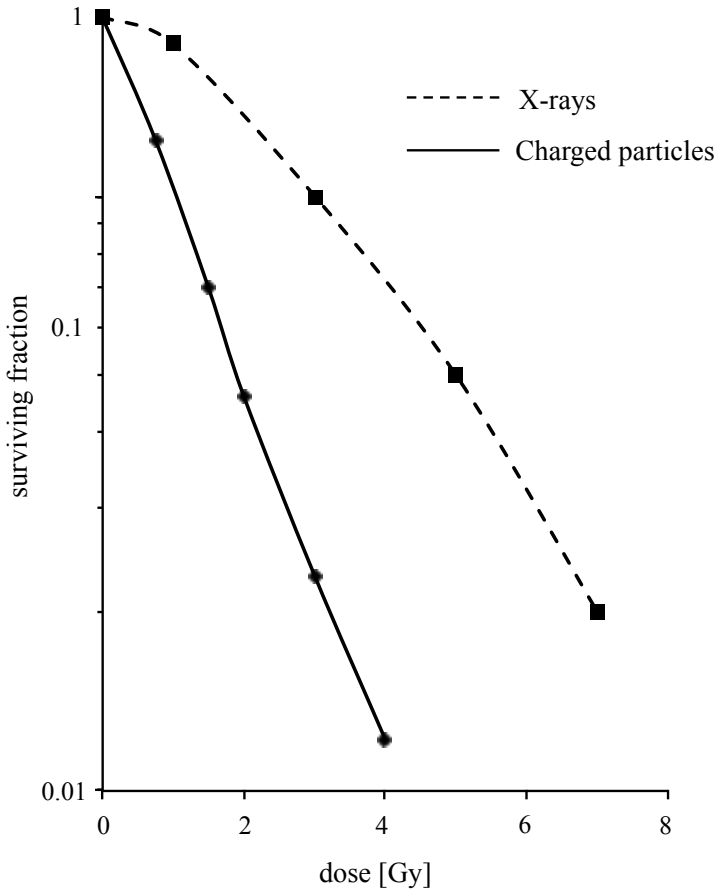

Figure 1.3: Cell survival as a function of dose for low-LET (X-rays) and high-LET charged particles (C^{6+}). A higher relative biological effectiveness per unit dose is achieved by using high LET radiation.

For the facility hardware, space must be available for the injector and injection beam lines, the accelerator, extraction beam lines and transport and finally a number of rotating gantries or fixed beam-lines for patient treatment. Fixed beam-lines are usually either horizontal or vertical and a facility commonly has at least one of each in order to reach a good range of tumour irradiation angles with minimal movement of the patient treatment table. A rotating gantry allowing full 360° flexibility of beam entrance angles requires a greater level of technological complexity, but provides superior flexibility in treatment planning and implementation. An example of such a facility is the IBA proton therapy centre [21] shown in Fig. 1.5. A view of the inside of a gantry room, in which patients are treated at the Paul Scherrer Institute

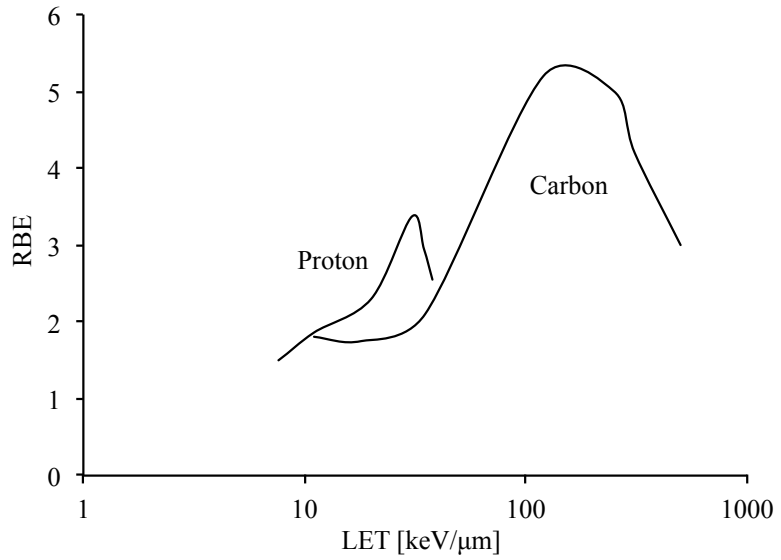

Figure 1.4: Relative biological effectiveness (RBE) as a function of linear energy transfer (LET) for protons and carbon ions. The maximum RBE for protons occurs at a lower LET than for carbon and the average RBE for carbon is higher than that for protons. RBE is calculated at a dose of approximately 2 Gy.

in Switzerland [22] is shown in Fig. 1.6.

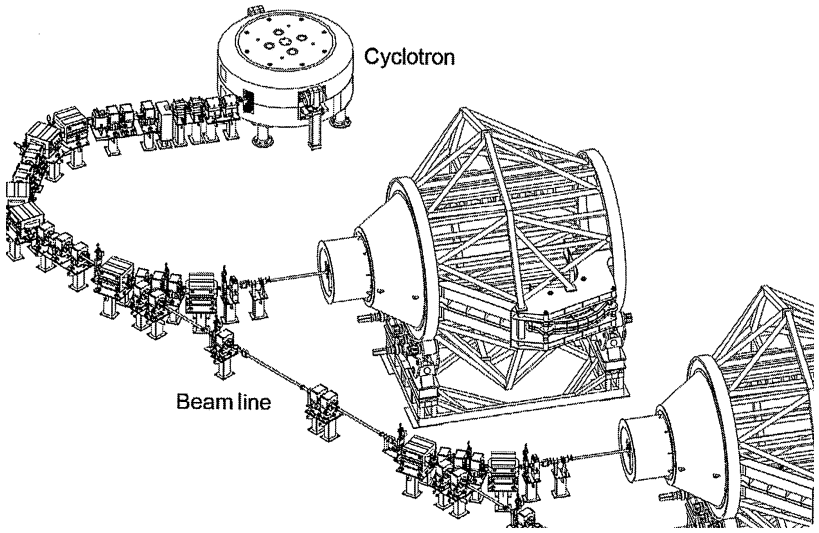

Figure 1.5: Possible layout of the IBA proton therapy centre for a cyclotron based CPT facility. Copyright 2006 IBA.

Figure 1.6: The gantry room of the proton therapy facility at the Paul Scherrer Institute (PSI) in Switzerland. Image courtesy of PSI.

1.3.5 Irradiation techniques

There are two main techniques of irradiation which can broadly be described as 'passive spreading' and 'active scanning'. Choosing an irradiation technique is of critical importance to the accelerator design. In particular the active scanning technique requires a highly flexible accelerator which can provide variable energy beams, whereas the passive spreading technique can be performed with a fixed energy machine. The most commonly used technique in current facilities is that of passive spreading, but the trend for future facilities is toward active scanning due to its superior dose conformation and lack of patient specific hardware [16].

Passive spreading technique

Proton or ion beams of a single energy display a Bragg peak which is too narrow to be used in treatment without modification [13]. Such beams must undergo two separate stages of modification; range modification and passive spreading.

A range modifier has the effect of spreading out the Bragg peak in depth, creating

the so-called 'Spread out Bragg Peak' (SOBP). This range spreading is achieved by using a rotating device with variable thickness of plastic, similar to that shown in Fig. 1.7. The resultant SOBP depth dose profile is shown in Fig. 1.8 and achieves a plateau of uniform dose which is designed to cover the target area depth-wise while sparing unwanted dose to nearby healthy tissues. The fact that this device is rotating means that the tumour can be treated in multiple layers. In some cases further use of patient specific hardware such as absorbers shaped to the treatment region, as in Fig. 1.9, can achieve a superior conformation to the tumour.

The second stage of modification, passive spreading, involves using scattering foils to adjust the size of the beam in addition to collimators and apertures which further assist in providing a dose which is highly conformed to the tumour shape in the lateral plane. By creating the SOBP and using the scattering system, the field of the beam is large enough in area to treat the entire tumour, or a significantly large part of it, in multiple layers to conform to the 3D shape of the tumour.

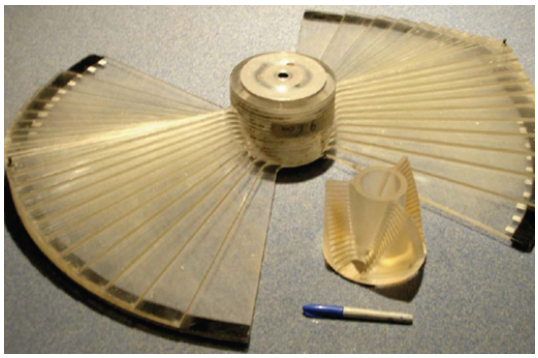

Figure 1.7: An example of a range modulator. The plastic modulator has a step-like structure in order to reduce the penetration depth of the Bragg peak to form the SOBP.

However, concerns exist about the use of passive spreading techniques. One of the major objections involves the production of neutrons in the scattering system which may provide an unwanted dose to the patient [23]. Solutions to this issue have been proposed involving the use of collimators [24], however a solution which avoids the production of neutrons entirely by actively changing the beam energy and position

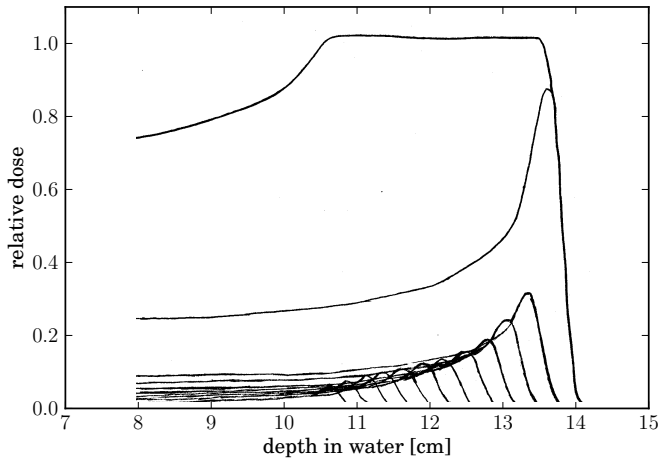

Figure 1.8: Depth-dose profile of the SOBP formed by the superposition of multiple Bragg peaks.

would be superior.

Active scanning technique

A major recent advance in CPT is the use of active beam scanning, usually in the form of spot scanning [25]. In this technique, the charge of the proton or ion beam is utilised to enable magnetic scanning of small 'pencil beams' of particles in order to 'paint' the tumour in three dimensions. For dose planning the volume is divided into small fixed volume elements known as 'voxels' (volumetric pixels). In the spot scanning method the beam is repeatedly moved to a static position before the dose is delivered to the target voxel with a defined energy. This results in an extremely accurately conformed dose to the tumour, and requires no patient specific hardware, which is seen as a significant advantage over passive scattering.

In analogy to IMRT, the feasibility of using rotating gantries to achieve intensity modulated proton therapy (IMPT) has recently been developed at PSI in Switzerland [22]. This has been shown to provide superior dose distributions to the equivalent IMRT [26].

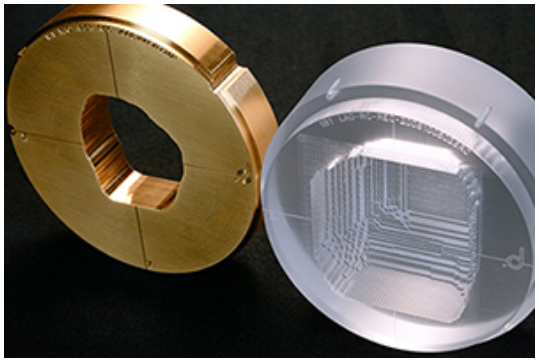

Figure 1.9: (Left) An example of a patient-specific collimator. This is designed to shape the proton beam to the shape of the tumour. (Right) A 'bolus', designed to shorten the range of the incoming beam of protons to suit the treatment plan. An intricate pattern is machined into the perspex according to the shape of the tumour. Image courtesy of .decimal, Inc.

1.3.6 Current status of CPT

To date, more than 70,000 patients have been treated with protons and light ions [27]. Initially, this treatment was only available at laboratories which hosted appropriate accelerators, but over the last 20 years there have been several CPT centres built in major hospitals, particularly in the US and Japan. The UK was a pioneer in the field of proton therapy, opening the Clatterbridge Centre for Oncology in 1989 [9]. Worldwide CPT facilities as of December 2009 given by the Particle Therapy Co-Operative Group [27] and the number of patients treated are listed in Table 1.2.

The field of CPT is undergoing rapid expansion, with 22 new facilities currently in the planning stage. Of these, 5 are in Germany, 4 are in the USA, there are 2 in both the Slovak Republic and Italy and the remaining 9 are in France, Switzerland, Austria, Sweden, Russia, Taiwan, Japan, China and South Africa.

1.4 Clinical requirements for accelerators

The PAMELA design envisages a next-generation CPT solution for both protons and carbon ions, incorporating active spot scanning technology in order to ensure the

Location	**Country**	**Part.**	**Max. K.E. (MeV)**	**Start**	**Total no. pts.**	**Date of total**
ITEP, Moscow	Russia	p	250	1969	4162	Jul-09
St.Petersburg	Russia	p	1000	1975	1353	Dec-09
PSI, Villigen	Switz.	p	72	1984	5300	Dec-09
Dubna	Russia	p	200	1999	595	Dec-09
Uppsala	Sweden	p	200	1989	929	Dec-08
Clatterbridge	UK	p	62	1989	1923	Dec-09
Loma Linda CA.	USA	p	250	1990	14000	Oct-09
Nice	France	p	65	1991	3935	Dec-09
Orsay	France	p	200	1991	4811	Dec-09
iThemba Labs	South Africa	p	200	1993	511	Dec-09
MPRI(2) IN.	USA	p	200	2004	890	Dec-09
UCSF CA.	USA	p	60	1994	1200	Dec-09
HIMAC, Chiba	Japan	ion	800/u	1994	4504	Feb-09
TRIUMF, Vancouver	Canada	p	72	1995	145	Dec-09
PSI, Villigen	Switz.	p	250	1996	542	Dec-09
G.S.I. Darmstadt	Germany	ion	430/u	1997	440	Nov-09
HZB (HMI), Berlin	Germany	p	72	1998	1437	Dec-09
NCC, Kashiwa	Japan	p	235	1998	680	Dec-09
HIBMC,Hyogo	Japan	p	230	2001	2382	Nov-09
HIBMC,Hyogo	Japan	ion	320/u	2002	638	Nov-09
PMRC(2), Tsukuba	Japan	p	250	2001	1586	Dec-09
NPTC, MGH Boston	USA	p	235	2001	4270	Oct-09
INFN-LNS, Catania	Italy	p	60	2002	174	Mar-09
Shizuoka	Japan	p	235	2003	852	Dec-09
WERC,Tsuruga	Japan	p	200	2002	56	Dec-08
WPTC, Zibo	China	p	230	2004	977	Dec-09
MD Anderson Cancer Center, Houston, TX	USA	p	250	2006	1700	Dec-09
FPTI, Jacksonville, FL	USA	p	230	2006	1847	Dec-09
NCC, IIsan	South Korea	p	230	2007	519	Dec-09
RPTC, Munich	Germany	p	250	2009	78	Dec-09
Oklahoma City, OK	USA	p	230	2009	21	Dec-09
HIT, Heidelberg	Germany	p	250	2009	treatment started	Nov-09
HIT, Heidelberg	Germany	ion	430/u	2009	treatment started	Nov-09
UPenn, Philadelphia	USA	p	230	2010	treatment started	Jan-10
GHMC, Gunma	Japan	ion	400/u	2010	treatment started	Mar-10

Table 1.2: Currently operating CPT centres worldwide including patients treated [27].

best possible treatment method is delivered. This thesis will focus on the delivery of protons (p^+) and fully stripped carbon ions (C^{6+}) for two reasons; these are the species which have the most clinical experience and carbon, being one of the lightest of the 'heavy' ion species available, would require a smaller accelerating ring than O^{8+}, Ne^{10+} or any heavier species and so represents a compromise between radiobiological effectiveness and the required technology. These clinical requirements have been developed into a set of parameters which the machine must be able to deliver, which are given in Table 1.3.

In addition to the requirements which come from clinical considerations, the accelerator must be suitable for use in a hospital environment. This imposes a number of constraints on the design which must be considered from the outset.

1. In order to ensure that treatment plans can be accurately followed, the system must be extremely reliable. The overall facility requires an availability of greater than 95%. The accelerator itself needs to have an availability of around 99% or greater. If this availability is not obtained down time of the treatment system can cause undesirable breaks in patient treatment plans.

2. The facility must be easy to operate and maintain. The number of staff required to run the accelerator must be minimised and ideally the machine should be a 'turn-key' solution, which is highly reliable and simple in its operation.

3. Hospitals often have restricted space available, therefore the overall facility should be kept as small as possible.

4. The cost of the machine should be kept to a minimum.

The implications of these requirements together with the clinical requirements given in Table 1.3 are addressed in terms of accelerator design in Chapter 2.

Parameter		**Value**	**Units**	**Comment**
Extraction energy (proton)	Min	60	MeV	30 mm depth
	Max	250	MeV	340 mm depth
Extraction energy (carbon)	Min	110	MeV/u	30 mm depth
	Max	400-430	MeV/u	230-300 mm depth
Energy step (protons)	at E_{Min}	5	MeV	2mm step size
	at E_{Max}	1	MeV	
Energy step (carbon)	at E_{Min}	15	MeV/u	2mm step size
	at E_{Max}	6	MeV/u	
Energy resolution (FWHM)	at E_{Min}	3.5	%	
	at E_{Max}	1.8	%	
Voxel Size	Min	$4 \times 4 \times 4$	mm	
	Max	$10 \times 10 \times 10$	mm	
Clinical Dose rate (protons)	Min	2	Gy/min	
	Max	≥ 10	Gy/min	
Clinical Dose rate (carbon)	Min	2	Gy/min	
	Max	≥ 10	Gy/min	
Cycle rate		≈ 1	kHz	
Bunch charge (protons)		1.6	pC	
Bunch charge (carbon)		0.3	pC	
Bunch charge stability		< 10	%	100 pulses/voxel give <1% dose accuracy

Table 1.3: Clinical requirements relevant to accelerator design for the PAMELA project [2, 3]. Depths are given for ICRU striated muscle [28].

Chapter 2

Accelerator physics challenge

The design of an accelerator for a CPT facility should be driven by the clinical requirements outlined in Section 1.4. Taken individually the 1 kHz cycle rate, extremely high reliability, multiple particle species, variable energy extraction or small accelerator footprint are all within the reach of current technology. However, taken simultaneously these requirements pose a significant challenge to the accelerator physics community. This chapter outlines existing accelerator technologies used for CPT, including the advantages and disadvantages of each type. A new accelerator called a non-scaling Fixed Field Alternating Gradient accelerator (ns-FFAG) is introduced, which is expected to be able to meet all the requirements of CPT simultaneously. The ns-FFAG is discussed in more detail and its feasibility as a CPT accelerator is studied.

2.1 Existing accelerator technology

Beam energies required for therapy are relatively low; up to 1 GeV compared to the multi-TeV energy range required for high energy physics experiments. As such, these energies can be achieved with a number of different types of accelerator including synchrotrons, cyclotrons and linacs. Due to the limited space available in a clinical

environment, a circular accelerator is usually chosen as the main accelerator for a CPT facility. While there have been recent developments such as the 'Cyclinac' design [29, 30], linear accelerators are not considered here. There are a number of choices of circular accelerator. Most existing or planned facilities use the established technologies of either a synchrotron or cyclotron, both of which are discussed in more detail below.

2.1.1 Cyclotrons

First conceived by Lawrence in 1929 [31], the fixed-frequency cyclotron uses a vertical magnetic guide field, B, which is constant in time, together with a fixed frequency for acceleration. The particles to be accelerated are produced by an ion source in the centre of the machine and are given an accelerating kick each time they cross between the two D-shaped electrodes, as shown in the diagram of the Lawrence Cyclotron in Fig. 2.1 from Lawrence's original patent [32]. The RF frequency matches the cyclotron frequency, f_c of Eqn. 2.1, which is constant for non-relativistic particles [33].

$$f_c = \frac{qB}{2\pi m} \tag{2.1}$$

where q and m are the charge and mass of the accelerated particle and B is the magnetic field strength. Focusing in the vertical direction is produced by a horizontal field component which arises near the edge of the cyclotron magnets, which can also be seen on the right-hand drawing in Fig. 2.1. To ensure vertical stability at all radii, the magnetic field must in practice be reduced slightly toward the outer edge of the cyclotron.

The fixed magnetic field of a cyclotron leads to the particles spiralling radially outward as they gain energy until they are extracted at a particular radius, corresponding to a defined energy. The particle trajectories are constantly being bent in

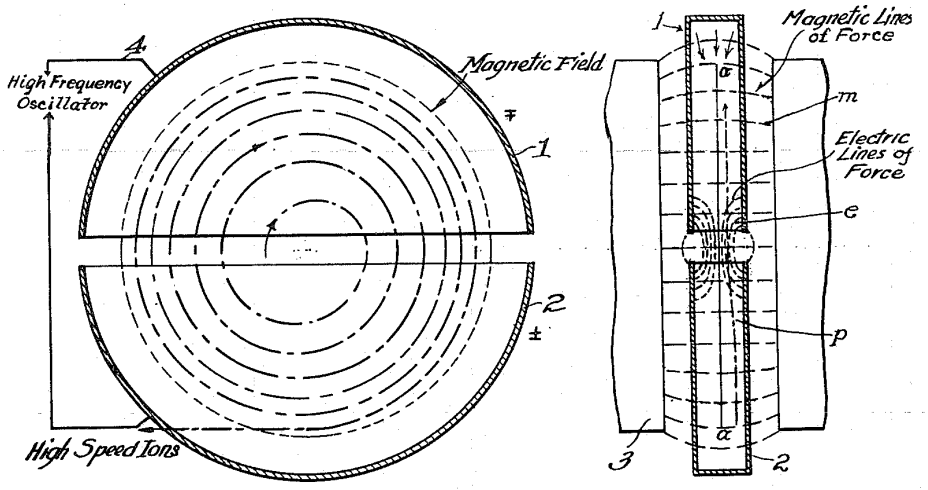

Figure 2.1: Diagram of the operation of the Lawrence Cyclotron.

the magnetic field. This constant bending with no long straight sections makes the cyclotron very compact and so a natural choice for a hospital based accelerator. However, the energy reach of fixed-frequency cyclotrons is limited due to particle orbits and RF fields losing synchronicity at relativistic velocities.

It should also be noted that while these accelerators have a relatively small footprint, high energy cyclotrons require extremely large volumes of iron for the yoke, which introduces technical and manufacturing difficulties, as well as making them expensive.

To counteract this, AVF (Azimuthally Varying Field) cyclotrons employ an azimuthally varying field in the form of additional pole pieces at periodic azimuthal positions or through the use of separated [34] or spiral [35, 36] sectors. This azimuthally varying field introduces additional horizontal field components, enhancing vertical focusing and allowing for increased beam currents. These cyclotrons go some way to counteract relativistic effects, particularly in the case of the isochronous cyclotron, in which the particles have a constant revolution frequency.

Further developments include the synchrocyclotron, employing a variable frequency RF field to allow synchronisation with the particle orbits into the relativistic

regime. This machine is cyclic in nature rather than providing a quasi-continuous beam like the fixed-frequency cyclotron. It is generally seen as a precursor to the synchrotron for this reason.

Industrial 'turn-key' cyclotron solutions exist for proton therapy, such as the IBA C235 [21, 37]. Developments are underway to create carbon ion cyclotron solutions, for example the IBA C400 [38], although no solution is commercially available at present. As an example of the issue of magnetic yoke volume, the yoke required for the C400 cyclotron has a weight of over 700 tonnes, which may make the machine expensive when compared to other solutions.

Another important consideration is the cyclotron's fixed extraction energy. For CPT this means that the beam energy must be adjusted between the accelerator and the patient using an energy degrader as discussed in Section 1.3.5. The cyclotron provides ample current to enable sufficient dose to the patient. However, the losses produced by passive scattering lead to concerns about activation and radiation protection in such a facility.

2.1.2 Synchrotrons

The idea of an accelerator consisting of a ring of pulsed magnets came from the Australian physicist Marcus Oliphant in 1943 [39], followed by the discovery of the phase stability principle in 1944 independently by Veksler [40] and McMillan [41, 42]. Original synchrotrons were of the weak-focusing variety. In this kind of synchrotron transverse focusing in the vertical (y) direction is achieved by introducing a field with a gradient $0 < n < 1$ with respect to the radial direction r, where

$$n = \frac{-r}{B}\frac{\partial B_y}{\partial r}. \tag{2.2}$$

Modern synchrotrons employ the principle of alternating-gradient or 'strong' fo-

cusing [43, 44] in which alternating focusing and defocusing magnets lead to much stronger focusing forces in the transverse plane than in constant-gradient weak-focusing synchrotrons.

This alternating-gradient focusing is also employed in another type of accelerator, the FFAG, which will be dicussed in Section 2.1.5. The differences between the alternating-gradient synchrotron and the FFAG accelerator are primarily in the transverse beam dynamics. Some key concepts in transverse dynamics of alternating-gradient accelerators are introduced here.

2.1.3 Transverse dynamics

In the following discussion of transverse dynamics, the reference frame shown in Fig. 2.2 is adopted, where the s-axis is in the beam direction, the z-axis is tangential to the beam direction, the x-axis is in the horizontal transverse direction and the y-axis is in the vertical transverse direction. The radial direction, r, points directly away from the centre of the circular accelerator. Angles of rotation are defined as ψ, the angle of roll about the z-axis, θ, the angle of rotation about the y-axis and ϕ, the angle of rotation about the x-axis.

FODO lattice: In an alternating-gradient synchrotron, the magnets are arranged into a series of cells, many of which may be identical. Together this pattern of cells around the ring forms the so-called accelerator lattice. A common cell structure for an alternating gradient synchrotron is the 'FODO' lattice, consisting of a focusing (F) quadrupole, a straight drift section (O), a defocusing quadrupole (D) and a further drift section (O). It should be noted that an F quadrupole focuses in the horizontal direction and defocuses in the vertical, while the D quadrupole does the opposite. The combination of F and D focuses in both planes. This structure produces the strong focusing effects characteristic of alternating-gradient synchrotrons. Bending

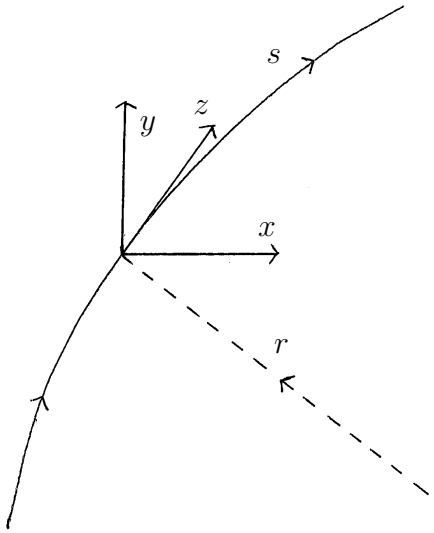

Figure 2.2: Reference frame.

is provided by dipole magnets inserted into the drift (O) sections in appropriate locations around the accelerator.

Hill's equation: The transverse motion in an alternating-gradient accelerator consisting of ideal dipole and quadrupole components is termed 'linear' motion, and is governed by Hill's equation. For a particle of ideal energy, Hill's equations in the horizontal (x) and vertical (y) planes, with respect to the beam direction (s) are given in Eqn. 2.3.

$$\begin{aligned} x'' + K_x(s)x = 0 \\ y'' + K_y(s)y = 0 \end{aligned} \tag{2.3}$$

Where the following definitions apply for positive charged particles [45]:

$$x' = \frac{dx}{ds}, y' = \frac{dy}{ds}$$
$$K_x = \rho^{-2} - \frac{B'}{B\rho}, K_y = \frac{B'}{B\rho} \tag{2.4}$$
$$B' = \frac{\delta B_y}{\delta x}$$

where ρ is the bending radius of a magnet, defined as the radius of an arc described by a charged particle traversing the magnet. With the condition of periodicity on the focusing functions over a period of length L, $K_{x,y}(s+L) = K_{x,y}(s)$, the solution to Hill's equation in each plane (neglecting the subscripts x, y) for $K > 0$ is of the form:

$$x = \sqrt{\beta(s)\epsilon}\,\cos[\phi(s) + \phi_0] \tag{2.5}$$

From Eqn. 2.5 it is clear that the motion in a linear system which obeys Hill's equation is similar to that of simple harmonic motion with both a constant amplitude component $\sqrt{\epsilon}$ corresponding to the emittance of Eqn. 2.11 and a varying amplitude component $\sqrt{\beta(s)}$, with a phase, $\phi(s)$ which is a function of distance around the ring and related to β (see next section) by Eqn. 2.6. The full derivation of the solution of Hill's equation can be found in Refs. [45, 46] among others and is discussed in more detail in Chapter 3.

$$\phi(s) = \int \frac{ds}{\beta(s)} \tag{2.6}$$

Betatron tune: Particles in an alternating gradient circular accelerator undergo oscillating trajectories in both the horizontal and vertical directions, known as betatron oscillations. The phase of the oscillating trajectory advances around the machine, and the number of oscillations per turn is called the betatron tune of the accelerator, Q, defined in Eqn. 2.7.

$$\oint_C \frac{ds}{\lambda(s)} = \frac{1}{2\pi} \oint_C \frac{ds}{\beta(s)} = Q \tag{2.7}$$

where Q is the machine tune, C is the machine circumference, s is in the direction of the beam, λ is the wavelength of the oscillations and β is the betatron function describing the oscillations [46]. The cell tune, ν is the phase advance per cell, corresponding to the machine tune Q divided by the number of cells.

Chromaticity: Chromaticity, $\xi(p)$ is defined as the change in cell tune, $\Delta\nu$ with momentum, p, as in Eqn. 2.8, where p_0 is a reference momentum and $\delta p = p - p_0$.

$$\Delta\nu = \xi(p)\frac{\delta p}{p_0} \tag{2.8}$$

There exists a natural chromaticity produced by the quadrupoles of the standard FODO lattice [45], given in Eqn. 2.9.

$$\xi^{\text{FODO}}_{\text{natural}} \approx -\frac{1}{4\pi} N\left(\frac{\beta_{\max}}{f} - \frac{\beta_{\min}}{f}\right) = -\frac{\tan(\phi/2)}{\phi/2}\nu \approx -\nu \tag{2.9}$$

where N is the number of cells in the lattice, f is the focal length of the focusing magnets and ϕ and ν are the phase advance and betatron tune per cell, respectively. $\beta_{\max}$ and $\beta_{\min}$ are the maximum and minimum values of the betatron function in the cell.

Dispersion: Dispersion, $D(p, s)$ describes the change in horizontal particle position with momentum. For a change in momentum, δp such that $p = p_0 + \delta p$, the change in particle position is

$$x(s) = D(p, s)\frac{\delta p}{p_0}. \tag{2.10}$$

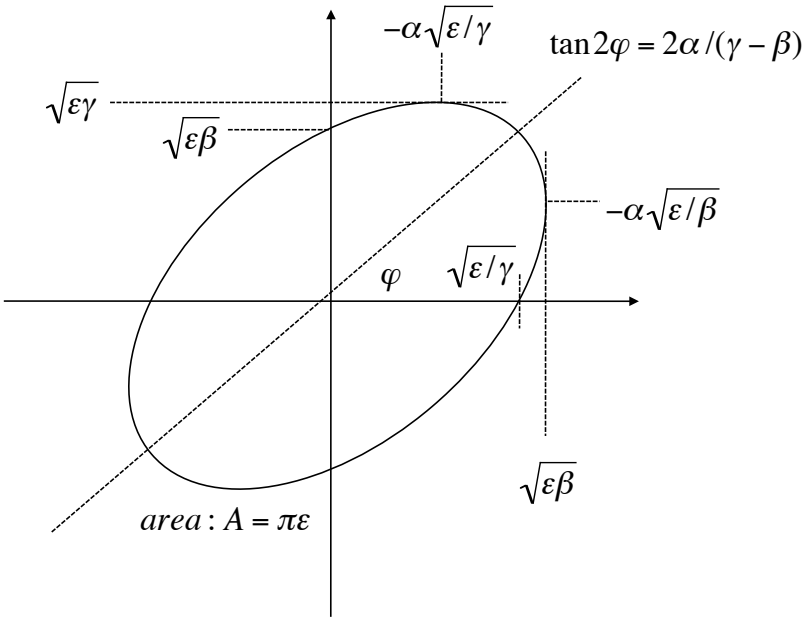

Figure 2.3: Emittance ellipse with dimensions in terms of β, α, γ and ϵ.

Emittance: The emittance ϵ is the phase space area occupied by the beam, usually given in units of π mm mrad. Various definitions exist depending on the fraction of the beam contained in the phase space. The definition used throughout this work is the RMS emittance, which can be calculated from particle phase space co-ordinates (x, x'), as in Eqn. 2.11.

$$\begin{gathered} \epsilon_{rms} = \sqrt{\langle x^2\rangle\langle x'^2\rangle - \langle xx'\rangle^2} \\ \langle x^2\rangle = \beta\epsilon, \qquad \langle x'^2\rangle = \gamma\epsilon, \qquad \langle xx'\rangle = -\alpha\epsilon. \end{gathered} \tag{2.11}$$

The corresponding ellipse in phase space (called the Courant-Snyder invariant) is of the form $\gamma(s)x^2 + 2\alpha(s)xx' + \beta(s)x'^2 = \epsilon$, where the dimensions of the ellipse in phase space at a point s along the beamline can be described by the β, γ and α functions together with the emittance ϵ as in Fig. 2.3 [47]. The quantities β, γ and α are referred to as the Twiss parameters.

As the beam size adiabatically shrinks with increase in momentum, for proton beams the normalised emittance is normally quoted. The normalised emittance is an adiabatic invariant and is given by $\epsilon_N = \gamma\beta.\epsilon$, where in this case γ and β refer to the

relativistic quantities.

Action variable (J): Hill's equation can be derived from a pseudo-Hamiltonian as in Eqn. 2.12.

$$H = \frac{1}{2}x'^2 + \frac{1}{2}K(s)x^2 \tag{2.12}$$

where (x, x') are the phase space co-ordinates and $K(s)$ is the focusing function discussed earlier. As the solution to Hill's equation is known it can be shown [45, p. 57] in terms of the conjugate action variable $\mathbf{J}$ that

$$\begin{aligned} x = &\quad \sqrt{2\beta\mathbf{J}}\cos\phi \\ x' = &\quad -\sqrt{\frac{2\mathbf{J}}{\beta}}\left[\sin\phi + \alpha\cos\phi\right] \end{aligned} \tag{2.13}$$

where ϕ is the phase, β is the Twiss parameter of Eqn. 2.6 and $\alpha = -\frac{1}{2}\frac{d\beta(s)}{ds}$. Thus the action $\mathbf{J}$ is

$$\mathbf{J} = \frac{1}{2\pi}\oint x'\,dx. \tag{2.14}$$

In a similar way to the emittance, there is an area enclosed by an invariant torus of $2\,\pi\,\mathbf{J}$. It can be seen that $\mathbf{J}$ corresponds to a kind of 'single particle emittance' and is expressed in terms of π mm mrad in a similar way to the emittance. This can be used to track single particles to determine the dynamic aperture of an accelerator, discussed in Chapter 3.

Resonances: In a real accelerator magnet positions, field strengths and gradients all have associated errors which are distributed around the lattice. Hill's equation can be used to calculate the closed orbit with errors by integrating all the orbit kicks provided by dipole errors or quadrupole errors. The integrand of this equation can

be expanded as a Fourier series, resulting in simple poles at all integer harmonics for dipole errors, and at half-integer harmonics for quadrupole errors.

These simple poles are resonances, and may produce both orbit disortion and distortion of the optical functions. The strongest resonances occur when the total betatron tune of the machine approaches an integer ($Q_{x,y} = 1, 2, 3 \dots$) or half-integer ($Q_{x,y} = 0.5, 1.5, 2.5 \dots$). Resonances can also occur at any point where $\mathrm{p}\, Q_x - \mathrm{m}\, Q_y = \mathrm{n}$, where p, m and n are all integers. Generally, the strongest resonances are integer resonances, with higher-order resonance producing a progressively weaker effect.

In a synchrotron the betatron tune is kept constant at a 'working point', chosen to avoid resonances, and the lattice will have a corresponding working diagram which represents both the chosen working point and gives an indication of the nearby resonances. An example of such a diagram for the Super Proton Synchrotron (SPS) at CERN is shown in Fig. 2.4.

2.1.4 Alternating-gradient synchrotrons

Alternating-gradient synchrotrons have a number of key differences from cyclotrons. The magnets provide strong alternating-gradient focusing and may be either combined function, with focusing and bending occurring in the same magnet, or separated function magnets. The magnetic field is ramped during acceleration to maintain particle orbits at the same radius. This has the effect of significantly decreasing the size of the required beam pipe and magnet apertures, so the synchrotron becomes a ring with small aperture magnets, very different in appearance to a cyclotron. A further key difference is in the RF acceleration. Particles which are not in the ultra-relativistic regime traversing the same radius will arrive at different times when their energies (and thus velocities) are increased. To ensure the RF cavities continue to accelerate the beam, the RF frequency must also be ramped during acceleration, in strict synchronisation with the magnetic field increase and particle velocity increase.

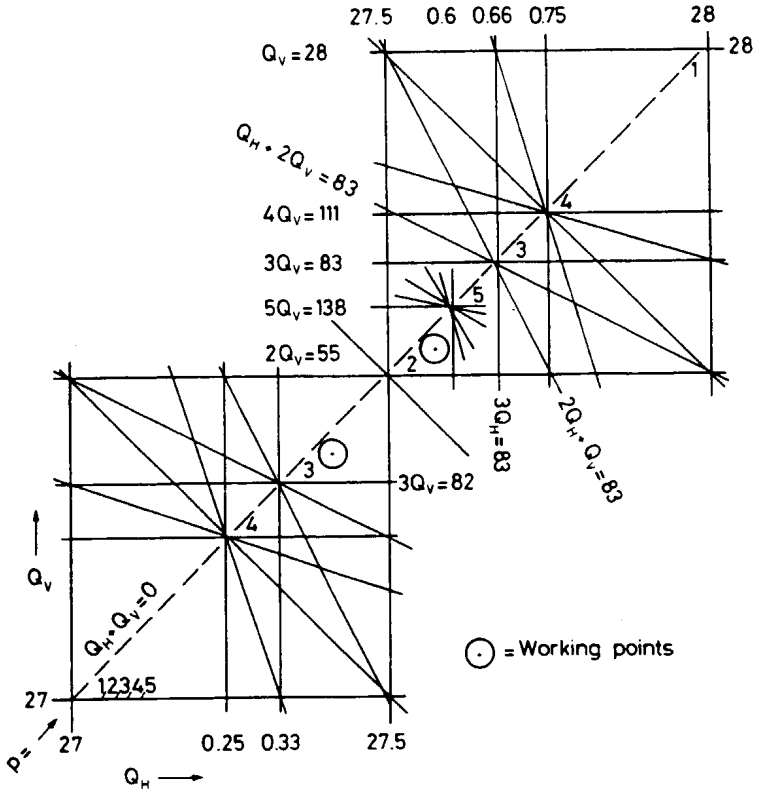

Figure 2.4: Resonance lines in Q_{H} and Q_{V} space for the SPS. Image courtesy of E. Wilson.

The synchrotron is a natural choice for a facility which provides both protons and ions for therapy as its flexibility means it can accelerate multiple particle species. However, it typically has a much larger footprint than a cyclotron [48]. Despite its larger size, a number of features make the synchrotron a suitable accelerator for CPT.

Variable energy extraction is possible on a cycle-to-cycle basis at a rate of around 1 Hz. In the case of a rapid cycling synchrotron this may be increased to about 60 Hz. Slow resonant extraction, where a third order resonance is induced to cause a controlled particle loss into the extraction line, is used to increase the beam extraction time. This enables fast active transverse scanning of the tumour during this period, removing the need for the passive scattering equipment required in the case of the cyclotron.

There are two 'turn-key' industrial solutions which use synchrotrons. Hitachi provide the PROBEAT^{TM} synchrotron which has a radius of 3.66 m and operates at 0.5 Hz producing protons of variable energy from 70 to 250 MeV [49]. Hitachi are in the design stages of a system which can provide carbon ions [50]. The synchrotron for this system has a radius of around 9.55 m to provide C^{6+} up to 480 MeV per nucleon and protons to 250 MeV. Their competitor in the current market is Siemens, who are in the process of building a synchrotron 10.35 m in radius, designed to fulfil a contract in Marburg, Germany [51]. This machine will provide C^{6+} up to 430 MeV per nucleon and protons to 250 MeV at a repetition rate defined by the ramping speed of < 1 s and extraction time of < 10 s.

In addition to 'turn-key' industrial solutions, a number of synchrotron based CPT centres exist or are being constructed which have been developed by research laboratories or collaborations. In Europe a few of these include the HIT synchrotron in Heidelberg [52] based on pioneering work at GSI [53] and synchrotrons based on the CERN PIMMS report [48] at CNAO in Italy [54] and at MedAustron in Austria [55].

2.1.5 Scaling FFAGs

The synchrotron and cyclotron are two types of circular accelerator, but not the only two. In general, there are four main types of circular accelerator, classified by the type of guide field they use: fixed-field constant-gradient (conventional cyclotrons, synchrocyclotrons and microtrons), pulsed-field constant-gradient (weak-focusing synchrotrons and betatrons), pulsed-field alternating-gradient (AG synchrotrons), and fixed-field alternating-gradient (FFAG) [56].

The fourth variety, FFAG accelerators were proposed in the early 1950s independently by T. Ohkawa in Japan [57], K. R. Symon and D. W. Kerst in the United States [58], and A. A. Kolomensky in Russia [59]. Symon and Kerst proposed "a type of circular accelerator with magnetic guide fields which are constant in time, and which can accommodate stable orbits at all energies from injection to output energy". It was suggested that due to the time-independent magnetic field the FFAG would be simpler to construct and operate while accommodating a larger beam current than conventional synchrotrons.

The key feature of the magnetic field of the FFAG is the increase in value of the vertical magnetic field with radius. The particular shape of the field is given by the r^k law of Eqn. 2.15, which describes the increase in field with radius r with respect to a reference radius r_0, where the field increase is characterised by the field index, k.

$$B_y = B_0\left(\frac{r}{r_0}\right)^k \tag{2.15}$$

Shaping the magnetic field profile in this way ensures that the shape of the particle orbits remains constant while the size of the orbits 'scales' with energy, such that each higher energy orbit is a geometrically similar enlargement of the lower energy orbits, as derived by Kolomensky [56]. Due to these properties this type of FFAG is referred to as the 'scaling' variety.

A number of scaling FFAGs were constructed in the late 1950s following these proposals, including three different electron accelerators at the Midwest Universities Research Association (MURA) [60, 61]. Proton FFAGs were not constructed at this time, as high energy physics demanded the higher energies accessible with synchrotrons rather than the improved performance of the FFAG.

In recent years, interest in FFAGs for their improved performance has increased dramatically. Specifically, their performance in terms of rapid acceleration combined with a very large beam acceptance could make them a potential solution for the acceleration of muons for either a muon collider or a neutrino factory [62, 63]. Their large beam acceptance, comparatively high energy reach and the reliability of having fixed field magnets also attracted the attention of proponents of accelerator driven sub-critical reactors. This renewed interest led to the construction of the first proton scaling FFAG at the KEK laboratory in Japan, shown in Fig. 2.5 [64, 65], as well as a 150 MeV proton FFAG [66], a 10 MeV proton FFAG at KURRI [67] and a prototype for an accelerator driven subcritical reactor [68].

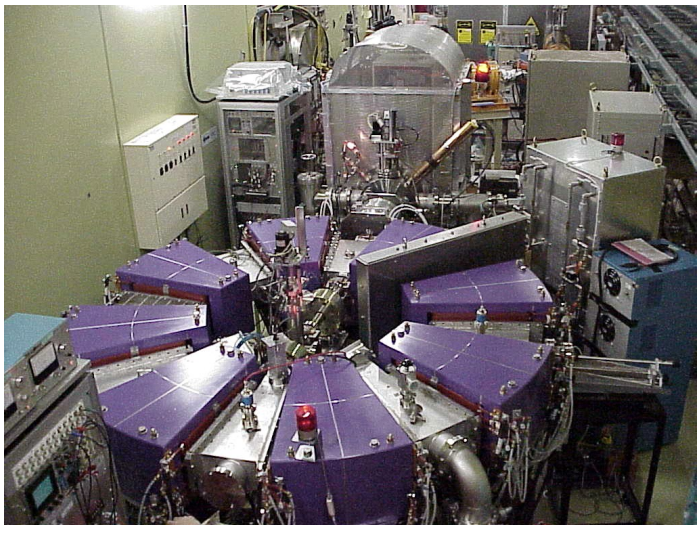

Figure 2.5: The first proton FFAG, the PoP (Proof of Principle) FFAG at KEK Laboratory in Japan. Image courtesy of KEK.

One of the disadvantageous properties of this type of FFAG is the increasing orbit radius with energy. This means that the scaling FFAG needs large aperture magnets

and RF systems, usually in excess of 1 m in horizontal bore. The magnets are also complex in nature, particularly in the case of spiral-sector FFAGs. A prototype magnet for the RACCAM project, a spiral-sector FFAG for medical applications, is shown in Fig. 2.6. These components are considered to be very expensive, which would have to be taken into account when considering the use of a scaling FFAG as a therapy machine.

Figure 2.6: The RACCAM spiral FFAG prototype magnet. Image courtesy of LPSC Grenoble.

In 1999 a new variety of FFAG was proposed, known as a non-scaling FFAG or ns-FFAG [69]. This proposal recognised that the strict magnetic scaling law of the FFAG could be relaxed, reducing the orbit shift with energy and providing new possibilities for the development of accelerators for CPT and other applications.

2.2 Non-scaling FFAGs

The ns-FFAG allows the strict scaling law of the original FFAG to be relaxed, which allows non-similar orbit shapes resulting in a much smaller change in orbit size during acceleration as shown in Fig. 2.7 (adapted from Ref. [70]). The simplest form of the ns-FFAG requires only quadrupoles with a radial offset, dramatically simplifying the required magnets.

This relaxation of the scaling law also produces non-trivial changes in the beam dynamics of the accelerator. The main difference in beam dynamics between a 'scal-

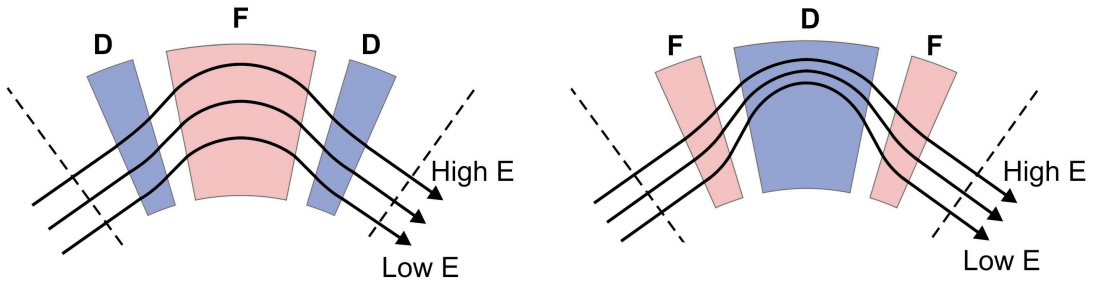

(a) (b)

Figure 2.7: (a) Scaling FFAG with similar orbit shapes, large orbit excursion and constant tune. (b) Non-scaling FFAG with non-similar orbit shapes, smaller orbit excursion and varying betatron tunes. Image courtesy of CERN Courier July/August 2004.

ing' and a 'non-scaling' FFAG is the variation of the betatron tune with energy. In a scaling FFAG or a synchrotron the tune is designed to be constant in order to avoid the crossing of resonances that may lead to beam deterioration or beam loss. In the ns-FFAG the tune is allowed to vary dynamically, crossing through both integer and half-integer betatron resonances. This intentional resonance crossing is discussed further in Section 2.3.2.

2.2.1 Requirements of a ns-FFAG for CPT

As discussed in Chapter 1, the irradiation method of choice in CPT is spot scanning. This method uses a pencil beam to irradiate a small fixed volume called a voxel. In order to implement spot scanning, Intensity Modulated Particle Therapy (IMPT) will be used to form a uniform dose field. It is estimated that a scanning speed of 100 voxel/sec will be required, setting the repetition rate of the accelerator at around 1 kHz.

Further requirements arise from Table 1.3, the most notable of which is the required energy range of protons and carbon ions for therapy. The lattice design is also required to minimise the overall footprint of the accelerator while ensuring that

sufficient drift space is available for RF cavities, injection and extraction systems, corrector magnets and diagnostics.

2.3 Existing ns-FFAG design proposals

An existing design for a ns-FFAG for CPT by E. Keil, A. Sessler and D. Trobjevic can be found in the literature [71] and will be referred to here as the KST lattice design. This lattice is a suitable starting point for studies for PAMELA and consists of three concentric rings, where each ring is a linear ns-FFAG lattice as shown in Fig. 2.8. For the purpose of looking at the general properties of this design, the second ring is taken to be representative of the complex.

This is the simplest type of ns-FFAG, the linear version, consisting of F (horizontal focusing) and D (horizontal defocusing) quadrupoles, providing alternating gradient (F/D) strong focusing. In this lattice, F and D doublet magnets are proposed in which a radial offset between the F and D quadrupoles provides the dipole bending field, removing the need for separate dipole magnets. The lattice of the second ring comprises 48 FD doublet cells.

For simulation purposes the lattice is modelled as quadrupole magnets with the radial offset described by a dipole field component. Lattice parameters are outlined in Table 2.1 and the cell layout shown in Fig. 2.9. The simulation code MAD-X [72] is used for initial studies, while the highly accurate code ZGOUBI [73] is used for acceleration tracking studies.

The magnets are rectangular in shape, and magnetic fringe fields are described using the Enge model [74], given in Eqn. 2.16, where $F(R, \theta)$ is the fringe field coefficient. F is dependent on the radial co-ordinate and the azimuthal angle θ within the magnet, as the ZGOUBI magnet description is in polar co-ordinates.

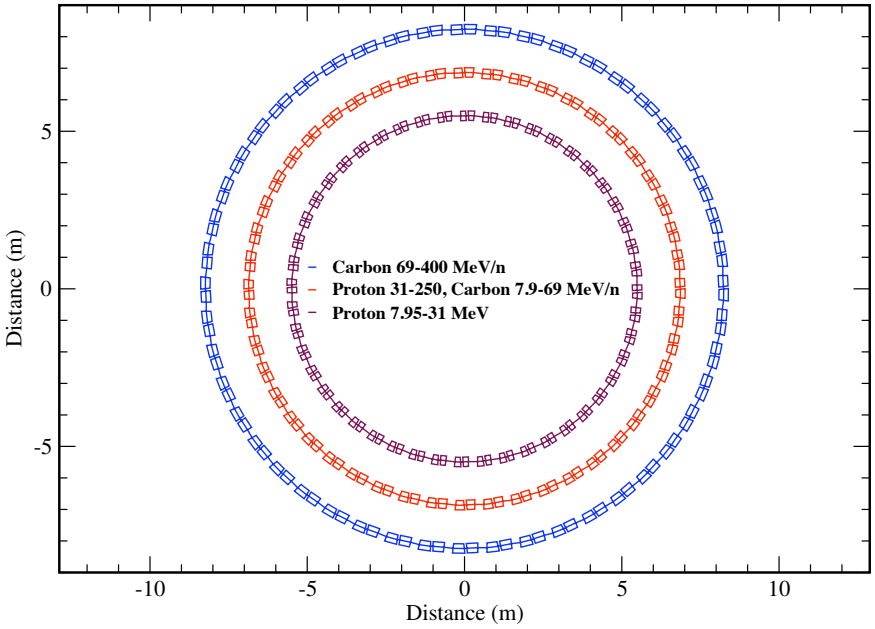

Figure 2.8: Layout of the proposed KST facility with 3 concentric ns-FFAG accelerating rings. Copyright 2007 The American Physical Society.

$$F(R,\theta) = \frac{1}{1+\exp P(d)}. \tag{2.16}$$

$P(d)$ is given in Eqn. 2.17, where d is the distance to the edge of the magnet description and depends on (R,θ). Further details of this description can be found in Ref. [75].

$$P(d) = C_0 + C_1\left(\frac{d}{g_0}\right) + C_2\left(\frac{d}{g_0}\right)^2 + C_3\left(\frac{d}{g_0}\right)^3 + C_4\left(\frac{d}{g_0}\right)^4 + C_5\left(\frac{d}{g_0}\right)^5 \tag{2.17}$$

where in this instance a half-gap height of $g_0 = 0.03$ m is used with coefficients: $C_0 = 0.1455, C_1 = 2.2670, C_2 = -0.6395, C_3 = 1.1558, C_4 = C_5 = 0$.

The β-functions and dispersion in one cell of this lattice with no alignment or gradient errors, as calculated with MAD-X [72], are shown in Fig. 2.10 with a linear representation of the F quadrupole, D quadrupole and RF cavity layout.

A key feature of linear ns-FFAG accelerators is the variation of the betatron tune

Parameter	**Injection**	**Reference**	**Extraction**
Proton Kinetic Energy [MeV]	30.95	118.38	250
C^{6+} Kinetic Energy [MeV/u]	7.84	30.98	68.36
Bρ [Tm]	0.81071	1.62142	2.43213
Cells	48		
r_0 [m]	6.875		
Magnet length (F/D) [m]	0.26 / 0.27		
Bend angle (F/D) [rad]	-0.1149 / 0.2458		
Quadrupole strength K (F/D) [m^{-2}]	9.56 / -10.74		
Half gap height [m]	0.03		
Long drift [m]	0.29		
Short drift [m]	0.08		
Orbit excursion [m]	0.065		

Table 2.1: Lattice parameters for the KST lattice.

with energy, in contrast to a synchrotron or scaling FFAG where the tune is designed to remain constant. This changing tune will cross through integer and half-integer betatron resonances, where any errors in the lattice will result in small kicks to the beam which will build up with each subsequent turn, potentially damaging the beam. The cell tune variation throughout acceleration in this lattice is shown in Fig. 2.11.

A proton/ion ns-FFAG achieves acceleration in around 1000 turns, which is fast compared to a synchrotron, through still much slower than a muon or electron ns-FFAG, which operate with around 20 turns. Studies of such accelerators for muons [63] indicate that provided acceleration is fast enough, the resonances encountered during acceleration can be crossed without damaging the beam. However, these effects in a proton/ion ns-FFAG with a slower acceleration rate and higher number of turns may be more significant.

To study the feasibility of such a ns-FFAG, alignment and field errors are analysed using two methods. The first studies are at a fixed energy without acceleration, which allows the natural effect of errors to be ascertained without the influence of resonance crossing. The second study then accounts for resonance crossing during acceleration, giving an indication of the severity of the resonance crossing and an idea of tolerances

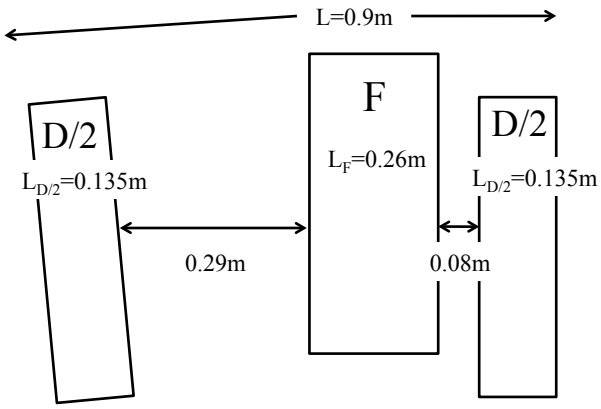

Figure 2.9: Layout of one cell of the KST lattice from centre to centre of the D magnets in two adjacent cells.

on magnet alignment and field errors.

2.3.1 Non-acceleration studies

Orbit and optical distortion sources

Orbit and optical distortions arise from errors in the accelerator components in a linear ns-FFAG. These errors may be classified into two sources; alignment errors and field errors.

Alignment errors of quadrupoles will introduce dipole magnetic field components, which will produce closed orbit distortion. The probable maximum closed orbit excursion due to dipole field errors, when caused by N displaced quadrupoles [33] is:

$$\langle \Delta x(s) \rangle = \sqrt{\beta(s)} \frac{\sqrt{N \langle \beta(s_i) \rangle}}{2\sqrt{2}\,\sin(\pi Q)} \langle \theta_i \rangle \tag{2.18}$$

where the dipole error at the i-th magnet, $\theta_i = (Kl)_i \delta x_i$ is caused by the displacement by δx_i of a quadrupole of length l and strength K. The average $\langle\ \rangle$ is understood to be the RMS value.

Quadrupole field errors can produce pertubations in the optical functions. The

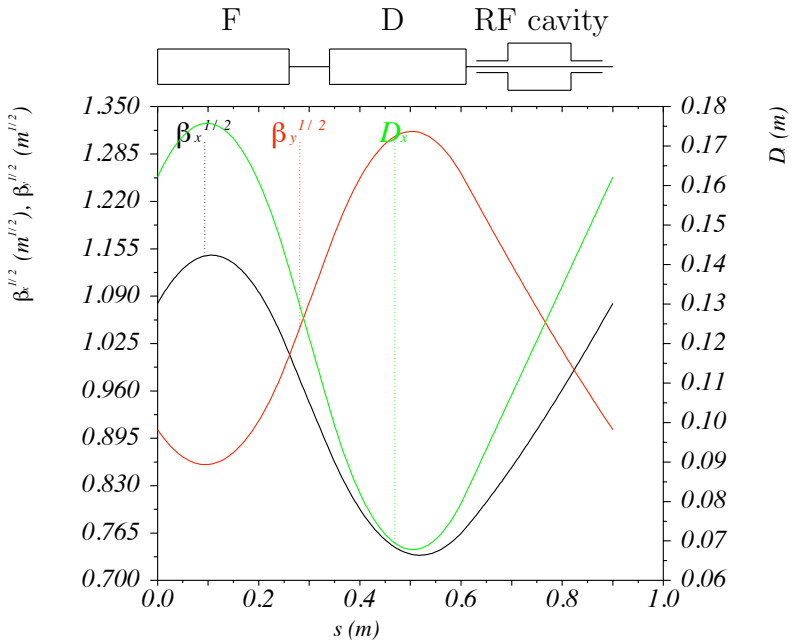

Figure 2.10: Beta functions and dispersion in model lattice at reference energy (118 MeV).

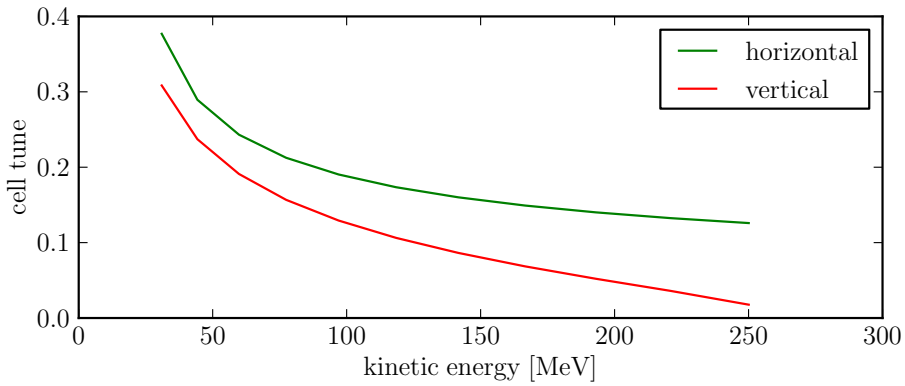

Figure 2.11: Variation of cell tunes in linear ns-FFAG as calculated with ZGOUBI.

change to the β-function from N quadrupole errors can be approximated by [33]:

$$\frac{\Delta\beta(s)}{\beta(s)} \approx \frac{N\langle\Delta Kl\rangle\langle\beta(s)\rangle}{2\sin(2\pi Q)} \tag{2.19}$$

This will result in a betatron tune change $\Delta Q = Q - Q_0$ for a small gradient error ΔK of:

$$\Delta Q = \frac{1}{4\pi}\oint \beta(s)\Delta K(s)ds \tag{2.20}$$

Closed orbit distortion due to alignment errors

Two hundred patterns of alignment errors are applied to the lattice. The errors are Gaussian distributed with a cut-off at 3σ, with a different random value applied to each of the 48 F/D pairs. The same alignment error (in magnitude and direction) is applied to both members of each pair, as it is reasonable to assume that 2 magnets mounted on a single support would have this property. The closed orbit is then calculated for each lattice, and the closed orbit distortion defined as the maximum deviation of the closed orbit from that of the error free lattice.

In order to quantify the effect of these alignment errors on the closed orbit, the maximum closed orbit distortion for each error pattern was plotted, and the resulting distribution fitted with a linear function. The amplification factor, A, as introduced in [63] is used to quantify the magnitude of orbit distortion.

$$\mathrm{A} = \frac{\langle\ \text{Orbit distortion [mm]}\ \rangle}{\langle 1\sigma\ \text{Alignment Error [mm]}\rangle} \tag{2.21}$$

The largest closed orbit distortion in the horizontal (x) direction is produced by a direct misalignment of the magnets along the x-axis, and similarly in the vertical (y) direction. The x and y amplification factors for each alignment error and the combination of all 6 types of alignment error are shown in Table 2.2, and an example of

the fitted distribution for alignment errors in the x (horizontal) direction in Fig. 2.12. Note that in the case of angle errors in ϕ, θ and ψ, the error is in mrad.

For comparison, the theoretical value calculated for A_x from Eqn. 2.18, given that $\sqrt{\beta(s)} = 0.95$ [m$^{1/2}$], $N = 48$, $\langle\sqrt{\beta(s_i)}\rangle = 0.73$ [m$^{1/2}$], $Q_x = 8.515$ at the reference momentum, $K = -9.6948$ [m^{-2}] and $l = 0.27$ [m], gives $A_x = 4.45$, which is in good agreement with the MAD-X model, as expected.

Error type	$\mathbf{A}_x$	$\mathbf{A}_y$
x	4.40	0.00
y	0.01	4.56
s	0.93	0.00
ϕ	0.00	0.48
θ	0.58	0.00
ψ	0.01	1.00
Combined	4.60	5.05

Table 2.2: Closed orbit distortion caused by alignment errors

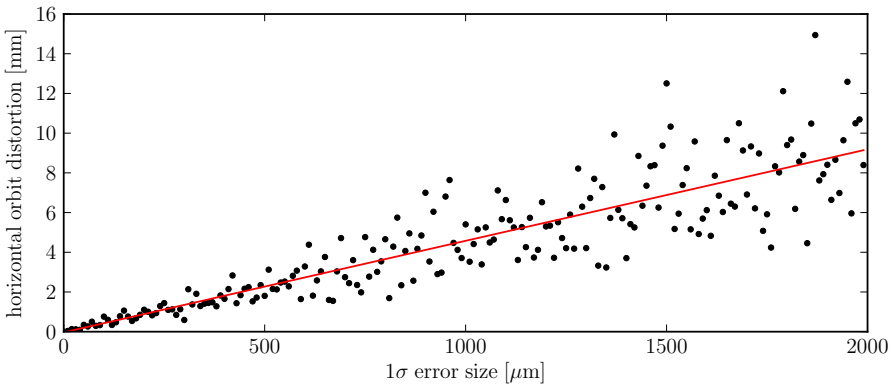

Figure 2.12: Fitted distribution of horizontal closed orbit distortion of 200 lattices with horizontal alignment errors.

Closed orbit distortion due to dipole errors

Closed orbit distortion can also be induced by errors in the dipole field of the magnets. The majority of the bending field is provided in the D quadrupoles due to the beam centre being off-axis.

To study the effect of dipole field errors, 200 random patterns of dipole errors were introduced to the D quadrupoles in the lattice, and the resulting closed orbit distortion studied. Dipole field errors are specified as the integrated field strength, $\int K.ds$, and in this case the dipole error amplification factor is defined as in Eqn. 2.22. The result in this case is $\mathrm{A(dipole)}_{\mathrm{orbit}} = 16.0$ for the horizontal direction, and 0 as expected in the vertical direction.

$$\mathrm{A(dipole)}_{\mathrm{orbit}} = \frac{\langle \text{Orbit distortion [mm]} \rangle}{\langle 1\sigma \int \Delta K.ds \rangle} \tag{2.22}$$

Optical distortion due to field errors

Dipole errors can also induce distortion of optical functions such as the tune and β-functions in the accelerator. In order to quantify the optical distortion caused by field errors in the magnets, the amplification factor is redefined as the average relative deviation of the optical parameter with errors, from its original value (with no errors) with respect to the average integrated field error.

$$\mathrm{A}_{\mathrm{optic}} = \frac{\langle \Delta\beta/\beta_0 \rangle}{\langle 1\sigma \int \Delta K.ds \rangle} \tag{2.23}$$

Results for dipole field errors are shown in Table 2.3.

	$\mathbf{A_{optic}}(\beta)$	$\mathbf{A_{optic}}(Q)$
x	330.3	0.9
y	19.6	2.4

Table 2.3: Optical distortion of the β-function and machine tune (Q) caused by dipole errors.

An additional cause of optical distortion in the lattice will be quadrupole gradient errors. In the accelerator model used quadrupole errors and dipole errors are intrinsically linked, however in other models they need not be. As a result these errors have been studied independently for completeness. When modelling quadrupole gradient

errors, the F and D magnets are allowed independent errors, in this study specified as the integrated field gradient, $\int K\,ds$. Results for quadrupole field errors are shown in Table 2.4.

	$\mathbf{A_{optic}}(\beta)$	$\mathbf{A_{optic}}(\nu)$
x	259.1	0.2
y	36.6	0.4

Table 2.4: Optical distortion of the β-function and cell tune (ν) caused by quadrupole errors

Discussion of non-acceleration studies

The non-acceleration orbit distortion study indicates that the dominant cause of closed orbit distortion in either transverse direction is dipole kicks due to the direct misalignment of magnets in the x (horizontal) and y (vertical) directions.

The non-acceleration optical distortion study indicates that the severest impact of both dipole and quadrupole field errors will be on the amplitude of the β-functions.

2.3.2 Effects of resonance crossing

The scope of the previous non-acceleration studies is limited due to the dynamic nature of the changing betatron tune in a linear ns-FFAG. Koscielniak and Baartman [76, 77] undertook an analytical study on rapid crossing of betatron resonances, studying emittance growth at an isolated resonance. This paper gives, for an integer resonance, a tolerance for the n-th Fourier component B_n of the vertical magnetic field,

$$\frac{B_n}{B} = 2Q(\sqrt{Q_\tau})\frac{\Delta A}{C} \tag{2.24}$$

where B is the average magnetic field, Q is the machine tune, tune change per turn is Q_τ, the machine circumference is C, and ΔA is amplitude growth which reflects the

real emittance increase of the beam due to resonance crossing.

For the KST 3-ring lattice design considered here, the tolerable $b_n = \frac{B_n}{B\Delta A}$ given in [78] is $0.0266m^{-1}$ for protons and $0.0376m^{-1}$ for carbon ions (in comparison with $0.16m^{-1}$ for a muon ns-FFAG) . This indicates that magnet errors may cause significant distortion in a proton/ion ns-FFAG.

To ascertain the severity of the distortion caused by magnet alignment and field errors in a linear proton ns-FFAG, a detailed analysis of the effects of resonance crossing was undertaken including both acceleration and highly accurate tracking.

2.3.3 Acceleration studies

In a linear ns-FFAG accelerator the tune and other optical functions of the machine vary throughout the acceleration cycle. To predict the outcome of resonance crossing accurately the ray-tracing code ZGOUBI was chosen, as it incorporates both acceleration and tracking simultaneously. Three effects are considered; those of the stability of the betatron tune when quadrupole gradient errors are included, the effect of alignment errors on orbit distortion when crossing through resonances and the effect of such resonance crossing on the emittance of an accelerated beam.

Betatron tune stability

The dependence of the betatron tune on quadrupole gradient quality was found for 10 equally spaced momenta throughout the acceleration cycle. Taking one cell of the KST lattice, the F and D quadrupoles are given random patterns of 100 different quadrupole gradient qualities up to $\Delta K/K = 10^{-2}$, where K is the quadrupole gradient $\partial B_y/\partial x$. In order to quantify the effect of gradient quality on the stability of the cell tune (referred to as ν), the definition of the amplification factor in Eqn. 2.25 was used. The quantity $\Delta\nu^{\max}$ is the maximum variation of the cell tune from the perfect-quadrupole case out of the 10 momenta throughout the acceleration cycle.

This accounts for the possibility of the tune being more sensitive in a particular region of the acceleration cycle. Qualitatively, this indicates how field gradient errors affect the tune stability.

$$A = \frac{\Delta\nu^{\max}}{1\sigma(\Delta K/K)} \tag{2.25}$$

The result is A=0.23 in the horizontal direction, and A=0.20 in the vertical direction. This indicates that the operating point chosen is quite stable, and quadrupole gradient qualities do not have a large effect on the betatron tunes in this machine. For example, a reasonable gradient quality of 1×10^{-3} would only produce a 2.3×10^{-4} difference in the horizontal tune. Given that for a lattice with no errors the horizontal cell tune at the reference energy is around 0.17, this change corresponds to a shift in horizontal tune of only 0.13%, which is tolerable.

Orbit distortion with acceleration

In contrast to the closed orbit distortion studied in Section 2.3.1, this study with acceleration is to quantify the distortion of the orbit of a particle which begins on the closed orbit but whose trajectory deviates from the closed orbit due to errors, rather than the distortion of the closed orbit itself.

One hundred lattices were studied with patterns of alignment errors, this time with 10 different error sizes and 10 different lattices with each error size. The pattern of alignment errors is a Gaussian distribution cut-off at 3σ to remove very large errors which could have a dominant effect on the dynamics.

For this lattice design, each magnet within an FD doublet has the same magnitude and direction of alignment error, as it can be assumed they would be constructed on a single girder. One particle was tracked over 1000 turns to extraction, starting on the closed orbit at injection. This results in an acceleration rate of around 220 keV/turn. Accelerating cavities are represented as zero-length elements providing a simple en-

ergy gain, with a 'cavity' in every cell. This is done in order to neglect any resonance phenomena which may occur from the asymmetrical placement of RF cavities in the highly symmetric ring. Synchrotron motion is neglected as only the transverse dynamics are of interest here.

The orbit shape changes throughout acceleration and the orbit distortion is defined as the maximum deviation of the tracked particle from the closed orbit of the zero-error lattice, as shown in Fig. 2.13.

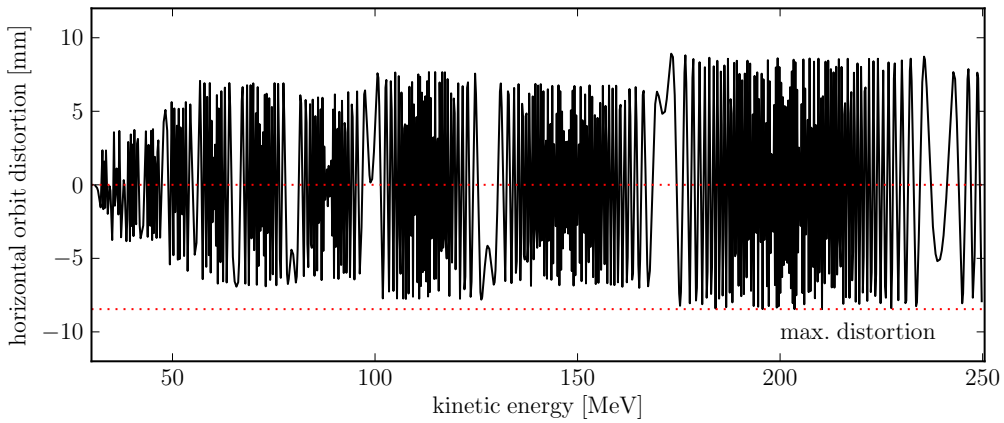

Figure 2.13: Example of distortion in a linear ns-FFAG, where the orbit distortion is calculated as the maximum distortion from the closed orbit of the zero-error lattice, as shown by the red lines.

The largest error size used in the study is determined as the σ error size at which particles are lost during tracking. The range of errors used is then 10 evenly spaced points between zero and the maximum error size. At each error size, the mean of the results for 10 lattices with random error patterns is plotted and the standard deviation of these results is given as error bars in Figs. 2.14 and 2.15.

The amplification factor is obtained by fitting a straight line to the mean values, shown as a red line. The error on the amplification factor is determined by the difference between the maximum/minimum fits and the central fit to the data.

The amplification factor (as in Eqn. 2.21) in the horizontal direction, with ac-

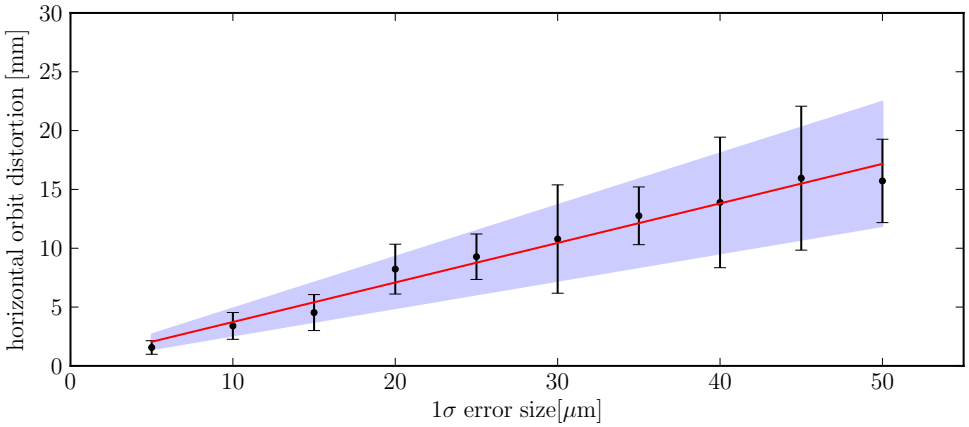

Figure 2.14: Fitted distribution of horizontal orbit distortion with horizontal alignment errors including acceleration.

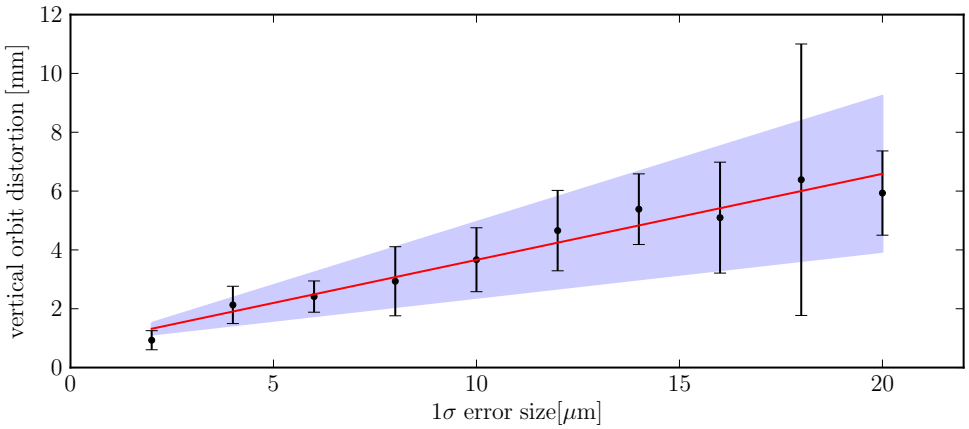

Figure 2.15: Fitted distribution of vertical orbit distortion with vertical alignment errors including acceleration.

celeration, is 336 ± 104; i.e. a realistic alignment error of $50\,\mu$m would induce an orbit distortion of approximately 16.8 mm. This is a factor of around 80 worse than the distortion of the closed orbit itself in the non-acceleration case. In the vertical direction the equivalent amplification factor is 293 ± 136. It should be noted that this presents an extremely stringent tolerance requirement on alignment errors in this type of lattice. In fact, for an acceptable distortion of 1 mm, the alignment would need to be better than $3\,\mu$m. This level of accuracy in alignment is not realistic.

Optical distortion with acceleration

The normalised emittance can be calculated from positions and momenta of a set of particles. Normalised emittance is constant throughout acceleration for an error-free lattice, however this is no longer true once alignment errors are incorporated.

To demonstrate the effect of the large orbit distortion observed in the previous section, 36 particles on a $10\,\pi$ mm mrad normalised emittance ellipse were tracked through the first 40 turns of acceleration, from 30.95 to 40 MeV. The initial ellipse parameters were determined from multi-particle tracking through a single cell around the closed orbit. Random horizontal alignment errors with a standard deviation of $50\,\mu$m are included, as in the previous section. The normalised emittance is re-calculated once per turn from the distribution of particle positions and angles in the centre of the long straight section. The resulting increase in normalised horizontal emittance is shown in Fig. 2.16.

The main regions in Fig. 2.16 where the emittance dramatically increases are those points where an integer horizontal total tune is crossed, as indicated by the vertical dashed lines. It is clear that a real beam would not survive the full acceleration cycle in this lattice design.

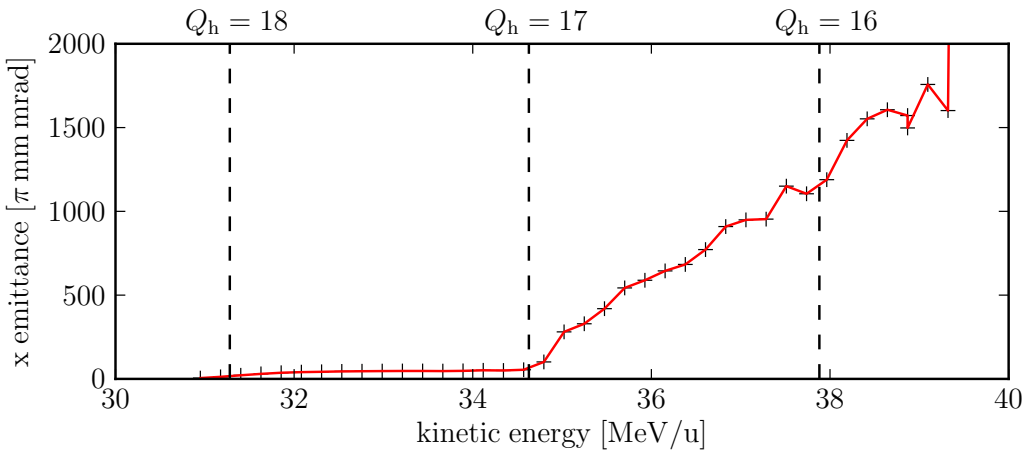

Figure 2.16: Change of normalised horizontal emittance in a linear non-scaling FFAG with 50 μm horizontal alignment errors.

2.4 Review of existing lattice designs

The lattice design presented here seems limited in its ability to meet the requirements laid out in Section 2.2.1. The lattice is very dense, with the longest drift length being just 0.29 m. While this makes the design relatively compact, it will have an impact in limiting the space available for RF systems, injection, extraction, corrector magnets and diagnostics. At the very least, this will be challenging to build.

However, the greatest problem presented here is the severity of alignment tolerances. The best alignment tolerances achieved in reality are around 50 μm. For the lattice design studied, where the amplification factor is found to be 336 in the horizontal direction and 293 in the vertical direction, this magnitude of error would result in an orbit distortion of greater than 10 mm, which is unacceptable. Taking into account additional sources of error including longitudinal and rotational alignment errors and a realistic magnetic field quality, in a real machine a more severe orbit distortion is expected than that observed here.

There are a number of ways to reduce the effect of resonance crossing on beam blow-up in ns-FFAGs. This design crosses around 12 integer machine tune resonances in both the horizontal and vertical plane. The variation of cell tunes throughout

acceleration as calculated with ZGOUBI is shown in Fig. 2.11.

The first possible solution would be to increase the acceleration rate, to cross the resonances more quickly. This may be feasible for a muon FFAG, but seems unrealistic for a medical accelerator in which any increase in acceleration rate would lead directly to greater capital costs for the machine. Increasing the acceleration rate would also require a larger integrated RF length which would be difficult in such a dense lattice with long straight sections of just 0.29 m.

Another option would be to change the number of cells. Assuming the beam dynamics remain acceptable, reducing the number of cells will reduce the number of machine integer resonances crossed, thereby reducing the amplification factor over the acceleration cycle. This was studied in a similar way to the KST lattice for a design based on a 24 cell lattice with wedge-shaped magnets [79, 80]. The total tune in the 24-cell lattice crosses four times fewer integer resonances in each transverse plane than the KST lattice and the amplification factor is reduced to 86.7. However, this would still require an alignment tolerance of 10 μm or better to limit the distortion to 1 mm. For this reason, it seems unlikely that changing the number of cells can reduce the problem to an acceptable level.

The third possible solution would be to add higher-order magnetic multipoles in the form of chromatic correction to reduce the total tune excursion to within one integer. This would remove the resonance crossing problem entirely. This method will be explored in more detail in Chapter 3.

Chapter 3

A novel non-linear ns-FFAG

Protons and carbon ions are many times more massive than the electons and muons for which the original ns-FFAG lattices were developed. The increased inertia of these particles imposes constraints on the design which restrict both the rate at which the particles can be bent in magnetic fields and the rate at which they can be accelerated. The original ns-FFAG designs cannot be simply scaled up to meet these requirements, as seen in Chapter 2. The only solution to this problem is the development of a new lattice design.

The lattice designs for PAMELA (Particle Accelerator for MEdicaL Applications) outlined in this chapter and in Chapter 4 reflect new developments in ns-FFAG accelerator design. Throughout the development process, strong emphasis is placed on the need for realistic magnet, RF and injection/extraction designs. The constraints imposed by these various components are included in the lattice optimisation alongside beam dynamics considerations.

To meet the particle energies defined by clinical requirements, two accelerating rings are needed. This is to limit the momentum range covered in each ring which in turn eases the RF frequency range and beam pipe apertures. The first ring accelerates protons to 250 MeV and C^{6+} ions to 68 MeV/u and the second will accelerate C^{6+}

to 400 MeV/u. The energies and rigidities of both particle species in these two rings are given in Table 3.1.

Particle	**H^+**		
Ring	1 inj	1 ref	1 extr
Kinetic Energy [MeV/u]	30.95	118.38	250
Bρ [Tm]	0.811	1.621	2.432

Particle	**C^{6+}**				
Ring	1 inj	1 ref	1 extr/2 inj	2 ref	2 extr
Kinetic Energy [MeV/u]	7.84	31.0	68.36	208.75	400
Bρ [Tm]	0.811	1.621	2.432	4.401	6.370

Table 3.1: Particle kinetic energies and magnetic rigidities for 2 ring complex, where 'inj' is the injection energy to the ring, 'ref' is the reference energy and 'extr' is the highest extraction energy for each ring.

In each lattice, the variation of the total betatron tune in both transverse planes is constrained to within half an integer throughout acceleration. This avoids the problems associated with linear ns-FFAG lattices discussed in Chapter 2. Simultaneously, the lattice solution maintains advantageous non-scaling properties such as a small orbit excursion and relatively simple magnets which are easy to align. The lattice design strategy is outlined here, together with the optimisation and resulting performance of the smaller 'proton ring'.

3.1 Design Strategy

The first aim of the design strategy is to overcome the deterioration of the beam due to resonance crossing as discussed in Chapter 2. To achieve this, there have been a number of strategies proposed. The first is from Johnstone *et al.* who propose a linear ns-FFAG with wedge-shaped quadrupoles [81]. Both the path length through the quadrupole and the edge focusing [45, p.42] are designed as a function of the beam momentum. This makes the effective optics of the lattice independent of momentum. It is then possible for the tune to be kept within an integer over a wide momentum

range, avoiding the crossing of major resonances. However, over the momentum range proposed, the orbit shift in these designs is still relatively large, of the order of 1 m.

Another strategy to avoid resonance crossing was proposed by S. Machida [82]. In this case a more conventional method of chromaticity correction is applied to a linear ns-FFAG. This involves adding a sextupole and octupole component to the linear ns-FFAG to correct the natural chromaticity, where the strength of these components is determined by the downhill simplex method [83]. Unfortunately chromaticity correction of this type results in a machine which has complex multipole magnets and a similar orbit shift to a scaling FFAG. The reason for this is two-fold. First, chromaticity correction is usually applied where the dispersion function is largest as it is most effective at this point. However, the dispersion function in linear ns-FFAGs tends to be small as this gives the desirable property of a smaller orbit shift. This means that the non-linear magnet strengths to obtain chromaticity correction must be large in such a machine. Second, the upper limit on cell tune variation is inversely proportional to the number of cells. The requirement that the total tune variation is restricted to within an integer (or preferably half an integer) indicates that a small number of cells is preferable, whereas a linear ns-FFAG tends to have a large number of cells. This makes chromaticity correction even more challenging.

Instead of trying to introduce zero chromaticity in a linear ns-FFAG, the PAMELA design maintains the properties of a scaling FFAG as much as possible while relaxing the strictly scaling magnetic field and simplifying the magnet shape and alignment. This allows a fixed tune over the momentum range, while having the flexibility to minimise the orbit shift and simplify the machine construction.

The concept of this novel type of ns-FFAG is based on an idea first suggested by S. Machida at the FFAG'08 workshop in Manchester, UK [84] which was then developed by this author for the PAMELA design [85, 86]. The design concept begins by considering a radial-sector scaling FFAG with a FDF (focusing-defocusing-focusing)

triplet structure. A scaling FFAG of this variety employs a magnetic guide field which follows the r^k law, introduced in Chapter 2, which results in geometrically similar orbit sizes and constant tunes throughout acceleration. It is normal in this type of FFAG for the orbit shift to be of the order of 1 m, which is undesirably large. The orbit shift scales with the field index k as in Eqn. 3.1.

$$\frac{\Delta r}{r_0} \approxeq \frac{1}{k+1}\frac{\Delta p}{p_0}, \tag{3.1}$$

where Δr is the orbit shift, Δp is the momentum increase from injection to extraction and p_0 and r_0 correspond to the the reference momentum and reference radius. Unfortunately, attempting to increase the field index k to reduce the orbit shift will increase the phase advance until the optics become unstable as;

$$\frac{dB_y}{dr} = \frac{B_y}{r}k. \tag{3.2}$$

However, this is only the case if considering the first stability region of Hill's equation. By further increasing the focusing strength in the FDF triplet focusing structure, it is possible to have a second stability region next to the first. This is discussed further in Section 3.1.1. From this starting point, the design strategy adopted here makes the design non-scaling, breaking away from the scaling FFAG principle at each stage of the design process, while ensuring that the total machine tune variation is within half an integer to avoid the resonance crossing described in Chapter 2.

The design of this FFAG lattice has major differences from the scaling concept and should be referred to as a non-linear ns-FFAG. The main differences are as follows:

1. The scaling law is approximated as a Taylor series (and later a polynomial fit) and truncated at the octupole or decapole. This breaks the scaling law and makes the machine non-scaling. This also significantly changes the magnet

design, removing the need for iron-cored magnets with the complicated pole shaping used in a scaling FFAG.

2. The magnets, rather than being sector-shaped as in a scaling FFAG, are made rectangular, in order to reduce costs in manufacturing.

3. The magnets in each triplet cell are aligned along a straight line, rather than along the arc of a circle described at the machine radius. This should ease alignment and the production of other systems, such as cryogenics, which will need to be integrated.

4. The second stable region of Hill's equation is used, with a horizontal phase advance per cell greater than 180°. This allows for a larger field index to be used, resulting in factor of five reduction in orbit excursion.

5. Depending on the ratio of cell length to machine circumference, the straight sections between cells can be increased to provide a long straight section of over 1 m, while preserving stable dynamics. The idealised layout of the lattice design is shown in Fig. 3.1.

3.1.1 Solution of Hill's equation for a second stable region

The numerical solution of Hill's equation for an FDF triplet focusing structure is central to the lattice design strategy. The solution of the linear second order differential Hill's equation is well known and its application to accelerators is found in many sources, the most relevant to this work being Ref. [44] and Ref. [56, p. 85-87]. The full solution is given here and stable regions are found numerically using Mathematica™ [87]. The solution for basic FD alternating gradient focusing is discussed first, followed by the solution for FDF triplet focusing.

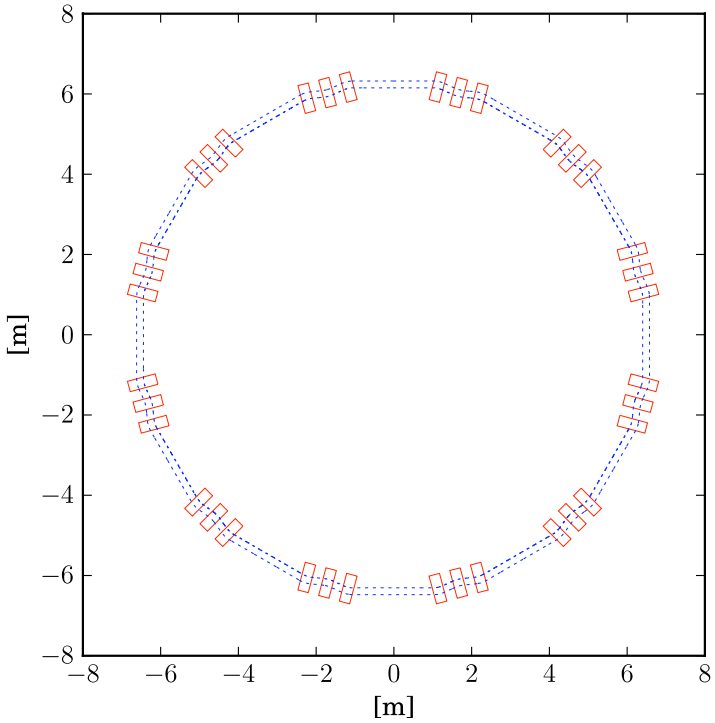

Figure 3.1: Layout of the proton lattice with injection orbit (inner dotted line) and maximum energy orbit (outer dotted line).

The equations for horizontal and vertical motion are given in Eqn. 3.3 and the function $f(\theta)$ can be used to describe basic FD alternating gradient focusing, as in Eqn. 3.4, where θ is the azimuthal position in one cell of total angle θ_0, $\pm f_0$ is the average focusing strength in the horizontal/vertical plane respectively and f_1 is the strength of alternating gradient focusing. The focusing term in Hill's equation is normalised so that the solution is independent of machine radius and is given by $K = \left[\frac{2\pi}{l}\right]^2 f(\theta)$, where l is the total length of the cell.

$$\begin{aligned} x'' + Kx &= 0 \\ y'' - Ky &= 0 \end{aligned} \tag{3.3}$$

$$f(\theta) = \begin{cases} f_0 + f_1 = const., & 0 < \theta < \frac{1}{2}\theta_0 \\ f_0 - f_1 = const., & \frac{1}{2}\theta_0 < \theta < \theta_0. \end{cases} \tag{3.4}$$

The solution to the linear second order differential Hill's equation in the matrix formulation takes the form of Eqn. 3.5 in which $x'(s)$ is the derivative of $x(s)$ and the same form of solution holds in the vertical $y(s)$ plane.

$$\mathbf{X}(s) = \begin{bmatrix} x(s) \\ x'(s) \end{bmatrix} = \mathbf{M}(s|s_0)\mathbf{X}(s_0) = \begin{bmatrix} a & b \\ c & d \end{bmatrix} \begin{bmatrix} x(s_0) \\ x'(s_0) \end{bmatrix} \tag{3.5}$$

The focusing function $f(\theta)$ is piecewise constant and the matrix $\mathbf{M}(s|s_0)$ is simply the product of the matrices for the sub-intervals in which $f(\theta)$ is constant. The matrices for each sub-interval for constant focusing take a different form depending on whether $f(\theta)$ is greater, less than or equal to 0, as in Eqns. 3.6 to 3.8.
For $f(\theta) > 0$ where $\phi = \sqrt{K}(s - s_0)$:

$$\mathbf{M}(s|s_0) = \begin{bmatrix} \cos\phi & \frac{1}{\sqrt{K}}\sin\phi \\ -\sqrt{K}\sin\phi & \cos\phi \end{bmatrix}. \tag{3.6}$$

For $f(\theta) < 0$ where $\psi = \sqrt{-K}(s - s_0)$:

$$\mathbf{M}(s|s_0) = \begin{bmatrix} \cosh\psi & \frac{1}{\sqrt{-K}}\sinh\psi \\ \sqrt{-K}\sinh\psi & \cosh\psi \end{bmatrix}. \tag{3.7}$$

For a region of no focusing $K = 0$ over a length l_d where $l_d = s - s_0$:

$$\mathbf{M}(s|s_0) = \begin{bmatrix} 1 & l_d \\ 0 & 1 \end{bmatrix}. \tag{3.8}$$

In the case of FD alternating gradient focusing the total matrix $\mathbf{M} = \mathbf{M_D}.\mathbf{M_F}$. The resulting oscillatory motion is stable when the absolute value of the trace of the matrix $|\mathbf{Tr}[\mathbf{M}]| \leq 2$ and unstable otherwise.

The stable regions for basic FD alternating gradient focusing in the horizontal and vertical planes are found using Mathematica$^{\text{TM}}$and are shown in Fig. 3.2.

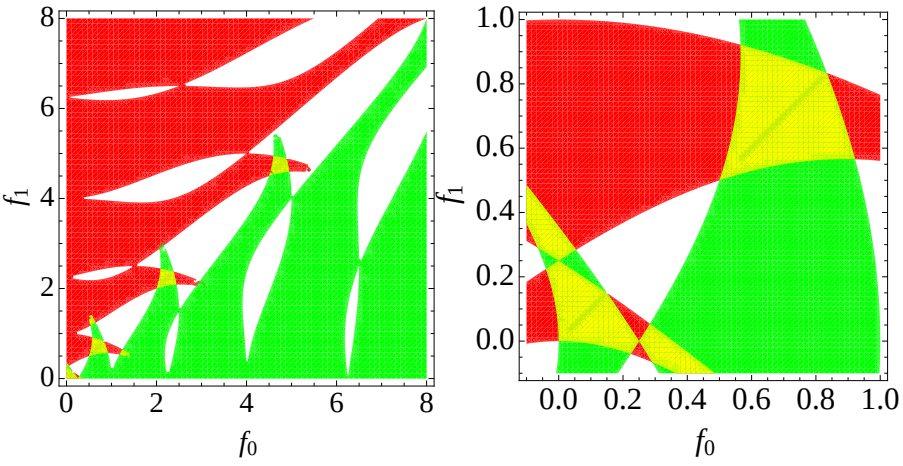

Figure 3.2: (a) The resulting stability regions in a basic alternating gradient (FD) focusing cell in the horizontal (green) and vertical (red) planes as a result of changing the average focusing f_0 and strength of alternating gradient focusing f_1. Overlap regions are shown in yellow. (b) A close-up view of the first and second stability regions in a basic (FD) focusing cell.

This shows that as the average focusing strength is increased multiple stable re-

gions appear, in this case the first 6 stable regions in each plane are shown. Naturally, stability in one plane does not mean the same region is stable in the other plane. The regions where both planes are stable are shown in yellow. In this example there are no drift spaces between the magnets, which is an unrealistic scenario. Including drift spaces will move the stability regions apart, so that for reasonable values of the focusing ($f_0, f_1 < 2$) only the first stable region is available using FD focusing.

The triplet lattice in an FDF configuration such as the one considered here has a different function of $f(\theta)$, given in Eqn. 3.9, where α is the magnet packing factor - the total length of the FDF triplets compared to the machine circumference.

$$f(\theta) = \begin{cases} f_0 + f_1 = const., & 0 < \theta < \dfrac{\alpha\theta_0}{3} \\ f_0 - f_1 = const., & \dfrac{\alpha\theta_0}{3} < \theta < 2\dfrac{\alpha\theta_0}{3} \\ f_0 + f_1 = const., & 2\dfrac{\alpha\theta_0}{3} < \theta < \alpha\theta_0 \\ 0, & \alpha\theta_0 < \theta < \theta_0 \end{cases} \tag{3.9}$$

The stable regions are again found using Mathematica$^{\text{TM}}$and are shown in Fig. 3.3.

In the top half of each stability diagram where $0 < f_1 < 2$, two small yellow stable regions are visible which come progressively closer to each other between Fig. 3.3a and Fig. 3.3b as the packing factor α is reduced from 0.8 to 0.5. This is mirrored in the bottom half of the stability diagrams for $-2 < f_1 < 0$. The advantage of having the two stable regions close to each other is that the lattice functions (tunes, β-functions etc...) should be similar in the two regions.

The FDF triplet focusing lattice was selected due to the availability of the second stable region close to the first with a reasonable packing factor and $f_0, f_1 < 2$.

3.1.2 Selection of baseline lattice parameters

In order to access the second stable region of Hill's equation for an FDF triplet focusing lattice while maintaining suitable dynamics, it is preferable to have a small ($\alpha \approx 0.5$) packing factor, as discussed above. However, too small a value for α results in short magnet lengths with very long straight sections. This may result in unachievable magnetic fields or, to compensate, a very large radius of the accelerator. For these reasons α is chosen to be suitably large to achieve a compact accelerator while preserving the stable dynamics.

Once the packing factor and average radius are chosen, the peak magnetic field can be reduced slightly by extending the magnets into the short drift space, ensuring the magnetic centre remains fixed. The baseline lattice design parameters for the 'proton ring' for PAMELA are outlined in Table 3.2. This baseline is taken as a starting point for comparison of the effects of the design strategy on lattice dynamics and for lattice optimisation.

Parameter	**Inj.**	**Ref.**	**Extr.**
Proton Kinetic Energy [MeV]	30.95	118.38	250
C^{6+} Kinetic Energy [MeV/u]	7.84	30.98	68.36
Bρ [Tm]	0.811	1.621	2.432
Cells		12	
r_0 [m]		6.251	
Magnet length [m]		0.3144	
Packing factor α		0.48	
Field index, k		38	
Orbit excursion [m]		0.176	

Table 3.2: Lattice parameters for the PAMELA proton ring.

Throughout the following studies an Enge type fringe field with an extent of 60 mm is assumed, as described in Chapter 2. The available working points as a function of field index and D/F magnet strength ratio for the baseline lattice as calculated with SCode [88] are shown in Fig. 3.4. By carefully choosing the field index to be as large as practicable, in this case $k = 38$, a D/F ratio is then chosen which results in cell

tunes of around $\nu_x = 0.75$, $\nu_y = 0.25$. The cell tunes are later refined to ensure the total tune variation is away from any integer resonances.

3.2 Effects of design strategy on lattice dynamics

Each of the major changes from a scaling FFAG described earlier in Section 3.1 affects the lattice dynamics in a different way. For the purpose of studying these independently, each change is applied separately to the baseline lattice. Further consideration is given to the variation of fringe field extent with radius and the difference between using a Taylor expansion or polynomial fit to the scaling FFAG field profile. The end result is the optimised design for the proton and low energy carbon lattice.

3.2.1 Multipole expansion

Starting from the baseline scaling FFAG design, the first step of the design strategy is the multipole expansion of the vertical magnetic field. The field increase in the radial direction, as defined in Chapter 2 is given by $B = B_0(r/r_0)^k$, where r is the radial co-ordinate, k is the field index defined as $k = (r/B_y)(dB_y/dr)$ and y is the vertical direction. This field profile is shown in Fig. 3.5.

When the scaling law is expanded as a Taylor series and truncated at the decapole (n=4) component, the resulting field profile is given by Eqn. 3.10.

$$B_y = B_0\Big[1 + \frac{k(r-r_0)}{1!\,r_0} + \frac{(k-1)k(r-r_0)^2}{2!\,r_0^2} + \frac{(k-2)(k-1)k(r-r_0)^3}{3!\,r_0^3} + \frac{(k-3)(k-2)(k-1)k(r-r_0)^4}{4!\,r_0^4}\Big] \tag{3.10}$$

Due to the nature of a Taylor expansion, the difference in field between the exact scaling law and this expansion increases with distance from the reference radius, r_0. The particles follow trajectories with a different mean radius in each magnet, as they

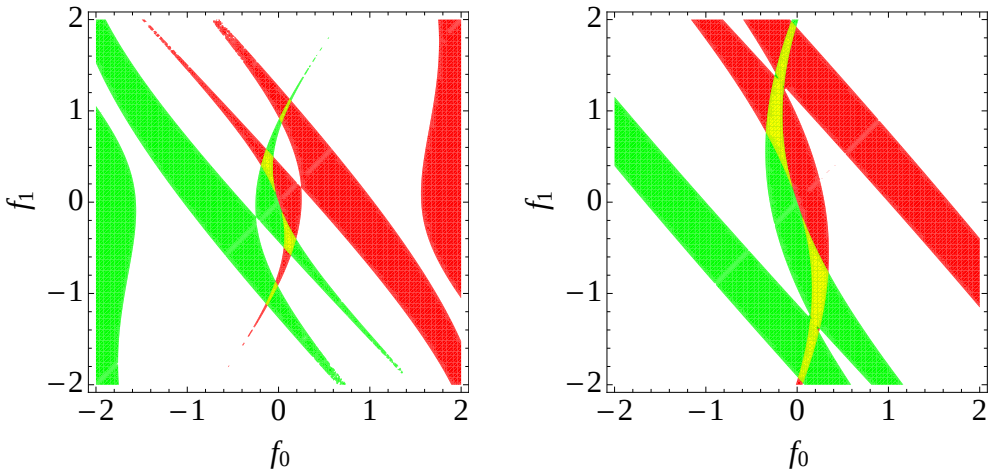

Figure 3.3: The resulting stability regions after the numerical integration of Hill's equation for (a) an FDF triplet with magnet packing factor $\alpha = 0.8$ and (b) an FDF triplet with $\alpha = 0.5$. The horizontal stable region is shown in red and the vertical stable region in green. The yellow overlapping area has stability in both horizontal and vertical planes.

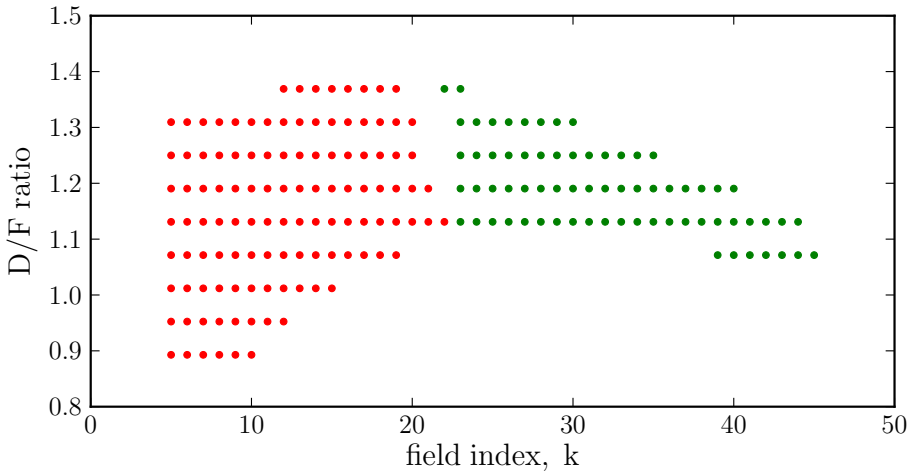

Figure 3.4: Available working points for the proton lattice at reference energy (118 MeV protons). The second stable region with $\nu_x > 0.5$ is shown in green.

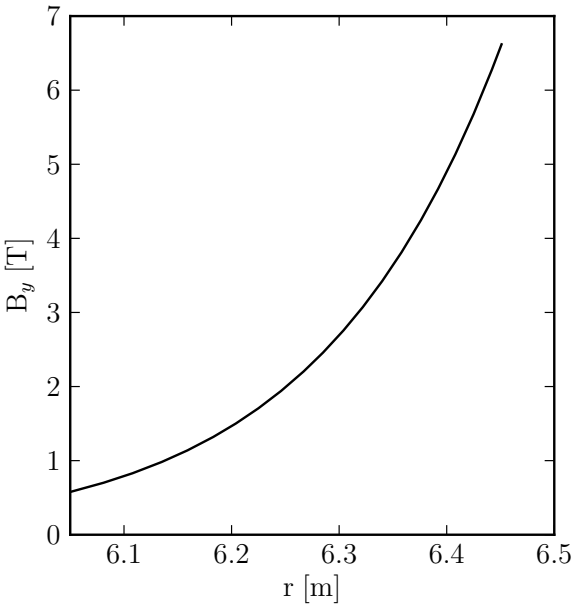

Figure 3.5: Ideal magnetic field profile of a scaling FFAG for a lattice with $k = 38$, $r_0 = 6.251$ m, $B_0 = 2.0$ T. B_y is the vertical magnetic field component.

experience reverse bending in the D magnet, shown in Fig. 3.6. For this reason, a different r_0 value is used in the F and D magnets. The offset is determined to be the central point of the orbit shift at the centre of each magnet in an ideal scaling version of the FFAG.

If this offset is not implemented, there is a large deviation in tune at low momentum, caused by the difference between the Taylor expansion and the ideal scaling law in this region, as shown in Fig. 3.7.

In this case the magnets are wedge shaped and aligned such that three triplet magnets face the machine centre as in a scaling FFAG. Single particles tracked through one cell on the closed orbit at the injection and highest extraction momentum are shown in Fig 3.6.

In order to determine the multipole order required to achieve a total tune excursion of less than half an integer, the betatron tunes throughout acceleration are obtained by multi-particle tracking for different orders of included multipoles. Multipole orders up

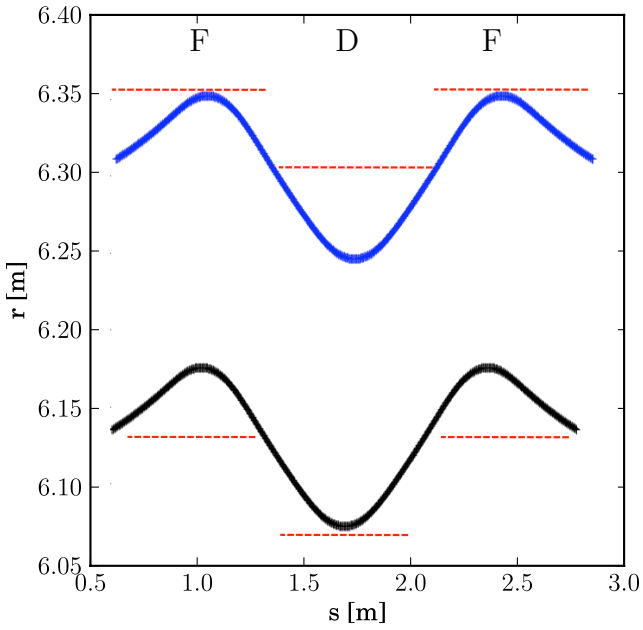

Figure 3.6: Single particles tracked through one cell on the closed orbit at the injection (black) and highest extraction momentum (blue) with red outlines of illustrative magnet positions where the magnet centres are shifted to the mid-point of the particle traces.

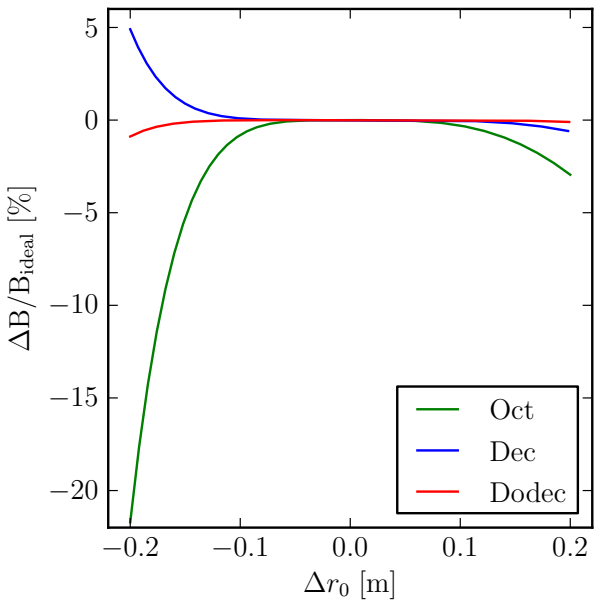

Figure 3.7: Percentage difference in vertical field between Taylor expansion to varying order and the ideal field profile, as a function of radius. In this case $r_0 = 6.251$.

to $n = 3$, 4, 5 (octupole, decapole and dodecapole, respectively) are studied and the resulting tunes shown in Fig. 3.8. The maximum variation of the cell and total tunes with varying orders of multipole are in Table 3.3. For the decapole and dodecapole cases the total tunes in both planes are well within half an integer.

Multipole order	ν_x	ν_y	Q_x	Q_y
Octupole	0.0467	0.0246	0.5600	0.2946
Decapole	0.0047	0.0025	0.0562	0.0298
Dodecapole	0.0006	0.0002	0.0067	0.0027

Table 3.3: Variation of cell ($\nu_{x,y}$) and total ($Q_{x,y}$) tunes as a result of changing the order of multipole expansion.

3.2.2 Variation of fringe field extent

In a scaling FFAG, the variation of the fringe field extent with radius can play a part in minimising the tune excursion as in Ref. [89]. The fringe fields in ZGOUBI are described using the Enge model as described in Chapter 2. The half-gap height of the magnet g can be made dependent on radius, as in Eqn. 3.11, where g_0 is the half-gap height at the reference radius r_0. This allows for variation of the fringe field extent with radius according to the variable κ. In the case of $\kappa \neq 0$, g_0 is replaced by g in Eqn. 2.17.

$$g(r) = g_0(r_0/r)^\kappa \tag{3.11}$$

The effect of this variation was examined for the case of the multipole expansion up to and including the decapole component. The first case has a fringe field extent proportional to the orbit radius so the extent increases with radius ($\kappa = -1$), and the second has the opposite property, where the fringe field extent decreases with radius ($\kappa = +1$). These are compared to a case with constant fringe field extent with radius ($\kappa = 0$). For both cases $g_0 = 60\,\text{mm}$ and the coefficients $C_0 = 0.1455, C_1 =$

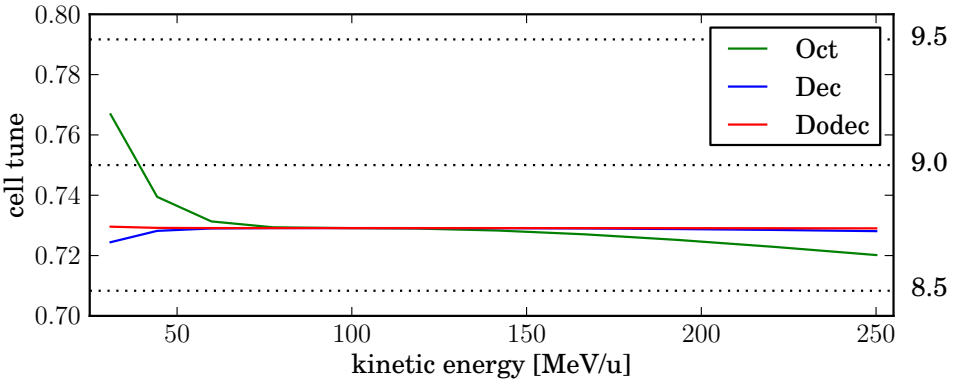

(a)

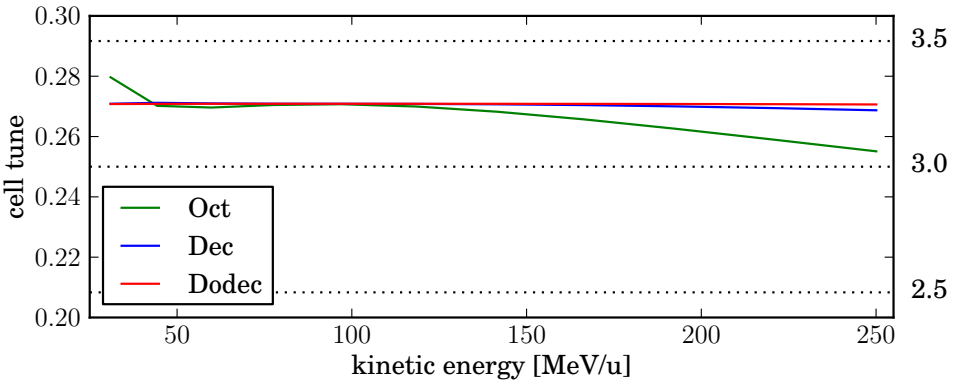

(b)

Figure 3.8: Cell tunes throughout acceleration for the case of wedge shaped magnets with different order of truncation. Horizontal cell tune in (a) and vertical cell tune in (b). Dashed lines and associated numbers show total tune of a 12 cell ring.

$2.2670, C_2 = -0.6395, C_3 = 1.1558, C_4 = C_5 = 0$ are used as before. The difference in tune excursion between the two cases is small, as shown in Fig. 3.9. For this reason a constant fringe field extent with radius is adopted.

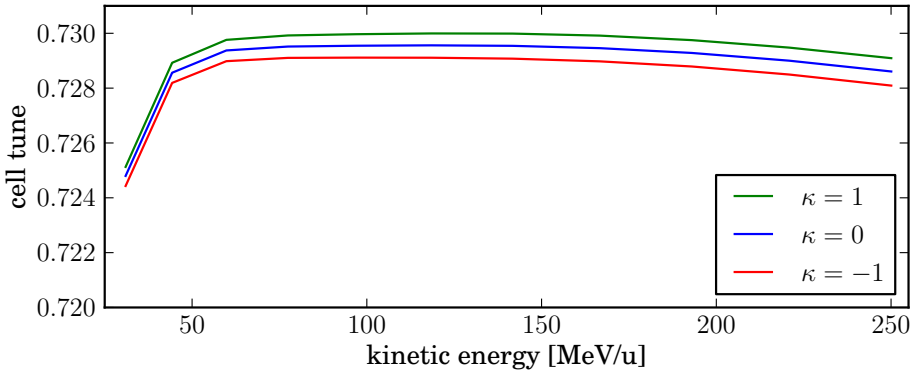

(a)

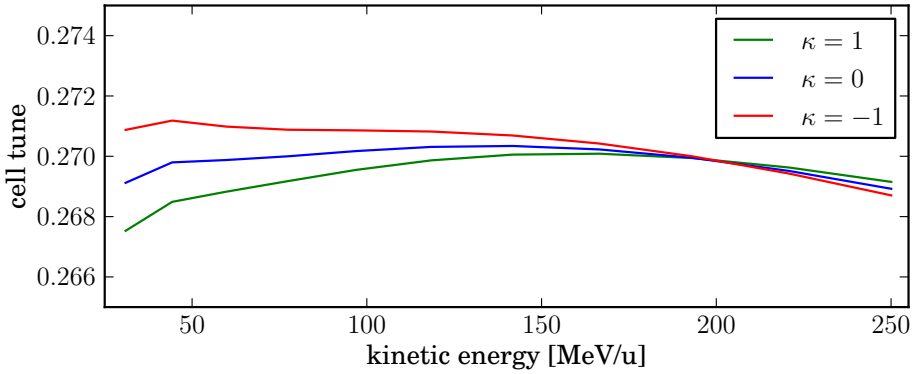

(b)

Figure 3.9: Cell tunes throughout acceleration for different models of the fringe field extent. Horizontal cell tune in (a) and vertical cell tune in (b). Note that the scale of tune variation is ten times smaller than in Fig. 3.8.

3.2.3 Rectangular magnets

The lattice magnets become simpler to construct and align when they are rectangular rather than wedge or sector shaped. For the purpose of studying the specific effect that using rectangular magnets has on lattice dynamics, the orientation of the magnets

remains the same at this stage so that the three rectangular magnets face the machine centre.

An idealized rectangular magnet can be defined with field lines parallel to the magnet axis. The field profile is represented in a Cartesian coordinate system as

$$B_y = B_{y,0}\left(\frac{x_0+x}{x_0}\right)^k = B_{y,0}\left(1+\sum_{n=1}\frac{1}{n!}\frac{k(k-1)\cdots(k-n+1)}{x_0^n}x^n\right) \tag{3.12}$$

where x_0 at the F magnet and D magnet are the same as r_0 defined in the previous section, x is the horizontal coordinate and k is the field index as before. Multipoles up to $n = 3$, 4, 5 (octupole, decapole and dodecapole, respectively) are included. A line perpendicular to each F magnet axis intersects that of the D magnet at the machine centre, as shown in Fig. 3.10. The Enge type fringe field with a constant extent of 60 mm is assumed, as before. As the magnets are rectangular, it is reasonable to assume that the fringe field extent is constant and independent of radial position.

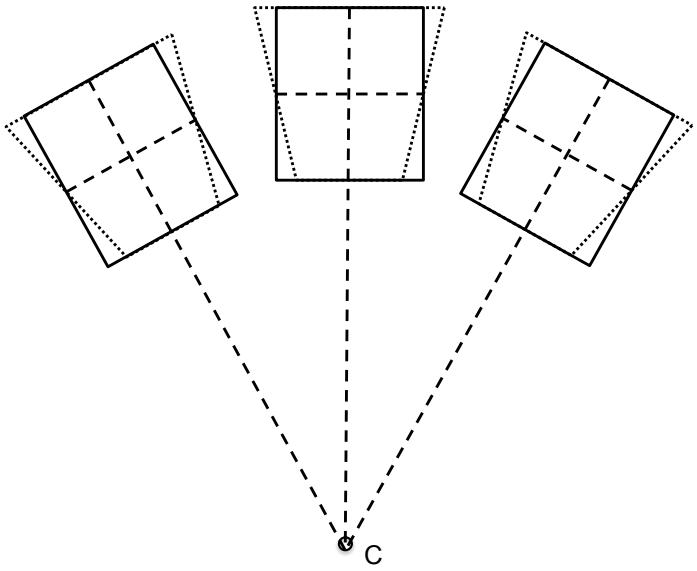

Figure 3.10: Converting wedge shaped magnets (dotted) to rectangular magnets (solid line). The magnet centre is unchanged and the three magnets face the machine centre.

The resulting betatron tunes throughout acceleration are shown in Fig. 3.11. The maximum variation of the cell and total tunes with varying orders of multipole for

the case of rectangular magnets on an arc are in Table 3.4. The maximum variation of the total horizontal tune with multipoles up to decapole is 0.042 and of the total vertical tune is 0.299, both of which are well within half an integer of total tune.

Multipole order	ν_x	ν_y	Q_x	Q_y
Octupole	0.0512	0.0454	0.6149	0.5445
Decapole	0.0035	0.024	0.0423	0.2995
Dodecapole	0.0042	0.0231	0.0506	0.2771

Table 3.4: Variation of cell ($\nu_{x,y}$) and total ($Q_{x,y}$) tunes as a result of changing the order of multipole expansion for rectangular shaped magnets on an arc.

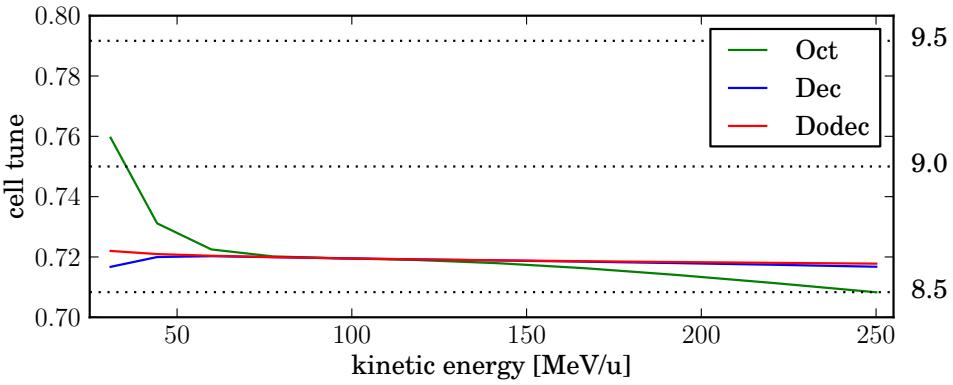

(a)

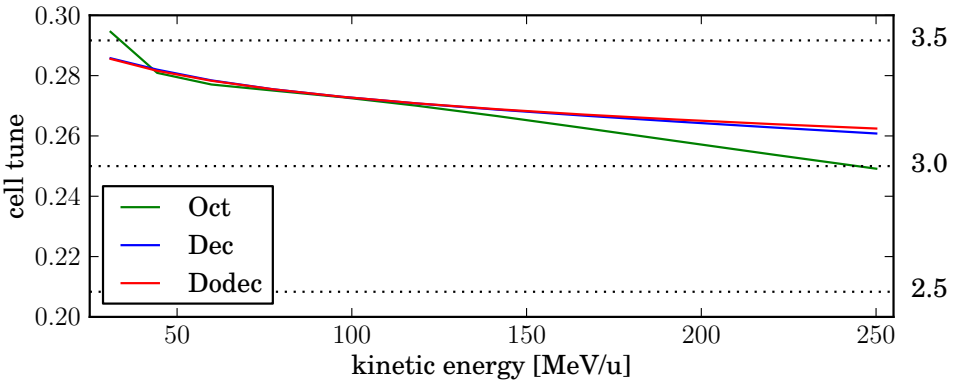

(b)

Figure 3.11: Cell tunes throughout acceleration for the case of rectangular shaped magnets with different order of truncation. Three magnets face the machine centre as in Fig. 3.10. The horizontal cell tune is shown in (a) and the vertical cell tune in (b). Dashed lines and associated numbers show total tune of a 12 cell ring.

3.2.4 Alignment of magnets

To simplify alignment issues further, the three multipole magnets are aligned parallel with each other. As shown in Fig. 3.12, both F magnets are rotated with respect to the magnet centre so that the three magnets become parallel. This will lead, in a realistic scenario, to a transverse offset between the magnets in the triplet in order to optimise the magnetic bore size. The field profile of each magnet is the same as in the previous section, namely the multipoles up to a certain order are included and the fringe field has a constant extent of 60 mm.

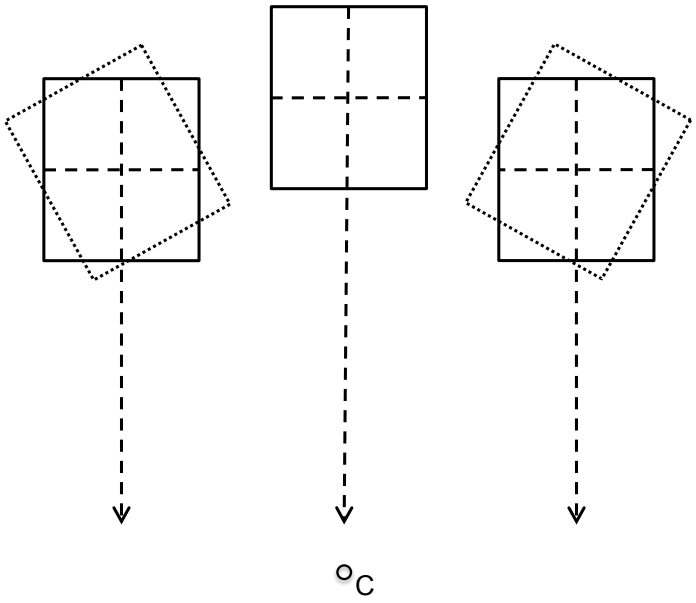

Figure 3.12: Converting rectangular magnets facing the machine centre (dotted) to rectangular magnets aligned parallel with each other (solid).

The resulting tunes throughout acceleration are shown in Fig. 3.13 and the variation of tunes is given in Table 3.5. In the case up to decapole, the maximum variation of the total horizontal tune is 0.093 and of the total vertical tune is 0.250. These values are very similar to the case before and well within half an integer.

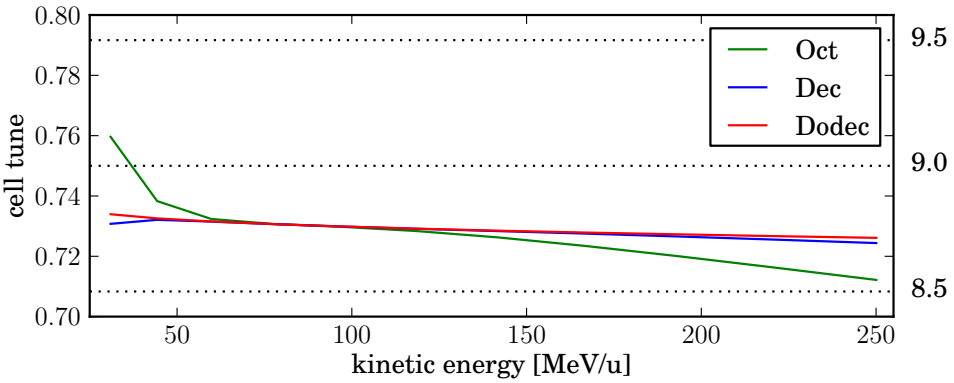

(a)

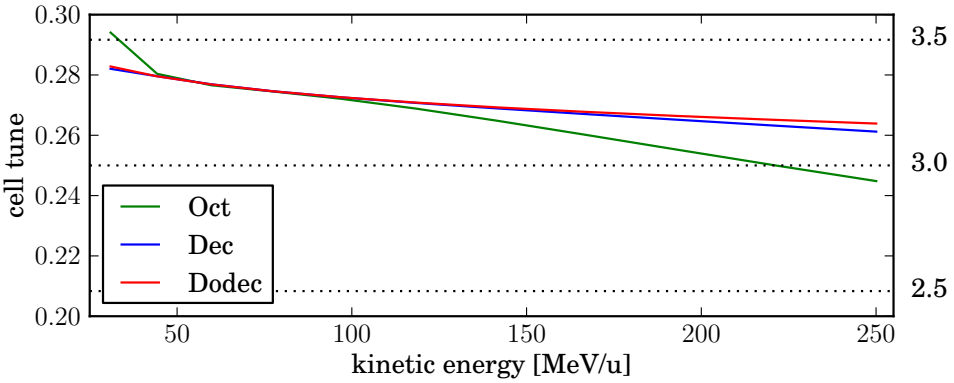

(b)

Figure 3.13: Cell tunes throughout acceleration for the case of rectangular shaped magnets with different order of truncation. Three magnets are aligned parallel with each other. Horizontal cell tune in (a) and vertical cell tune in (b). Dashed lines and associated numbers show total tune of a 12 cell ring.

Multipole order	ν_x	ν_y	Q_x	Q_y
Octupole	0.0474	0.0492	0.5693	0.5909
Decapole	0.0077	0.0208	0.0925	0.2499
Dodecapole	0.0078	0.0189	0.0939	0.2271

Table 3.5: Variation of cell ($\nu_{x,y}$) and total ($Q_{x,y}$) tunes as a result of changing the order of multipole expansion for rectangular shaped magnets aligned parallel to each other.

3.2.5 Taylor expansion vs. polynomial fit

So far the multipole components used have been determined by using a Taylor expansion of the scaling field around the central orbit position for each magnet. However, for an orbit shift of greater than $\approx 100\,\text{mm}$, a closer fit to the field profile of r^k can be obtained using a polynomial fit in the region of interest, that is the region of magnetic field experienced by the particle beam. The polynomial fit is calculated using the well-known method of least squares.

The main reason for trying to match the multipole expansion to that of the ideal field profile is to achieve flat tunes throughout acceleration. Since the betatron tunes are determined by the local gradient of the field rather than the field value itself, an improvement in the overall tune excursion throughout acceleration may be achieved by ensuring that the gradient of the field is as close as possible to the gradient of the ideal profile. The variation from the ideal gradient profile after using a Taylor expansion to decapole is shown in Fig. 3.14, where B' is the field gradient with respect to radius. In the region that the beam experiences, shown by the dotted lines, the gradient of the field differs from the exact scaling profile by around 1% at the low momentum end, where the maximum tune excursion is observed in Fig. 3.8. Any further excursion of the beam in this direction would result in a gradient which rapidly diverges from the ideal gradient profile.

For comparison, the variation of the field strength (rather than the gradient) using a Taylor expansion does not show such a large difference from the ideal field profile,

as seen in the decapole curve in Fig. 3.7. This shows that in order to minimise the variation of tunes, the field gradient must be as close as possible to the ideal gradient.

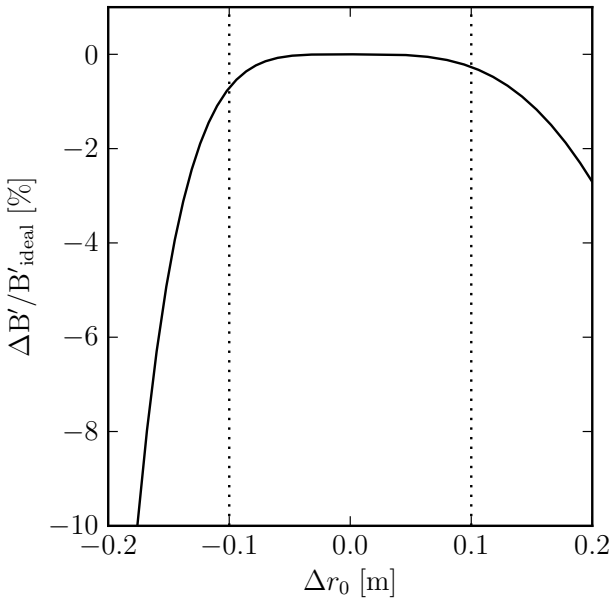

Figure 3.14: Difference in field gradient between Taylor expanded scaling field and exact scaling field. In this case the Taylor expansion is up to and including the decapole component.

Therefore, in order to achieve flatter tunes throughout acceleration, polynomial fits to either the field strength or field gradient determined by the scaling law are considered. The resulting tune excursion for polynomial fits to the field strength and field gradient using up to the decapole component, and the tune excursion for a polynomial fit to the field gradient using only up to the octupole component, are given in Table 3.6 and shown in Fig. 3.15.

Multipole order	ν_x	ν_y	Q_x	Q_y
Deca, Strength	0.0041	0.0045	0.0489	0.0537
Octu, Grad	0.0130	0.0152	0.1560	0.1824
Deca, Grad	0.0040	0.0044	0.0476	0.0528

Table 3.6: Variation of cell ($\nu_{x,y}$) and total ($Q_{x,y}$) tunes as a result of changing the order of polynomial fit for rectangular shaped magnets aligned parallel to each other.

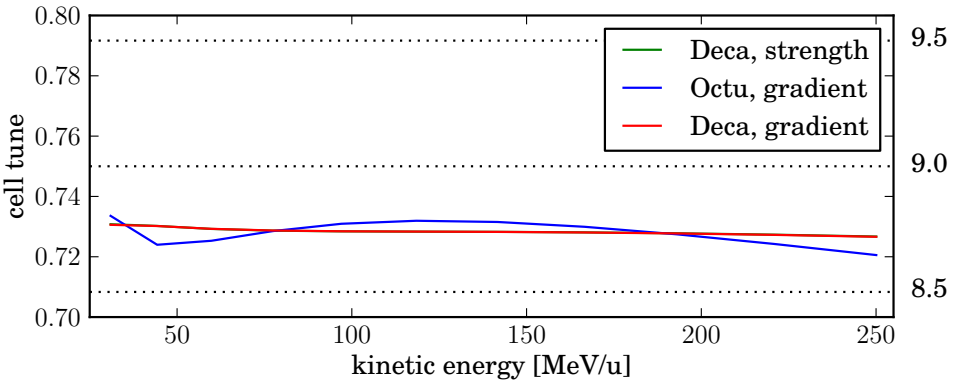

(a)

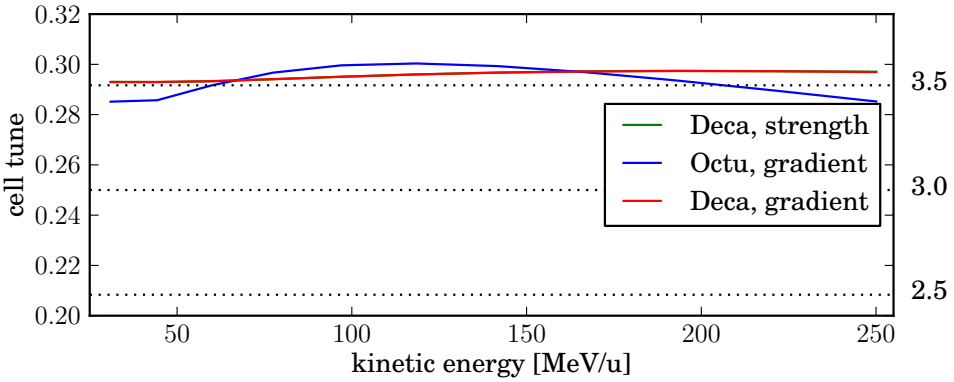

(b)

Figure 3.15: Cell tunes throughout acceleration for the case of rectangular shaped magnets with polynomial fit to either strength or gradient of scaling field. Three magnets are aligned parallel with each other. Horizontal cell tune in (a) and vertical cell tune in (b). Dashed lines and associated numbers show total tune of a 12 cell ring. In both (a) and (b) the difference between the two decapole cases is too small to be visible at this scale.

These results indicate that by simply using a polynomial fit to either the field profile or the gradient instead of using a Taylor expansion results in a greatly improved fit to the local field gradient, and hence a much reduced total tune excursion.

In fact, the variation of the total tune throughout acceleration using a polynomial fit up to the octupole component is reduced to just 0.156 and 0.182 for the horizontal and vertical tunes respectively. These are both well within half an integer, indicating that it is possible to achieve the required total tune constraint without the need for a decapole field if a polynomial fit to the field profile is used. This allows for further simplification of the required magnets, helping to reduce the machine cost.

3.3 Proton lattice performance

The lattice which emerges from the four steps of the design procedure using a polynomial fit to the field is considered to be the optimised lattice design. The parameters of the resulting proton lattice are in Table 3.7. This is the design adopted for further studies of the lattice performance.

Parameter	**Value**
Cells	12
r_0 F [m]	6.2600
r_0 D [m]	6.1869
Magnet length [m]	0.3144
Packing factor α	0.48
Field index, k	36.721
Orbit excursion [m]	0.1760
Target cell tunes (horiz / vert)	0.7292 / 0.2768

Table 3.7: Optimised lattice parameters for the proton ring of PAMELA.

Optics and Orbit

The beta functions in one cell of the proton ring as calculated with SCode are shown in Fig. 3.16. To calculate the orbit shift with acceleration a single particle was tracked

from injection to extraction on the closed orbit. The resulting change in horizontal position at the centre of the long straight section is shown in Fig. 3.17. The total orbit excursion throughout acceleration is 17.6 cm.

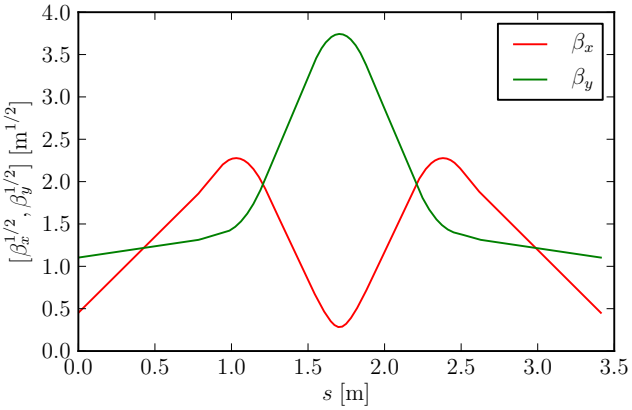

Figure 3.16: Beta functions in one cell of the PAMELA proton ring.

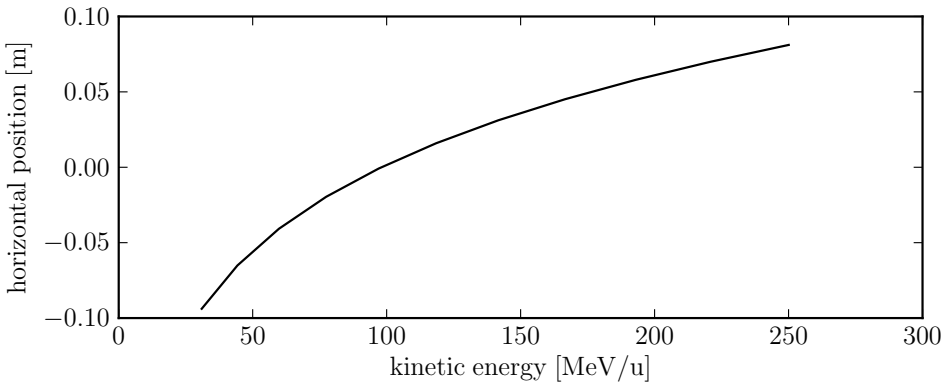

Figure 3.17: Orbit excursion in the PAMELA proton ring.

3.3.1 Alignment error studies

In a similar manner to Section 2.3.3, a study of alignment errors including acceleration was undertaken on this lattice design, in order to show that by avoiding resonance crossing, the large orbit distortion observed in linear ns-FFAGs is also avoided [80].

Gaussian distributed patterns of random horizontal alignment errors were introduced to each magnet in the lattice[1], using 10 different values of the standard deviation σ from 0 to 100 μm in steps of 10 μm. The Gaussian distributions are cut-off at 3σ, which removes very large errors which could have a dominant effect on the dynamics.

For each value of σ, a different random value is applied to each of the lattice magnets and a single particle is tracked to extraction over 1000 turns. The orbit distortion is calculated as the maximum difference between the distorted particle orbit and the orbit of a particle in an error free lattice. This is repeated 10 times for each σ value and the mean and RMS values of the orbit distortion are calculated.

To ascertain the difference in sensitivity to alignment errors between this design and the linear ns-FFAG lattice, the same acceleration rate is used. Acceleration is achieved in 1000 turns with an energy gain of 220 kV/turn. This allows a direct comparison between the results of the different lattice designs. As before, synchrotron motion is neglected as only the transverse dynamics are of interest here and the 'cavities' are represented as zero-length elements providing a simple energy gain.

The amplification factors (as in Eqn. 2.21) are obtained by fitting straight lines to the mean of the distributions shown in Fig. 3.18 and the error on the amplification factor corresponds to the difference between the maximum/minimum linear fit and the central fit. The errors are relatively large as the main contribution to the distortion is the difference between the closed orbits of the error-free lattice and the misaligned lattice, rather than the distortion of the single particle orbit.

The amplification factor in the horizontal direction with acceleration is 5.81 ± 3.95, and in the vertical direction is 9.47 ± 5.13. The alignment tolerances in this machine are considerably more relaxed than in the case of the linear ns-FFAG design in Chapter 2, where the equivalent amplification factors were 336 ± 104 in the horizontal

[1] Alignment errors were introduced using the 'changref' command in ZGOUBI.

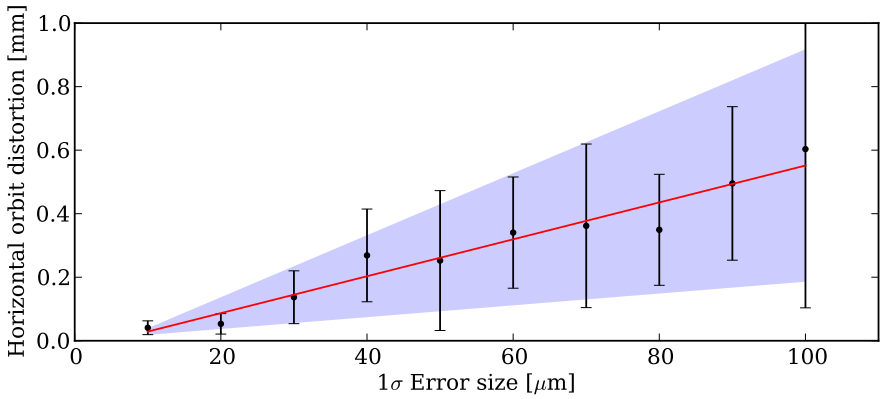

(a) Fitted distribution of horizontal alignment errors

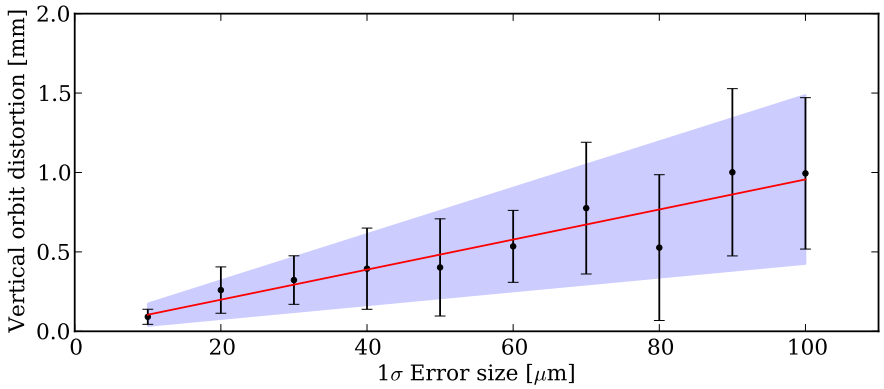

(b) Fitted distribution of vertical alignment errors

Figure 3.18: Orbit distortion as a result of introducing horizontal and vertical alignment errors to the proton ring. The black points correspond to the mean of the 10 runs at each σ value and error bars correspond to the RMS of the 10 runs. The shaded region is the area between the maximum and minimum linear fit, where the central linear fit determines the amplification factor in each case.

direction and 293 ± 136 in the vertical direction. These results indicate that for an allowed orbit distortion of $\approx 1\,\text{mm}$, the alignment tolerances must be better than around $100\,\mu\text{m}$. This tolerance level has been routinely achieved in other accelerators [90].

Distortion near an integer resonance

To check if distortion also arises in this lattice when the total horizontal tune is near to an integer, the varying distortion with total horizontal tune is studied.

To begin with, the field index k and ratio between the D and F magnet strengths are systematically varied by up to 10% in either direction. At each value of k and D/F the closed orbit is found by minimising the phase space area with single particle tracking and the tune is calculated from multi-particle tracking. A set of lattice configurations is then established in which the total horizontal tune varies smoothly between 8.7 and 9.3 at the injection energy, while the vertical tune remains fixed.

For each configuration a random Gaussian distribution of horizontal alignment errors is applied to the lattice magnets, with a standard deviation of 50 μm. A single particle is then tracked through 10 turns without acceleration at each tune value and the maximum distortion calculated as before. This is done 10 times for each tune value and the resulting mean is shown with error bars representing the RMS of the 10 trials. There is a clear increase in the distortion when the tune nears the integer, as shown in Fig. 3.19. This shows that as expected, the tune in this lattice must be kept away from an integer in order to avoid unnecessary orbit distortion.

Multi-particle tracking with alignment errors

Tracking through the full acceleration cycle of the proton lattice was undertaken to show that a realistic emittance beam should emerge from the proton ring with no significant distortion. Horizontal alignment errors were applied to each magnet in the

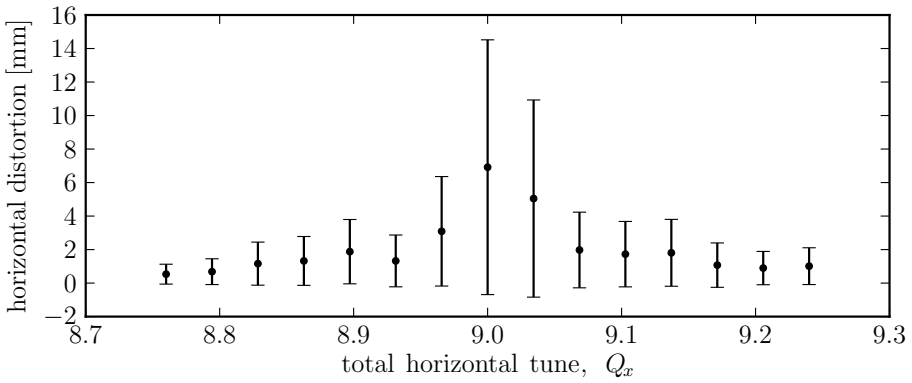

Figure 3.19: Orbit distortion of the proton lattice with 50μm horizontal alignment errors for varying total horizontal tune.

lattice. The applied errors are Gaussian distributed with a 50 μm standard deviation and a cut-off at $3\,\sigma$. Thirty-six particles on a $10\,\pi$ mm mrad emittance ellipse were tracked from 30.95 MeV to 250 MeV in 1000 turns and the emittance re-calculated turn-by-turn. Initial ellipse parameters (Twiss parameters) were determined from multi-particle tracking through a single cell.

The emittance stays constant at $10\,\pi$ mm mrad throughout acceleration, as shown in Fig. 3.20. The small ripples at the start of tracking are due to the slight inaccuracy in determining the centre of the closed orbit and Twiss parameters when alignment errors are included. This demonstrates that the proton lattice design is suitable for the acceleration of beams for CPT with little or no emittance increase throughout acceleration.

3.3.2 Dynamic aperture

The dynamic aperture of this lattice was calculated for the case of rectangular magnets with parallel alignment. The procedure for establishing the dynamic aperture was developed by D. Kelliher, as a co-author of Ref. [85]. The results presented here use the same method but have been re-calculated.

The calculation covers a cell tune range of 0.7 - 0.75 and 0.25 - 0.30 in the horizon-

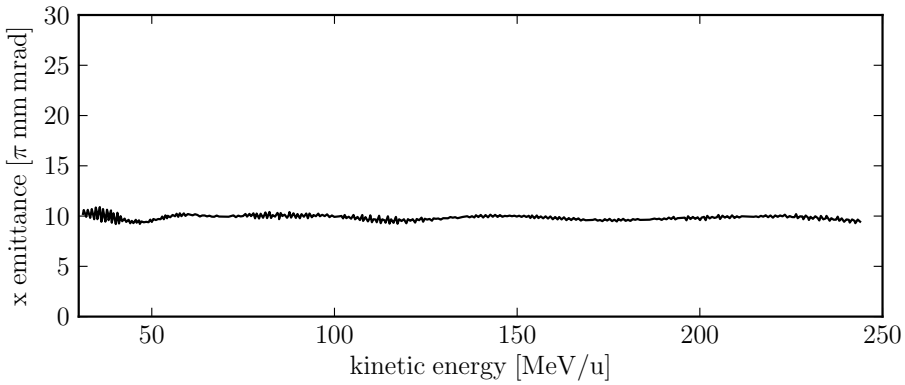

Figure 3.20: Horizontal emittance throughout acceleration in the proton lattice with 50 μm random alignment errors, starting with a 10 π mm mrad ellipse.

tal plane and vertical plane respectively. In each scan, the tune in just one transverse plane is varied while in the other transverse plane it is fixed at the nominal value in Table 3.7. The calculation is made at injection energy to study the case where the beam is at its largest size in physical space. An error-free lattice is assumed and multipole components up to decapole from a polynomial fit to ideal field strength are included. To select a particular value in the tune space, the field index k (and hence the coefficients of each multipole term) and the ratio of the F and D strength are adjusted.

The search for dynamic aperture begins by tracking a single particle over 1000 turns. The particle has identical starting conditions in both planes. In each case the initial coordinate is given by $-\sqrt{2\mathbf{J}/\gamma_{x,y}}$ and the initial angle is zero. $\mathbf{J}$ is the action variable and $\gamma_{x,y}$ is the horizontal or vertical Twiss parameter. The tracking is started at $2\mathbf{J} = 1\,\pi$ mm mrad normalised amplitude and then increased in steps of 1π mm mrad until the particle is lost. The dynamic aperture is given by the highest amplitude particle that survives tracking.

It is clear from the results shown in Fig. 3.21 that it is possible to choose a point in the tune space where the dynamic aperture is more than $50\,\pi$ mm mrad normalised in both transverse planes, which is sufficient for the application of CPT. One of the local

minima in the dynamic aperture results in Fig. 3.21 can be attributed to a coupling between the transverse planes. Since there is no skew quadrupole component present a second order resonance at $\nu_x + \nu_y = 1$ is discounted. Instead the observed coupling is attributed to the octupole term driving a fourth order resonance at $2\nu_x + 2\nu_y = 2$.

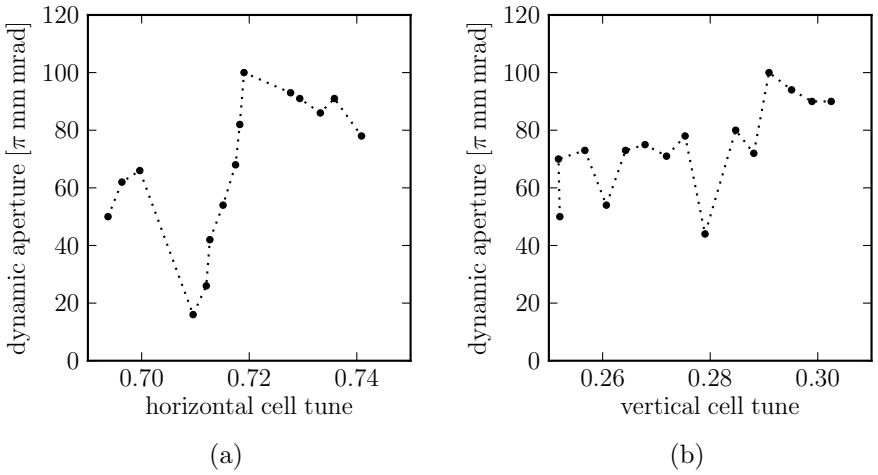

Figure 3.21: Dynamic aperture vs. (a) horizontal cell tune (ν_x), (b) vertical cell tune (ν_y). The optimised lattice of rectangular shaped magnets with polynomial fit to strength is used.

3.4 Summary of proton lattice design

The PAMELA proton lattice design successfully reduces orbit excursion and simplifies magnet design, construction and alignment issues when compared to a scaling FFAG. Both the horizontal and vertical betatron tunes are constrained to within half an integer, avoiding resonance crossing. Furthermore, a study of sensitivity to alignment errors indicates that the design is feasible in terms of alignment tolerances. The design also provides adequate dynamic aperture for the application of CPT.

The PAMELA design requires both protons and carbon at full treatment energy and for this purpose the design outlined here needs to be scaled up to a second ring which can provide C^{6+} ions at 400 or even up to 430 MeV/u. This will be explored

in the next chapter.

Chapter 4

Lattice solution for carbon ions

There is a growing body of clinical evidence that fully stripped carbon ions (C^{6+}) are a more effective ion species for charged particle therapy for some radio-resistant tumours due to their higher cell-killing power compared to protons [91]. As such, the ability to provide full treatment energy C^{6+} ions is an integral feature of next-generation CPT accelerators like PAMELA. This chapter describes the application of the design principles outlined in Chapter 3 to the second ring of the PAMELA complex, the carbon ring.

Ideally the lattice for the carbon ring should follow the same concept as the smaller proton lattice, but poses an even greater challenge as the charge to mass ratio of C^{6+} is only half that of protons. This leads to a higher required energy and higher magnetic rigidity of the particles. The highest rigidity reached by C^{6+} ions at 400 MeV/u is 6.370 Tm; more than double the 2.432 Tm of full energy protons, as outlined in Table 3.1. Nonetheless the ring radius should be much less than double the radius of the proton machine, while maintaining long straight sections for injection/extraction and realistic magnet designs.

Initial considerations and constraints on the lattice are given and each parameter is studied in terms of the geometric effects of scaling up the design. After establishing

a suitable region in the parameter space, the design is then further developed and optimised. The resulting lattice performance is studied in a similar manner to the proton lattice.

4.1 Scaling up the lattice design

4.1.1 Basic considerations

The following requirements are imposed on the design of the carbon lattice:

1. Long straight sections of greater than 1.2 m are required in order to fit the RF system, injection and extraction sections.

2. The total magnetic bore diameter needs to be less than 0.35 m. This is to minimise the ratio of magnet bore to length, where a practical magnet length should be less than about 1 m.

3. The peak magnetic field must be less than 4.5 T to ensure that realistic superconducting magnets can be designed. This is in line with experience from designing the proton lattice.

4. Total tune variation should be less than half an integer in both planes in order to avoid resonance crossing.

5. The radius of the carbon ring needs to be at least 1.5 m greater than the proton ring to allow the possibility of concentric rings.

In order to study the feasibility of designing a carbon lattice that meets these requirements, a scan of the basic parameters is undertaken.

4.1.2 Geometric model and assumptions

As discussed in the design of the proton lattice, a number of parameters can be adjusted to achieve a realistic lattice design, including the ring radius, field index, lattice packing factor and number of cells. It is important to understand the effect that changing each of these parameters has on the peak magnetic field, orbit excursion, magnet bore size and length of long straight sections. Dynamics and optics are considered later, in Section 4.2.

During the following parameter scans, two assumptions are made. First, the field described by the polynomial fit in the lattice magnets is assumed to be close to the ideal r^k law so the particles follow an approximately circular trajectory when inside the magnets. This is also used by Misu *et al.* in Ref. [92] where the author assumes "a constant radius of curvature along an equilibrium orbit for each magnet"[1]. Outside the magnets the particles travel in a straight line. Fringe fields are not considered in the geometric model but play an important role in dynamics and are included after the initial baseline parameters are selected.

Second, as the magnets are in an FDF configuration, it can be assumed that each F magnet needs to provide the total bending required in the cell, as the bending power of one F will be effectively cancelled by the reverse bending of the D. For example, each F magnet must be able to provide 30° bending in a 12-cell lattice. Of course, this also assumes that the F and D magnetic fields are very similar in magnitude (although opposite in sign). In reality the F and D are likely to differ in magnitude by around 10%, but making this assumption gives a reasonable indication of the peak bending field required in the magnets, making it a useful tool at this stage. For this reason the maximum peak field in the parameter scan is set to 4.0 T, which respects

[1]The Misu *et al.* study does not look at the FDF triplet focusing structure and only uses the first stability region of Hill's equation. The model in [92] is not used as the simplified layout of rectangular magnets on a straight line in the present description allows the described geometric model to be implemented.

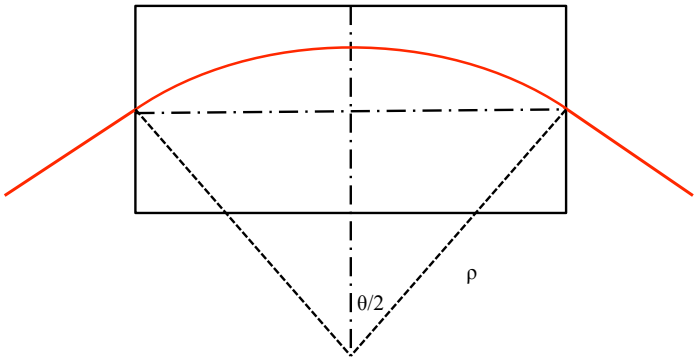

Figure 4.1: Approximate circular trajectory of particles through a magnet of length l_{mag} and dipole field strength B.

the 4.5 T limit once this 10% difference is taken into account.

A set of basic geometric equations can be defined to describe the changing parameters in this type of lattice. To begin with, the bending power of a dipole field is given by Eqn. 4.1, where l_{mag} is the magnet length, B is the magnetic field, ρ is the bending radius (so $B\rho$ is the magnetic rigidity) and θ is the angle through which the trajectory is bent, as shown in Fig. 4.1.

$$\sin\frac{\theta}{2} = \frac{l_{\mathrm{mag}}B}{2(B\rho)} \tag{4.1}$$

$$l_{\mathrm{mag}} = \frac{2\pi\, r_0\, \alpha}{5\, n_{\mathrm{cells}}} \tag{4.2}$$

$$l_{\mathrm{LD}} = \frac{2\pi r_0(1-\alpha)}{n_{\mathrm{cells}}} \tag{4.3}$$

The magnet length l_{mag} is defined as in Eqn. 4.2 and the long drift length l_{LD} in Eqn. 4.3 where r_0 and α are the reference radius and packing factor respectively, as in Chapter 3. The total realistic magnetic length can be extended into the short straight sections keeping the magnetic centre fixed, in order to reduce the peak field, giving a total magnetic length of up to $1.8\, l_{\mathrm{mag}}$. This also slightly reduces the long drift length by $0.8\, l_{\mathrm{mag}}$. The peak magnetic field, B_{max}, can then be calculated by

rearranging Eqn. 4.1.

There are two contributions to the total magnetic bore size, the orbit excursion and a geometric offset. The orbit excursion is defined by the r^k scaling law and is the difference between the radius of the beam trajectory at injection and full extraction momentum, as in Eqn. 4.4.

$$\Delta r_{\text{orbit}} = r_0 \left[\left(\frac{B_{\text{extr}}}{B_0} \right)^{1/k} - \left(\frac{B_{\text{inj}}}{B_0} \right)^{1/k} \right] \tag{4.4}$$

where B_{inj} and B_{extr} are the corresponding field strengths from Eqn. 4.1 using the injection and extraction rigidities of Table 3.1. The geometric offset is the difference between the radius at which the beam enters or exits a magnet and the maximum radius of the beam orbit, as shown in Fig. 4.2.

$$\Delta r_{\text{geom.}} = \rho - \frac{1}{2}\sqrt{4\rho^2 - l_{\text{mag}}^2} \tag{4.5}$$

Given the first assumption that the trajectory is a sector of a circle, the geometric offset can be calculated easily using Eqn. 4.5. The total bore diameter (D_{bore}) is then simply given by Eqn. 4.6.

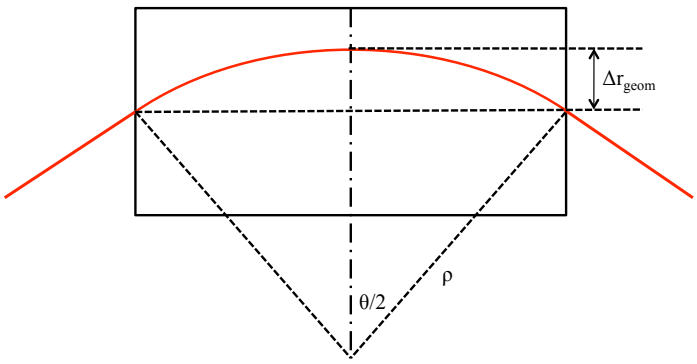

Figure 4.2: Definition of geometric offset for calculation of magnet bore size.

$$D_{\text{bore}} = \Delta r_{\text{orbit}} + \Delta r_{\text{geom.}} \tag{4.6}$$

4.1.3 Variation of lattice parameters

To determine which potential parameter combinations meet the requirements and which do not, solutions of the above equations are plotted using Mathematica^{TM} as regions of suitable lattice configurations, as shown in Fig. 4.3. These calculations are independent of optics and dynamics of the lattice.

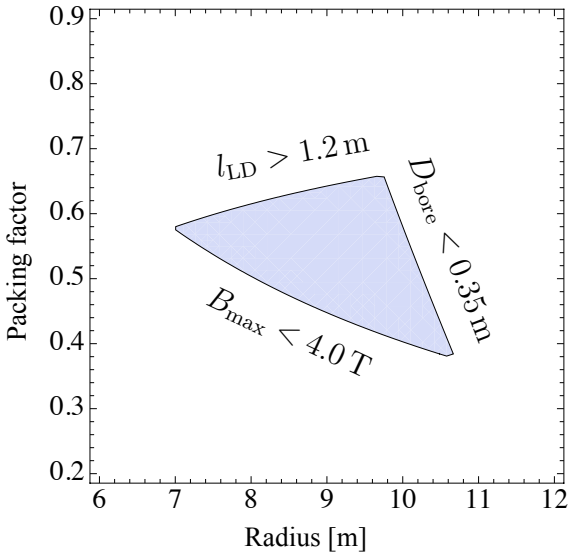

Figure 4.3: Possible regions for carbon lattice design assuming straight sections greater than 1.2 m with a peak magnetic field less than 4.0 T and a magnetic bore less than 0.35 m. The shaded region describes the 'good' region for lattice design.

From Fig. 4.3 a selection of suitable lattice parameters can be made in order to study the variation of magnetic bore size (D_{bore}), peak field required (B_{max}), magnet length (l_{mag}) and other parameters as a function of each relevant variable. The base values selected are $r_0 = 8.5$m, $k = 42$, $\alpha = 0.5$, $n_{\mathrm{cells}} = 12$. Figs. 4.4 to 4.8 show the variation of each parameter, where in each case the only changing variable is the one given on the horizontal axis.

It is clearly shown that while the number of lattice cells does not greatly affect the required maximum bending field strength, factors such as the ring radius and packing factor have a much greater impact, as expected. In a similar manner, the main contribution to the orbit excursion and thus the total magnetic bore size is the field

index, k. The magnet length increases with both the ring radius and packing factor but decreases with the number of cells, while the long straight length is maximised by having a small packing factor, α.

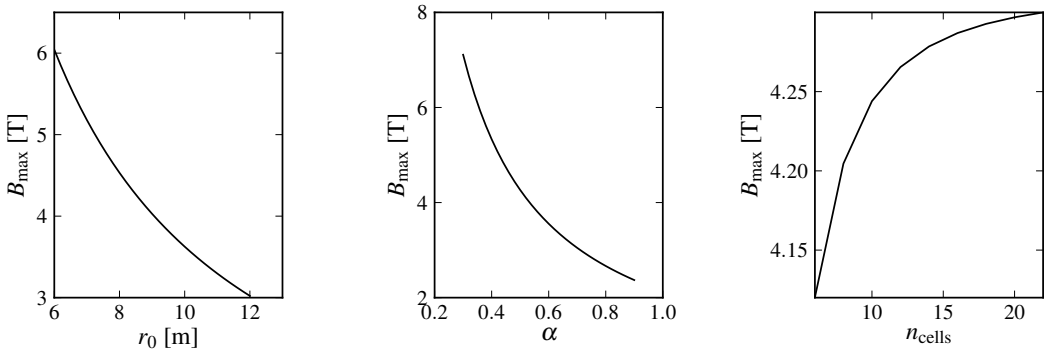

(a) (b) (c)

Figure 4.4: Variation of $B_{\max}$ with (a) machine radius r_0, (b) lattice packing factor α and (c) n_{cells}.

4.2 Baseline carbon lattice

The process of selection of the baseline parameters for the PAMELA carbon lattice necessarily involved consultation with magnet and RF designers. Initial discussions were based on an 8.5 m radius lattice; however high peak fields observed in a preliminary magnet design necessitated an increase in radius. After a number of iterations a 9.3 m radius was selected to lower the peak current on the superconducting wires in the magnet design. A description of the principles of the magnet design can be found in Ref. [93] and these are discussed briefly in Chapter 6.

From the point of view of lattice dynamics this does not make a significant difference. As the packing factor is increased in the 8.5 m lattice design to allow for longer magnet lengths and lower peak fields, the two stable regions move away from each other, as was observed in Section 3.1.1. This is shown in Fig. 4.9, where the green second stable region becomes separated from the red first stable region with increas-

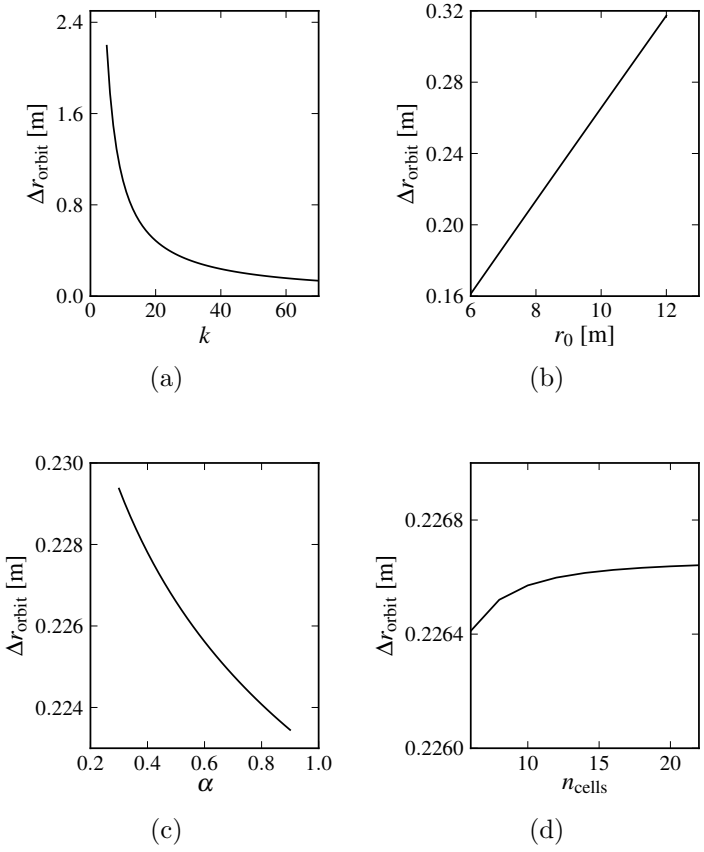

Figure 4.5: Variation of orbit excursion during acceleration $\Delta r_{\mathrm{orbit}}$ with (a) field index k, (b) machine radius r_0, (c) lattice packing factor α and (d) n_{cells}.

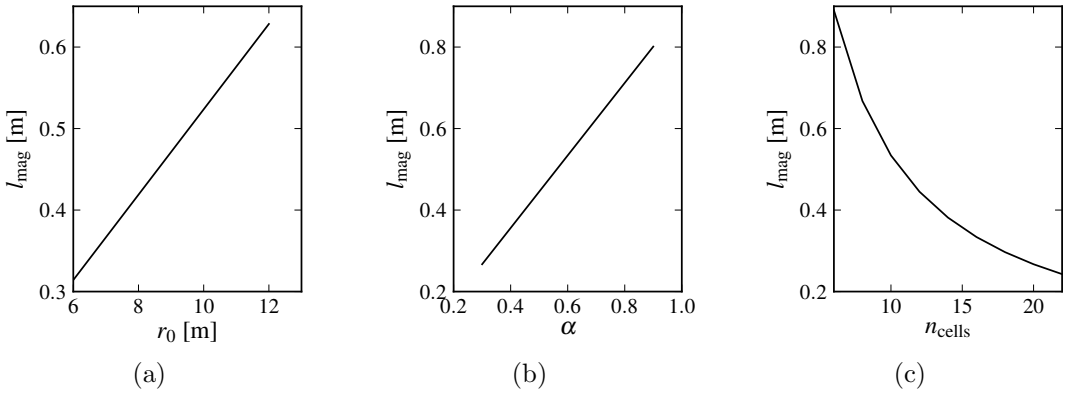

Figure 4.6: Variation of l_{mag} with (a) machine radius r_0, (b) lattice packing factor α and (c) n_{cells}. This is the idealised magnet length, the real magnet length may be up to a factor of $1.8\,l_{\mathrm{mag}}$.

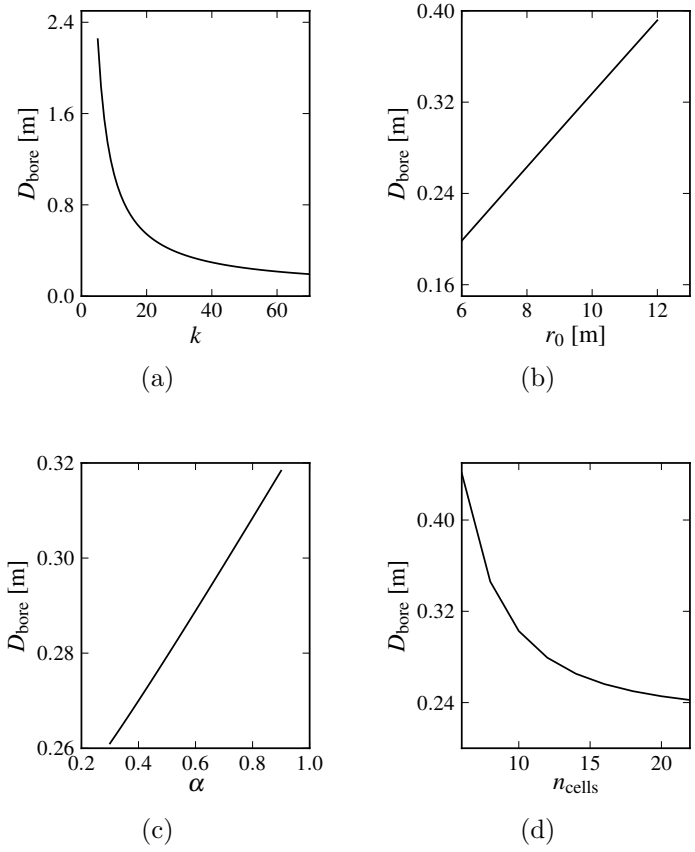

Figure 4.7: Variation of D_{bore} with (a) field index k, (b) machine radius r_0, (c) lattice packing factor α and (d) n_{cells}.

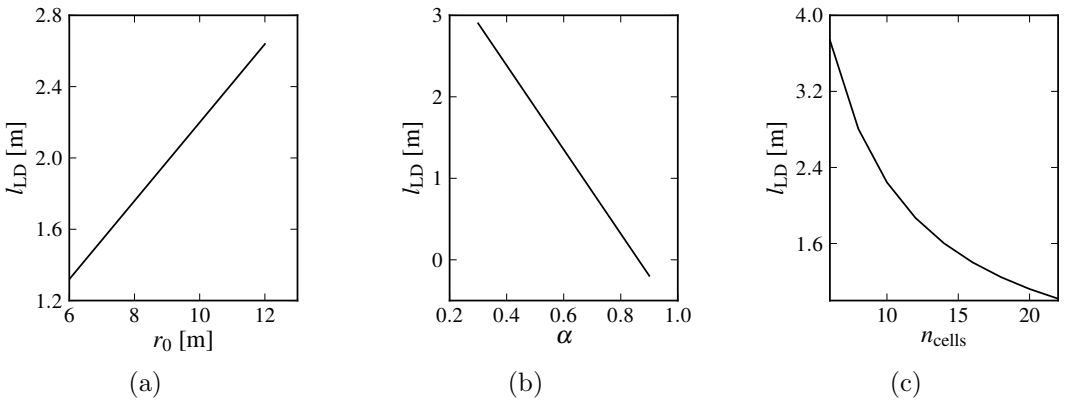

Figure 4.8: Variation of long drift length l_{LD} with (a) machine radius r_0, (b) lattice packing factor α and (c) n_{cells}. This is calculated in each case with a magnet length of $1.8\,l_{mag}$.

ing packing factor. With the increase in machine radius to 9.3 m for a packing factor of 0.65 in Fig. 4.10, the stable regions look very similar and the difference between the β functions in the first and second stable regions will be comparable to that of the 8.5 m lattice.

The optimisation procedure in Section 4.3 is carried out for the 9.3 m carbon lattice design, as this was deemed the most likely feasible solution. For this configuration, the lattice parameters are outlined in Table 4.1.

Parameter	**Value**
Radius	9.3 m
Lattice packing factor	0.65
Circumference	58.4 m
Approximate k value	42
Long straight	1.1979 m
Short straight	0.1266 m
Magnet length	1.1395 m
Orbit shift	0.217 m
Bore size	0.35 m

Table 4.1: Lattice parameters of the baseline lattice.

4.3 Optimisation

The optimisation follows the same method used for the proton lattice and begins by calculating the positions of particle orbits throughout acceleration in a perfectly scaling version of the FFAG. The non-scaling version then takes the middle point of the orbit excursion within each magnet as the central point of the polynomial fit, in order to achieve the best possible fit of the multipole coefficients to Eqn. 2.15 in the region of magnetic field that the beam experiences. Outside the region that the beam traverses, the magnetic field is allowed to be different from Eqn. 2.15. In Cartesian co-ordinates the expansion of the field takes the form of Eqn. 4.7, where x_0 is used instead of r_0 of Eqn. 2.15, the distance from the centre of the machine to the centre

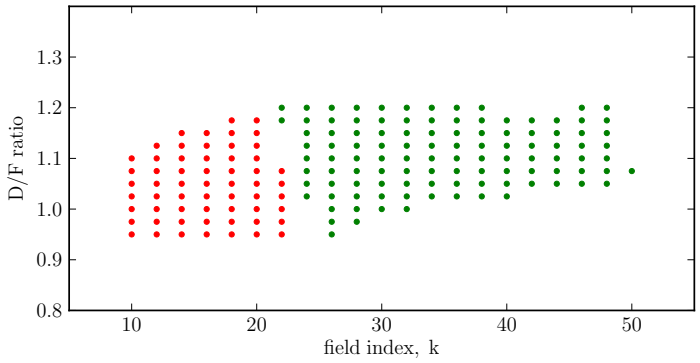

(a)

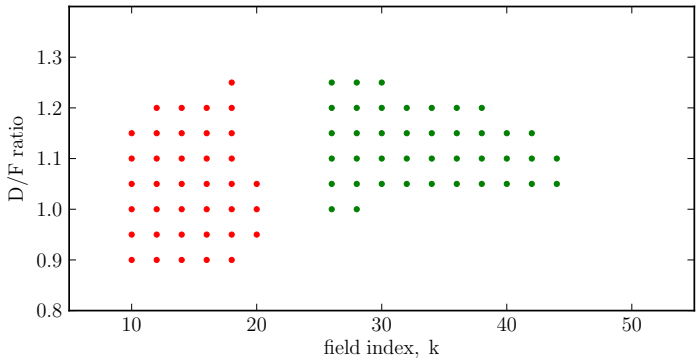

(b)

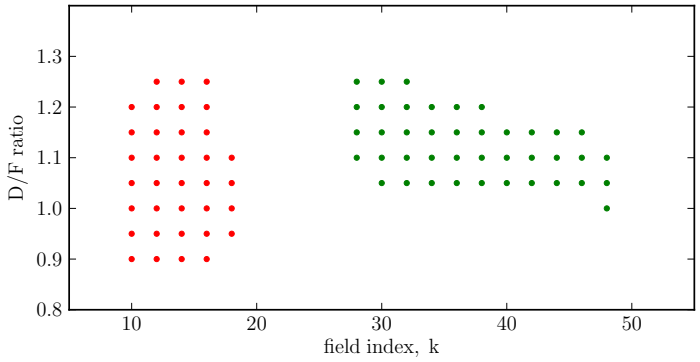

(c)

Figure 4.9: Stable working points for the 8.5 m carbon lattice design when the packing factor is changed from 0.5 in (a) to 0.6 in (b) and to 0.65 in (c). The second stable region is shown in green.

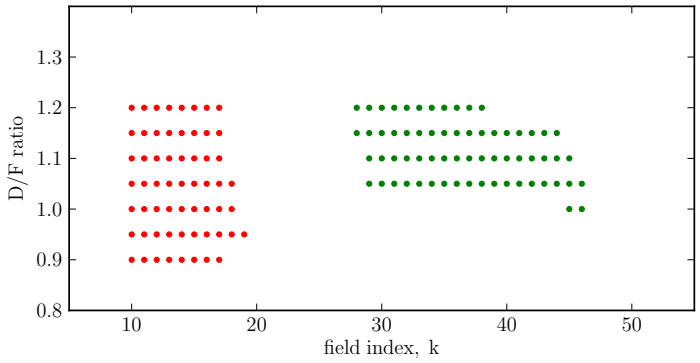

Figure 4.10: Stable working points for the 9.3 m carbon lattice design with a packing factor of 0.65. The second stable region is shown in green.

of the magnet.

$$B_y = B_{y,0}\left(1 + \sum_{n=1} \frac{1}{n!} \frac{k(k-1)\cdots(k-n+1)}{x_0^n} x^n\right) \tag{4.7}$$

4.4 Performance

Optics and orbit

The beta functions at the reference momentum in one cell of the carbon lattice as calculated with SCode are shown in Fig. 4.11. The total orbit excursion throughout acceleration is shown in Fig. 4.12. The total change in orbit position between the lowest and highest energy orbits is 21.7 cm for the energy range required. A larger energy range is achievable with the same lattice design, for example an energy range of 50 to 430 MeV/u is possible with a total orbit excursion of 23.7 cm. The final choice of energy range will depend on both clinical considerations and the magnet and RF designs, as the aperture of these components will determine the allowed orbit excursion.

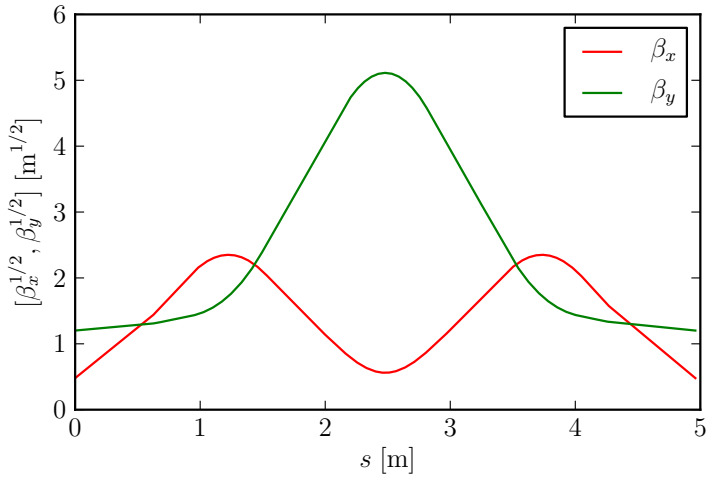

Figure 4.11: Beta functions in one cell of the carbon lattice as calculated with SCode.

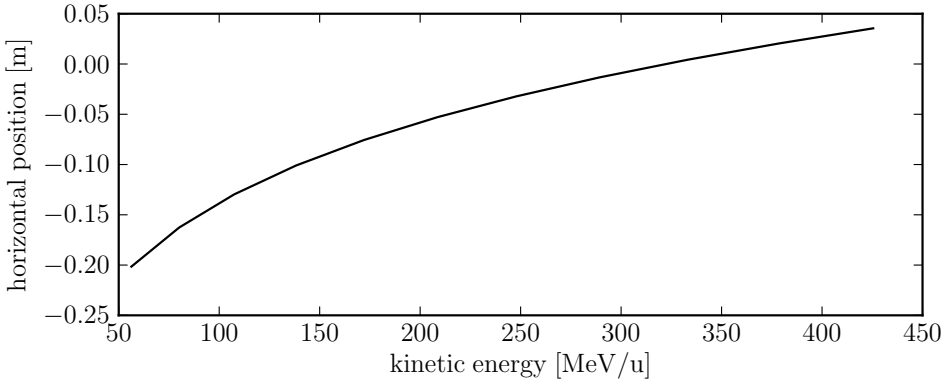

Figure 4.12: Variation of orbit position in the horizontal direction during acceleration.

Tune variation

The variation of betatron cell tunes throughout acceleration is shown in Fig. 4.13 for varying orders ($n = 3, 4, 5$) of polynomial fit to Eqn. 2.15 corresponding to the number of magnetic multipoles employed (up to octupole, decapole and dodecapole respectively). The total machine tune variation for each case is given in Table 4.2. In each case, including the simplest case of multipoles up to the octupole, the tune variation is less than half an integer. The operating point can be shifted to avoid the

half-integer resonance currently crossed at high momentum in the octupole case.

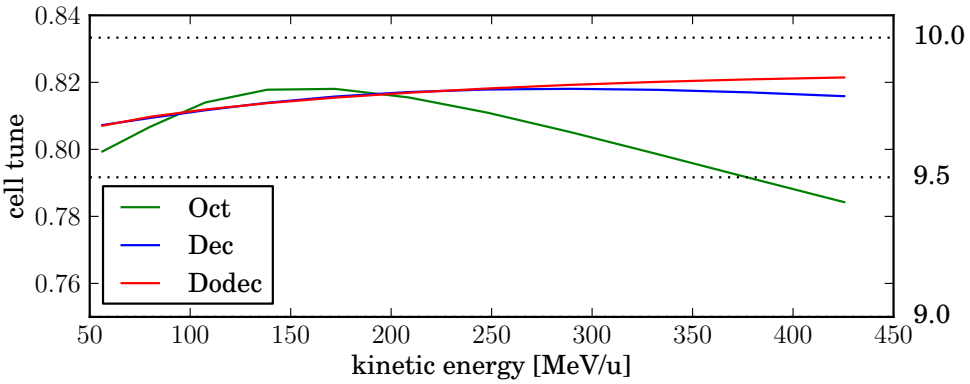

(a)

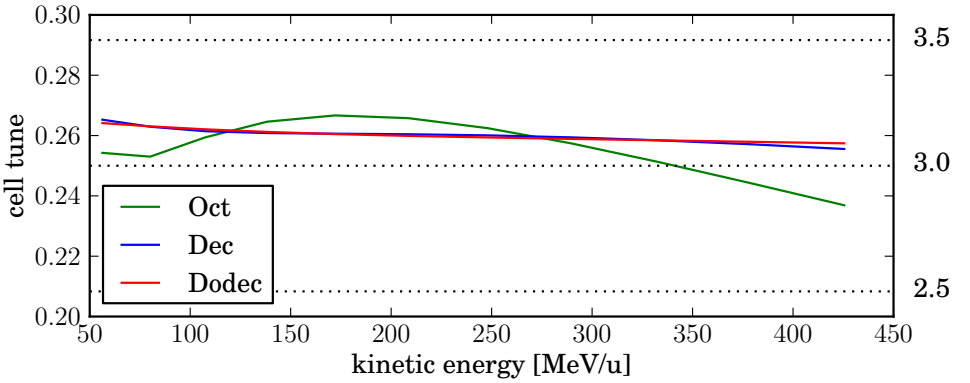

(b)

Figure 4.13: Variation of horizontal cell tune (a) and vertical cell tune (b) for different orders of multipoles. Dotted lines correspond to integer and half integer resonances of the total machine tune.

Multipole order	ν_x	ν_y	Q_x	Q_y
Octupole	0.0338	0.0298	0.4056	0.3574
Decapole	0.0108	0.0097	0.1297	0.1165
Dodecapole	0.0144	0.0067	0.1727	0.0805

Table 4.2: Variation of cell ($\nu_{x,y}$) and total ($Q_{x,y}$) tune for different orders of polynomial fit to the ideal field profile.

Dynamic aperture

The dynamic aperture is calculated using the method outlined in Section 3.3.2 at the injection energy (68.36 MeV/u) for a range of horizontal and vertical tunes, determined by changing the k value and ratio between the F and D strengths. The optimised carbon lattice using a polynomial fit up to decapole is assumed with no alignment errors present. Single particles are tracked over 1000 turns, starting with the same normalised amplitude in both horizontal and vertical planes. The amplitude is then increased until the particle is lost, and the dynamic aperture plotted next to each point in Fig. 4.14 is the highest amplitude surviving particle in units of π mm mrad normalised. In this case the dynamic aperture is greater than $50\,\pi$ mm mrad for most tune values, which is sufficient for this application.

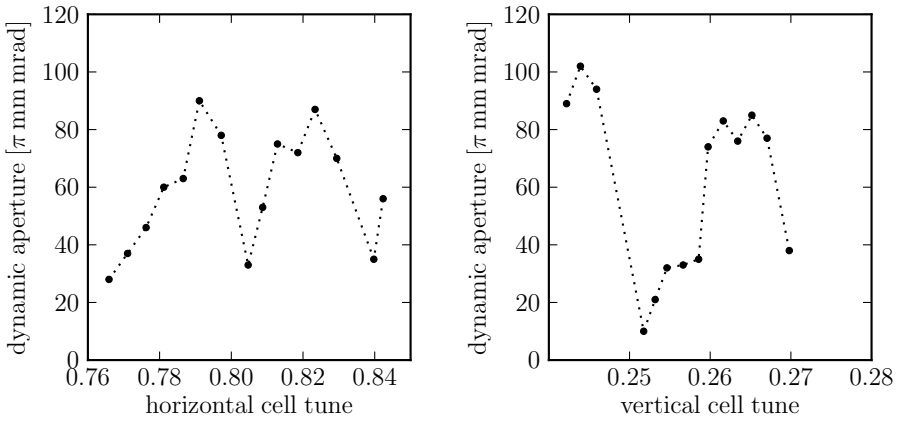

Figure 4.14: Dynamic aperture vs. (a) horizontal cell tune (ν_x), (b) vertical cell tune (ν_y).

4.5 Summary of carbon lattice design

The carbon lattice design has successfully scaled up the non-linear ns-FFAG idea from the proton lattice, varying the lattice parameters in order to adapt the design

to the more challenging specification. Despite the changes in lattice parameters, the betatron tunes remain constrained to within half an integer and the orbit excursion remains small. In fact, the lattice is able to operate over a larger energy range than initially conceived, a potential advantage if the engineering design of the main RF, magnet and injection/extraction systems can accommodate the slightly increased aperture that this would require. The dynamic aperture remains sufficient for the application.

There remain challenges in the engineering design of the major components. Ongoing work on these components is discussed in Chapter 6.

The next stage in the design of PAMELA is an important one; to make sure that the real beam dynamics in a ns-FFAG are close to those produced by the simulation code[2]. For this reason Chapter 5 focuses on EMMA (Electron Model of Many Applications), the world's first ns-FFAG and results obtained during the initial beam commissioning of this machine.

[2]Further verification of the lattice design is also considered by tracking accurate 3D field maps from realistic magnet designs, which is discussed in Chapter 6.

Chapter 5

The EMMA experiment

The CONFORM project, of which PAMELA is one of three branches, aims to demonstrate the feasability of ns-FFAG technology. A crucial part of this programme is the design and construction of the first ns-FFAG accelerator, the 'Electron Model of Many Applications' (EMMA). Originally, the construction of EMMA was scheduled to be completed toward the end of 2009 [94]. However, it became clear in late 2009 that the original construction schedule would not be met and that waiting for the full EMMA ring to be finished was likely to cause a significant delay in the completion of this thesis.

As a result, it was proposed to begin commissioning of EMMA with an incomplete ring: the 'four sector' commissioning described in this chapter. This proposal was adopted by the EMMA collaboration with enthusiasm and leadership of the task was granted to the author. The planning, experimental work and methods for this stage of commissioning were developed by the author in collaboration with the commissioning work package leader.

Rather than delay the completion of the full EMMA ring, this experimental work was undertaken in parallel with construction during successive 8-hour shifts. This early stage of commissioning has proven to be extremely valuable, particularly in

terms of establishing an accurate beam injection setup and in understanding the operation of EMMA. This has made a substantial impact in the commissioning of the full EMMA ring. In fact, when the full ring was completed it took less than a month for a number of key commissioning milestones to be met, discussed in Section 5.5.

The main aim of this chapter is to connect the commissioning of EMMA with the design of PAMELA through the comparison of experimental results with the ZGOUBI simulation code, used in the design of both.

5.1 Overview of EMMA

EMMA is an interesting accelerator project as it is the first ns-FFAG ever to be constructed. It is located at the STFC Daresbury Laboratory in the UK and commissioning activities began in June 2010. A brief overview is given here to provide a background to the experimental measurements presented in this chapter. More complete descriptions of EMMA can be found in [94, 95, 96, 97].

The EMMA accelerator has been built as a proof-of-principle demonstrator for ns-FFAG technology. The project aims to demonstrate feasibility of ns-FFAGs and to study the novel beam dynamics of these machines in detail. The availability of the partial EMMA ring in the initial stages of commissioning allowed measurements to be made which are relevant to PAMELA as they contribute to the validation of the ZGOUBI simulation code. This code was used both for the EMMA design and the EMMA on-line model[1], and has been used extensively in the design of PAMELA. The results of the relevant commissioning experiments are presented and their implications discussed.

[1]The on-line model is a graphical user interface under development which will be available in the control room to enable operators to simulate the accelerator at the same time as operating the real machine [98].

5.1.1 EMMA - the Electron Model of Many Applications

Three main features differentiate EMMA from the non-linear ns-FFAG designs in the two previous chapters. The first is that EMMA accelerates electrons, rather than protons or ions, from 10 to 20 MeV, which means that the electrons are ultra-relativistic. Second, it is a linear type of non-scaling FFAG, composed only of quadrupole magnets with a radial offset to provide the dipole bending field. In this respect it is quite similar to the linear ns-FFAG lattice discussed in Chapter 2. The third main difference is that EMMA has extremely rapid acceleration; it will accelerate electrons from $10 - 20$ MeV in tens, rather than thousands of turns. This rapid acceleration appears to be fast enough to avoid beam deterioration due to resonance crossing [63]. In fact, the acceleration itself is a novel 'serpentine acceleration' scheme, a description of which can be found in Ref. [99].

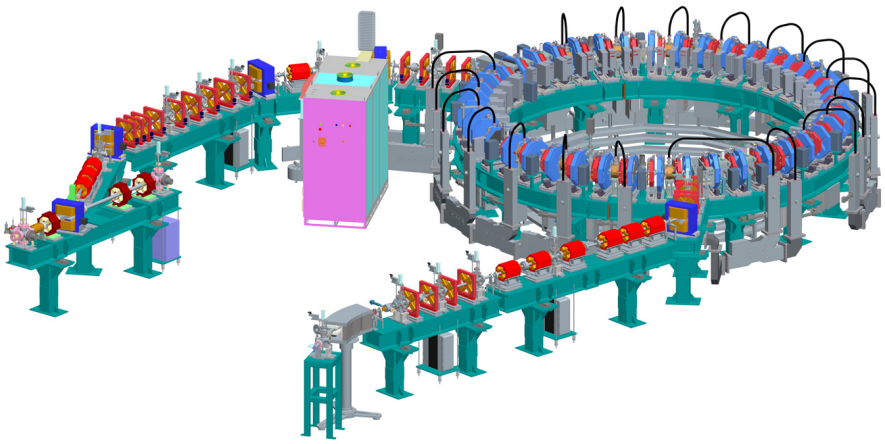

Figure 5.1: 3D schematic of the EMMA ring including injection line (top left) and diagnostic beamline (bottom right).

The main EMMA parameters are given in Table 5.1 and a 3D schematic of the machine is shown in Fig. 5.1. The layout of EMMA with its injector, ALICE (Acceler-

ators and Lasers In Combined Experiments) is shown in Fig. 5.2. ALICE is an existing facility which consists of a 35 MeV electron energy recovery linac prototype [100]. During EMMA operation the two linac sections of ALICE (the booster linac and main linac) are used to provide appropriate beams for the 10 to 20 MeV energy range of EMMA. The electron beam is diverted out of ALICE to the EMMA injection line and so ALICE does not run in energy recovery mode during EMMA operation. Details of ALICE and its setup for EMMA can be found in Refs. [101, 102, 103].

Parameter	**Value**
Radius	2.637 m
Circumference	16.57 m
No. of cells	42
Cell type	DF doublet
Cell length	394.5 mm
RF	19 cavities; 1.3 GHz
Energy range	10 to 20 MeV

Table 5.1: Lattice parameters of the EMMA accelerator.

In preparation for EMMA, a number of methods were developed into high-level software specific to non-scaling FFAGs including measurement of the phase space and aperture scanning algorithms. These methods differ from those of synchrotrons due to the shifting orbit in non-scaling FFAGs and are also applicable to PAMELA. They are described in Appendix A.

5.2 Experimental method

EMMA consists of 42 cells which are physically organised into seven sectors, with six cells in each sector as seen in Fig. 5.3. For the experimental work outlined in this chapter, only four of the seven sectors of EMMA were used, as discussed earlier.

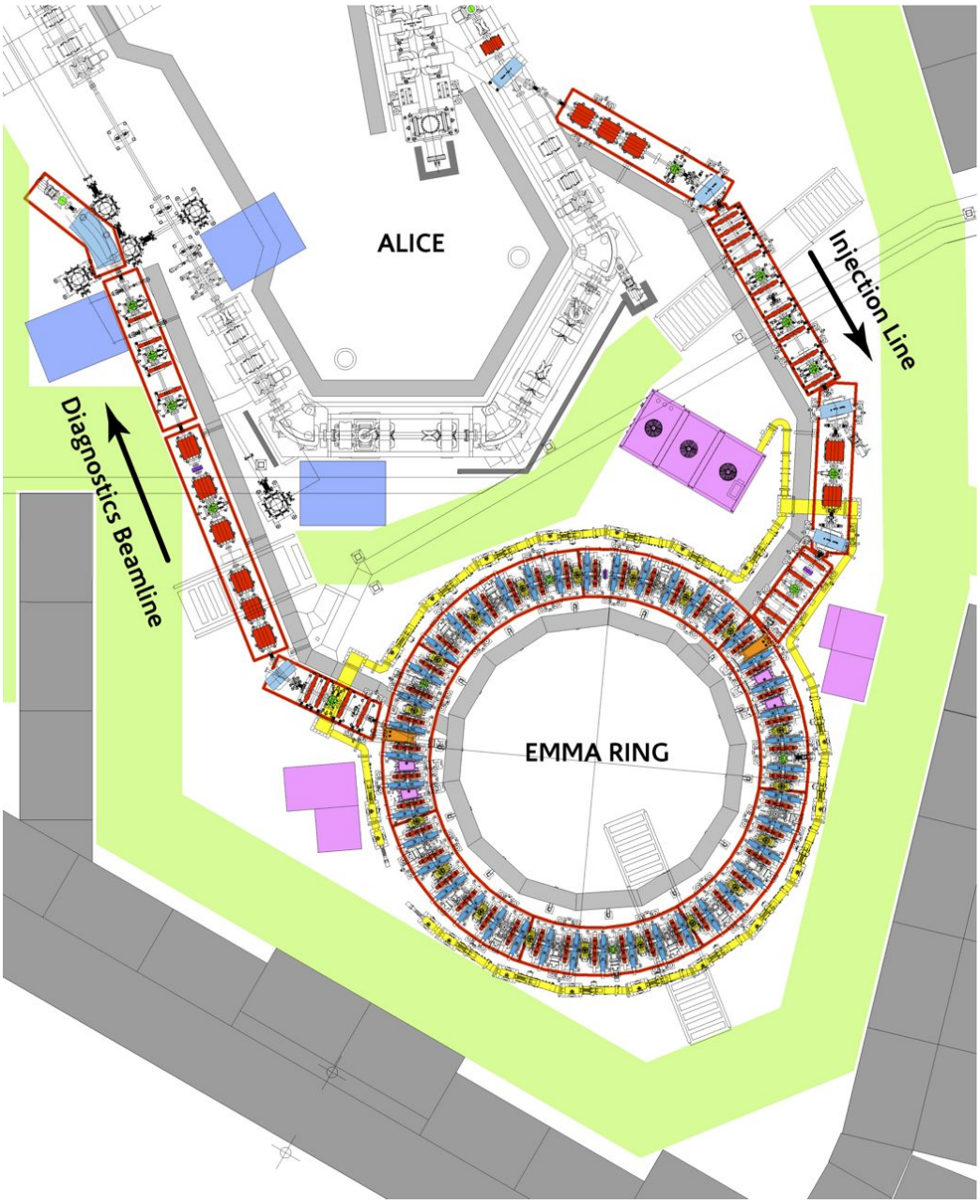

Figure 5.2: Layout of the ALICE and EMMA accelerators.

5.2.1 Four sector setup

The naming convention and layout of cells, diagnostics and other components is shown in Fig. 5.4 and will be used hereafter to refer to EMMA components. In the four sectors there is one YAG screen in Cell 5 and one in Cell 23, the details of which can be found in Ref. [104]. There are a large number of beam position monitors (BPMs) installed, with either two or three BPMs per cell.

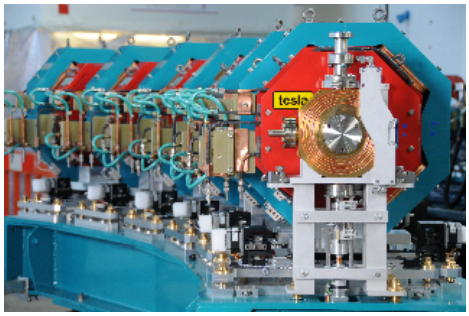

Figure 5.3: One of seven EMMA sectors comprising six DF magnet doublet cells.

In planning the experimental commissioning work the decision was made to keep the beam energy of the ALICE injector constant and to represent different relative momenta by changing the EMMA quadrupole strengths while maintaining the ratio between the D and F quadrupoles (the D/F ratio). This means that to reproduce the dynamics of a relative momentum of +5% the main quadrupole magnet strengths have to be changed by −5%[2].

[2]This change is not immediately obvious. As $B\rho \propto pc$, usually for constant B (in a fixed field accelerator) pc is increased and the bending radius ρ increases proprtionally. In this case we keep pc constant but want to mimic the increase in ρ, hence B is reduced.

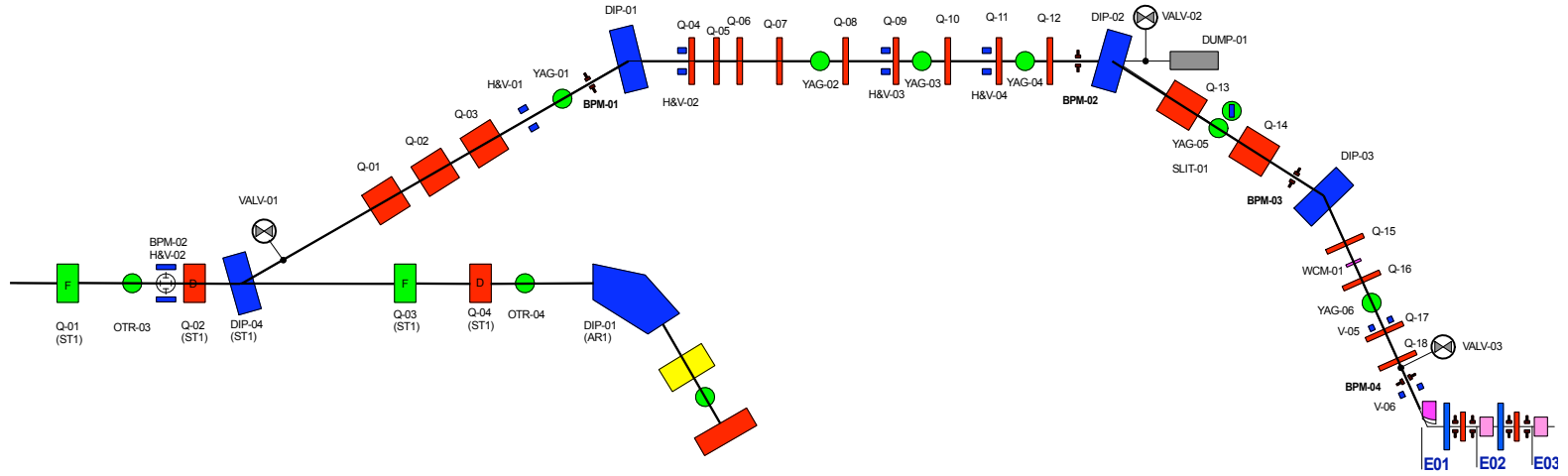

(a)

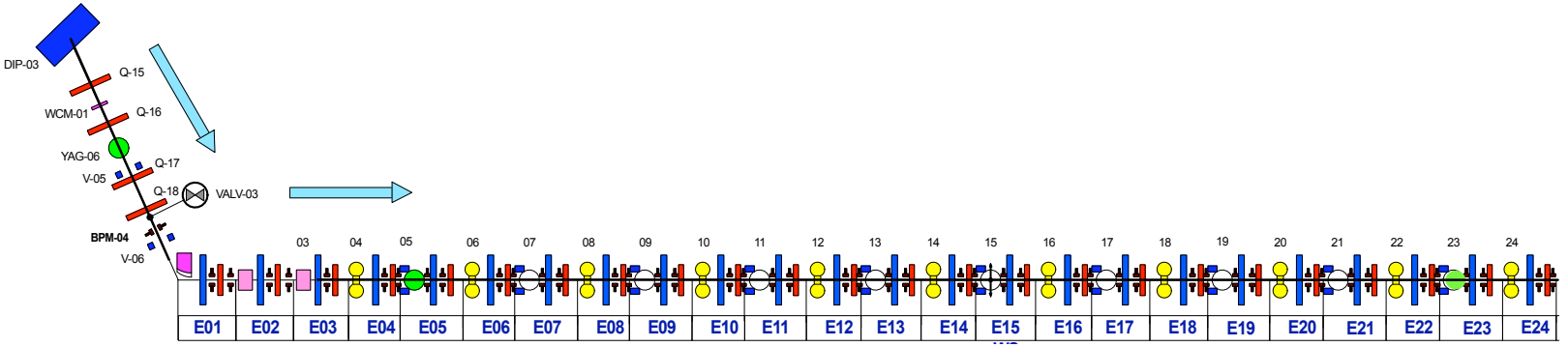

(b)

Figure 5.4: Naming conventions for the EMMA injection line (a) and for the four sectors of EMMA (b).

5.2.2 Beam position monitors

The EMMA ring is heavily instrumented with diagnostic devices as it is an experimental machine with novel beam dynamics that need to be studied in detail. The full EMMA Beam Position Monitor (BPM) system consists of 81 button BPMs. Each BPM includes a button electrode pickup and a pair of front-end modules connected via a single low loss cable 40 m in length to a VME module[3], where the pickup signals are measured using analog to digital converters (ADCs) [105]. Further information about this system can be found in Refs. [106, 107].

During the initial commissioning process the electronic BPM readout system was not yet available. To read positions from the installed BPMs, seven coaxial cables were available which were connected directly from the BPMs to the control room where the analog signals were monitored using a Tektronix TDS6124C oscilloscope. For each BPM, the left-right signals are multiplexed onto the same cable with a set time delay, which is one of the main functions of the front-end module [105]. This means that the horizontal position can be read from a single cable, and similarly for the top-bottom signals for the vertical position. The oscilloscope was used to read out the raw voltage signals from the BPMs and beam positions were calculated from these raw values using a pre-measured calibration algorithm [108]. An example of the traces of three left-right BPMs is shown in Fig. 5.5.

With a total of just seven coaxial cables the amount of data taken was limited during this period, as each cable can only supply either a horizontal or vertical position. In other words, only three BPMs with both horizontal and vertical positions and one with either horizontal or vertical position can be connected at any one time. A machine shut down is required in order to change which BPMs are connected, so such changes are minimised during the commissioning shifts.

During the measurements in Section 5.4 only horizontal BPMs were connected to

[3]Versa Module Europa (VME)

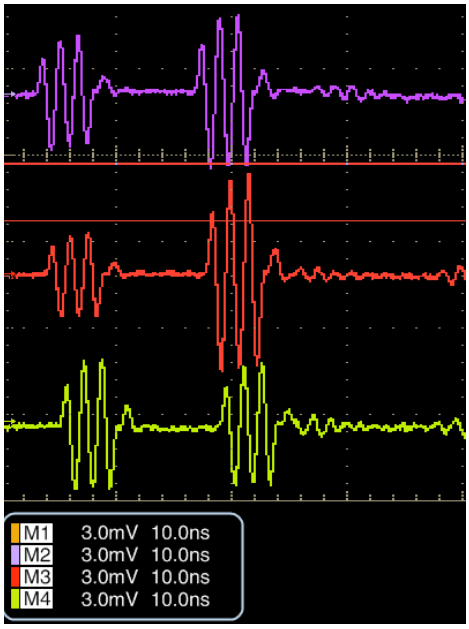

Figure 5.5: Example of BPM traces where the left-right signals are multiplexed onto the same cable for each BPM. Each coloured trace clearly shows two signals (left and right) with a difference in amplitude - this difference gives the horizontal position.

give the maximum of 7 horizontal positions simultaneously. The vertical offset prior to the injection septum was minimised using the vertical correctors in the injection line, though only to within a few mm.

5.2.3 Dispersion measurement

To measure the dispersion, repeated measurements of the beam orbit are taken while varying the relative momentum of the beam. The dispersion is then calculated by rearranging Eqn. 2.10, as:

$$D(p,s) = x(s)\left[\frac{\delta p}{p_0}\right]^{-1}. \tag{5.1}$$

For this measurement the horizontal readouts of the BPMs situated between the D and F magnets in cells E12 to E18 are connected. The measurement is made well after the septum and kickers to allow the betatron oscillations to become roughly constant in amplitude.

5.2.4 Tune measurement

The measurement of the betatron tune in a ns-FFAG is a challenge, particularly with an incomplete ring. The lack of a reference 'closed orbit' to compare particle positions against means that an assumption has to be made about where the centre of the betatron oscillations ought to lie. In most cases, the mean of the measured particle positions is sufficient. In practice this may introduce problems if the beam has large oscillations or is clipped due to beam loss which could skew the position measurements. This is a problem specific to this type of machine as the beam is designed to be off-centre in the beam pipe and this off-centre position changes with energy. Measurements may be improved by minimising betatron oscillations to avoid beam loss.

An additional challenge in measuring the tune with only four sectors of EMMA is the small number of BPM readings available. Fourier analysis relies on a large number of BPM readings so is not reliable in this instance. The method adopted is a least squares fit to a sine wave.

In this method, it is assumed that the data points follow a curve of the form:

$$f(s) = A.\sin(\frac{2\pi\nu_x s}{l_{cell}} + \phi) + \Delta x \tag{5.2}$$

where l_{cell} is the design cell length[4] (394.5 mm). The remaining four variables, A, the amplitude of the oscillations, ν_x the horizontal cell tune, ϕ the phase and the horizontal offset of the 'orbit' from the centre of the BPMs, Δx, are all used as free parameters to make the least squares fit.

[4]It is assumed in the tune measurements that the real distance between the BPMs is the same as the design cell length.

5.3 ZGOUBI simulations and expected results

5.3.1 The ZGOUBI code

The ZGOUBI simulation code has existed since 1972 [109], having undergone major development in the 1990s to make it into a more generalised ray-tracing code. It computes the trajectories of an arbitrary number of charged particles through both electric and magnetic fields. ZGOUBI comes equipped with analytical models of many different types of elements, both magnetic and electric, while allowing for the use of both 2D and 3D field maps in Cartesian or cylindrical co-ordinates. It can accommodate acceleration and tracking simultaneously, as well as calculating synchrotron radiation, spin and in-flight decay processes, although the latter three are not utilised here. Importantly, this is not a new simulation code and has been used for accelerator and spectrometer design for many years. It is one of only a few codes which can accurately simulate FFAGs and has been upgraded for this purpose [110].

5.3.2 Simulating the EMMA experiments

EMMA has been simulated using ZGOUBI with a hard-edge magnet model. The geometry considered is the baseline lattice, which corresponds to one of eight different lattice configurations proposed as part of the EMMA experiment [111]. The lattice parameters used in this instance (additional to those in Table 5.1) are given in Table 5.2.

The ZGOUBI element chosen in this case is the QUADRUPO element, which represents a basic quadrupole with optional fringe fields, described in detail in Ref. [75, p.110]. To ascertain the tunes and dispersion which ought to be observed during the EMMA four sector commissioning, closed orbits were found by locating the centre of the minimised phase space ellipse with multi-turn single particle tracking. These closed orbit positions are plotted relative to a small change in momentum in Fig. 5.6.

Parameter	Value
D offset	34.048 mm
F offset	7.514 mm
Long drift	210 mm
Short drift	50 mm
Quad length F	58.782 mm
Quad length D	75.699 mm
Quad radius (inscribed) F	37 mm
Quad radius (inscribed) D	53 mm
Quad gradient F	6.695 T/m
Quad gradient D	4.704 T/m

Table 5.2: Parameters used to describe the EMMA accelerator in ZGOUBI.

In the small momentum range being considered, the dispersion can be approximated as linear in order to make a comparison with the experimental data. The dispersion is estimated by the gradient of a least-squares linear fit, the result of which is $D(s) = 53.9 \pm 0.52\,\mathrm{mm}$. The betatron tunes were also calculated at each momentum step, shown in Fig. 5.7. These results provide a point of comparison with the experimental data obtained in the next section.

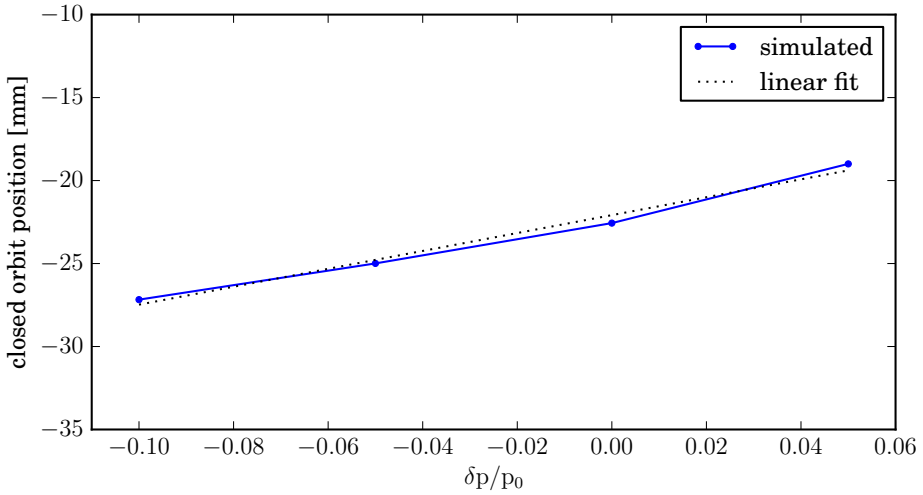

Figure 5.6: Simulated change of closed orbit position with momentum using ZGOUBI.

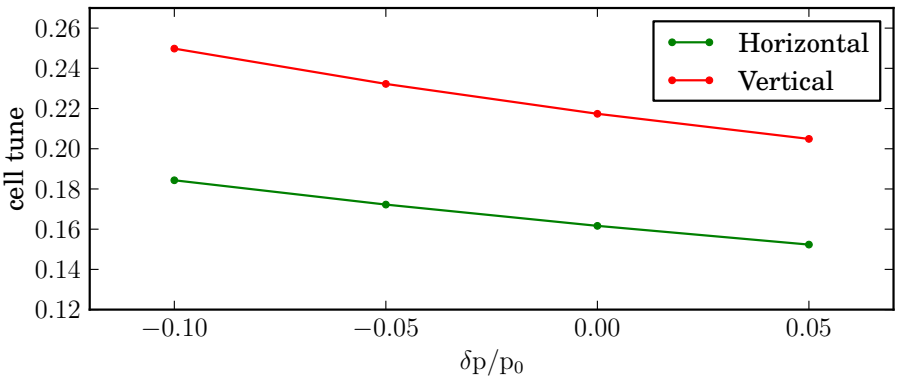

Figure 5.7: Simulated tunes for the baseline EMMA lattice using a hard-edge model in ZGOUBI.

5.4 Experimental results

The following measurements were taken on the evening of 5th August 2010. ALICE was tuned for EMMA injection and the main ALICE parameters during operation are shown in Table 5.3.

Parameter	**Value**
Beam energy [MeV]	15.0
Charge [pC]	40
Repetition rate [Hz]	3.0

Table 5.3: Parameters of ALICE during commissioning of EMMA four sectors.

It should be noted that this was only the second time that beam had been taken all the way through the four sectors of EMMA. On the first occasion (in June 2010) it was observed that the measured position and angle of the beam emerging from the septum were not as expected. A substantial amount of effort was dedicated to mapping the transport properties of the injection line and septum region in order to improve the injection scenario. The measurements presented here were taken after this work was completed. Full optics matching and optimisation of the injection scenario will be undertaken when the whole EMMA ring is available.

5.4.1 Horizontal particle positions

Horizontal particle positions in cells E12 to E18 were measured three times, changing the strength of the injection septum and kicker timing in each instance to try to optimise the injection scenario and minimise betatron oscillations. This was done starting at nominal D/F strengths which mimic a momentum of 18.5 MeV/c and was then repeated for different relative momenta. The settings for each run are given in Table 5.4, where K1 and K2 are the first and second kicker delay timings and QD/QF are the D and F quadrupoles of the main ring. The measured positions for relative momenta of 0.9, 0.95, 1.0 and 1.05 are shown in Figs. 5.8 and 5.9. The error bars shown on each point are an estimated measurement error, determined from repeated measurements of the beam position in a single BPM, which change slightly each time due to beam fluctuations and small errors in reading the oscilloscope traces. The error was taken as the RMS value of these repeated measurements and includes the error on the alignment of the BPMs, which is known to within 250 μm [108].

p/p_0	**QD/QF [V]**	**K1 [V]**	**K1** [μs]	**K2 [V]**	**K2** [μs]	**Septum [V]**
1.0	260/220	7.70	19.762312	6.70	19.761960	6.63
1.0	260/220	7.70	19.762312	6.70	19.761948	6.63
1.0	260/220	7.70	19.762312	6.70	19.761948	6.65
0.90	286/242	7.70	19.762311	6.70	19.762086	6.87
0.90	286/242	7.70	19.762311	6.70	19.762086	6.89
0.90	286/242	7.70	19.762310	6.70	19.762086	6.86
0.95	273/231	7.70	19.762310	6.70	19.762106	6.84
0.95	273/231	7.74	19.762310	7.94	19.762106	6.81
0.95	273/231	6.60	19.762284	6.00	19.762191	7.06
1.05	247/209	8.00	19.762312	8.00	19.762131	6.75
1.05	247/209	6.60	19.762284	7.00	19.762116	7.03
1.05	247/209	6.60	19.762284	6.00	19.762191	7.06

Table 5.4: Settings for each experimental run of EMMA four sectors, in each case the value given is that used as the setting on the EMMA control panel.

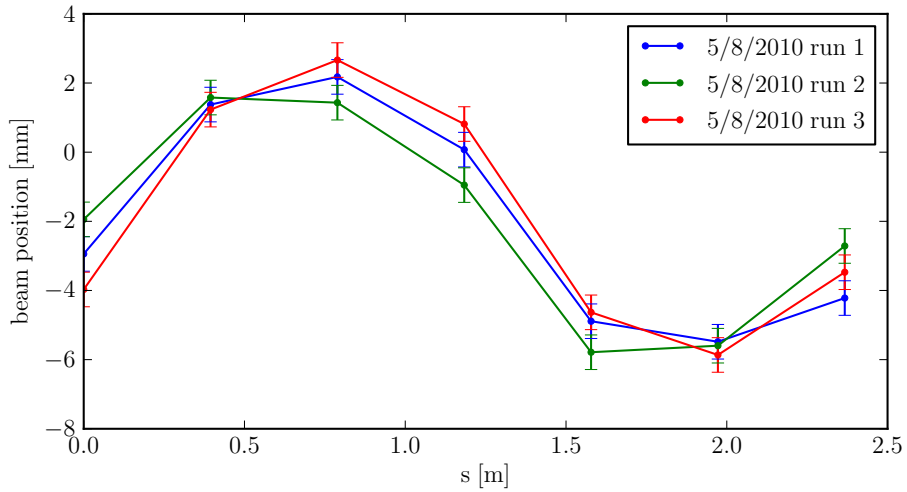

(a) $p = 1.0\,p_0$

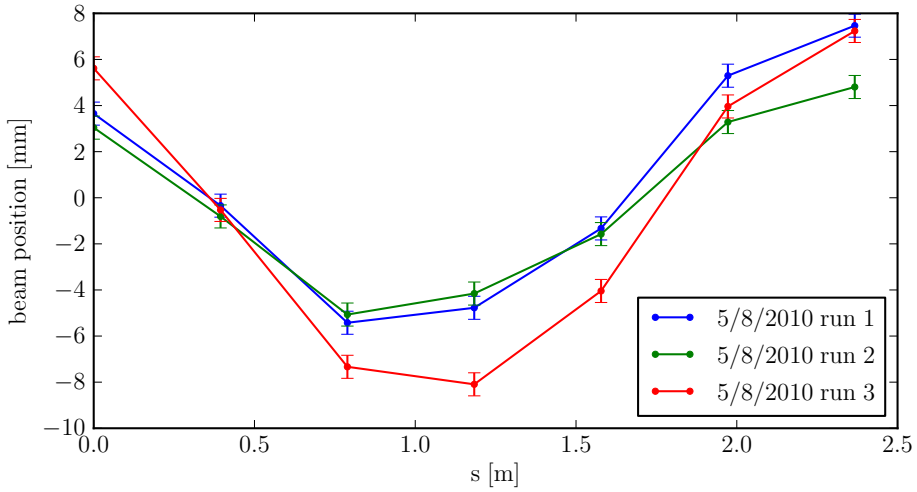

(b) $p = 1.05\,p_0$

Figure 5.8: Measurement of horizontal positions with relative momenta equal to and greater than p_0.

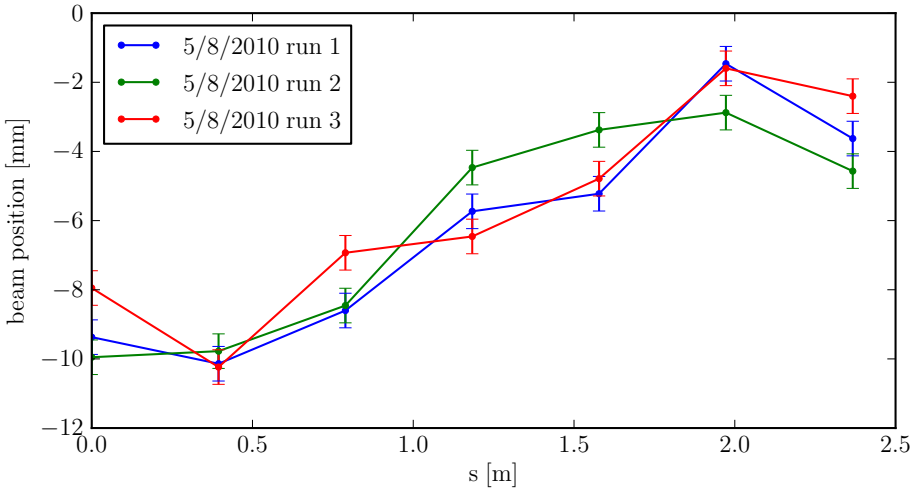

(a) $p = 0.9\,p_0$

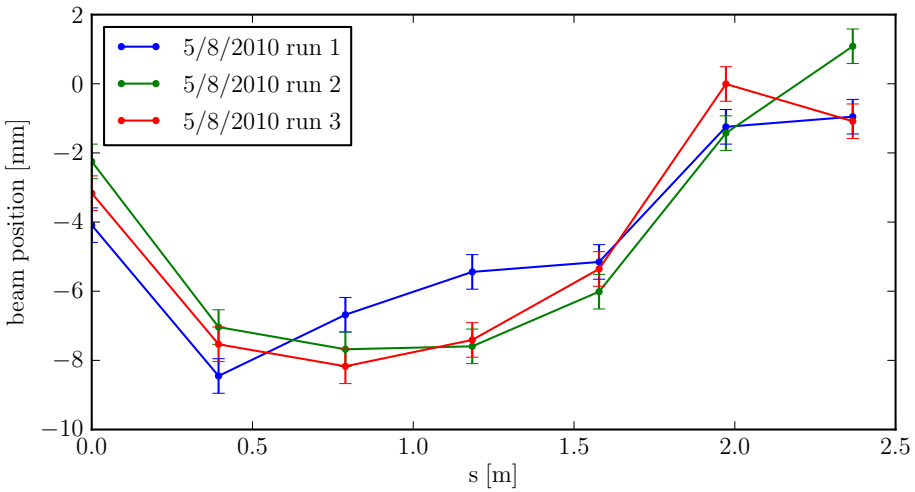

(b) $p = 0.95\,p_0$

Figure 5.9: Measurement of horizontal positions with relative momenta less than p_0.

5.4.2 Dispersion measurement

Using the position data obtained in the previous section, the centre of the orbit is approximated by taking the mean of the 7 horizontal beam position readings. The dispersion is then found by making a linear fit to the mean positions with relative momentum, as shown in Fig. 5.10. The measured mean dispersion in this momentum range is $D(p) = 42.01 \pm 12.1\,\text{mm}$, compared to $D(p) = 53.9 \pm 0.52\,\text{mm}$ obtained from the earlier simulation. The error on this measurement is calculated as the difference between the best fit and the maximum/minimum linear fits which remain within the error bars of the data points.

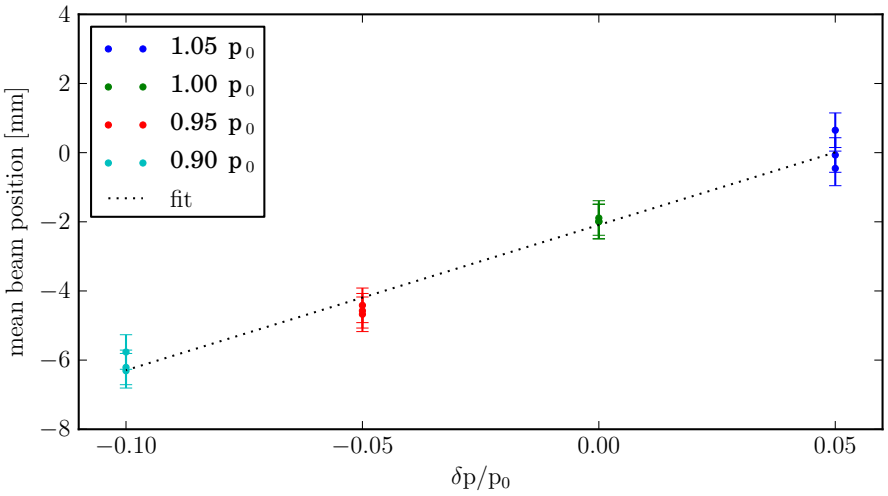

Figure 5.10: Measured dispersion in EMMA four sector setup.

5.4.3 Horizontal tune measurement

The measured horizontal cell tunes are shown with the simulated tune values in Fig. 5.11. Given the difficulty of measuring the tune in this scenario, the agreement with simulation for the two higher momenta is remarkable. However, the two lower momentum values differ significantly from the expected tunes.

During the measurements at lower momenta there appears to have been significant beam loss occurring upstream of the BPMs. Although there is no beam loss monitor to verify this hypothesis, there was a reduction in the amplitude of the raw BPM signals observed. Further information can be gained by looking at the sinusoidal fit to the BPM data points, shown in Fig. 5.12. It is clear that the sinusoidal fit to the data points in Fig. 5.12b for $p = 1.0\,p_0$ is far superior to that in Fig. 5.12a for $p = 0.9\,p_0$. Beam loss upstream of the BPMs or in the 7 cells in which these measurements were taken would result in a non-uniform and mis-shapen bunch which could give false or misleading position measurements. As the tune measurement relies on the frequency component of these position measurements, the tune measurements at lower momenta cannot be considered to be reliable.

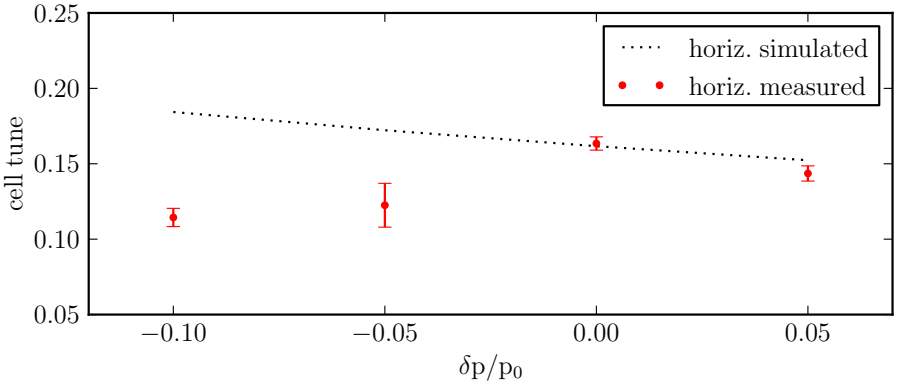

Figure 5.11: Measured horizontal cell tunes in the EMMA four sector setup.

5.5 Commissioning of the full EMMA ring

The involvement of the author in EMMA commissioning effectively ended after the four sector experiments took place. Since this time, the full ring has been completed and work has continued to progress rapidly in the commissioning of EMMA. The first beam was steered around the full ring on August 16$^{\text{th}}$ 2010 and over 1000 turns were achieved shortly after this. Fig. 5.13 shows the oscilloscope readings of BPMs

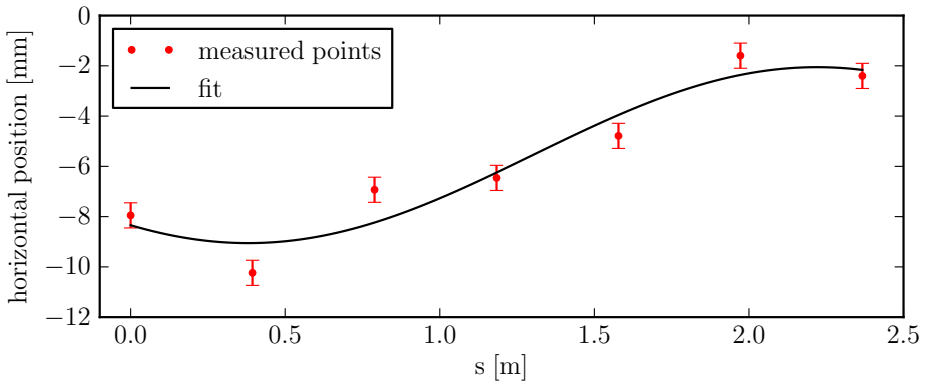

(a) $p/p_0 = 0.9$

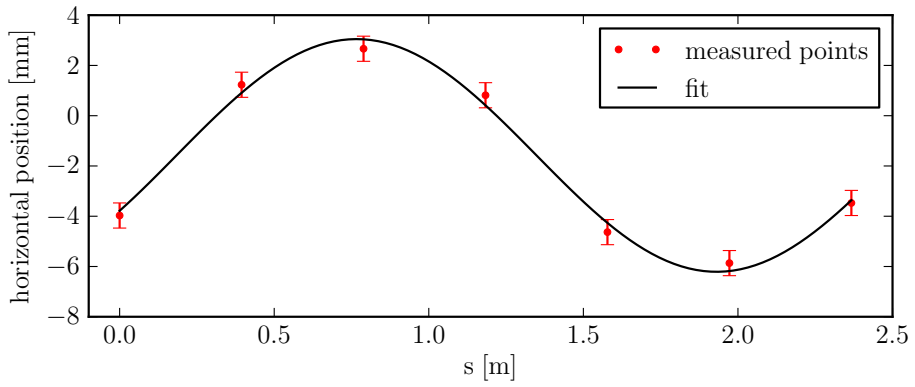

(b) $p/p_0 = 1.0$

Figure 5.12: Sinusoidal fits to measured data points for the lower momentum (a) and the reference momentum (b).

between the D and F quadrupoles in cells E12 to E15.

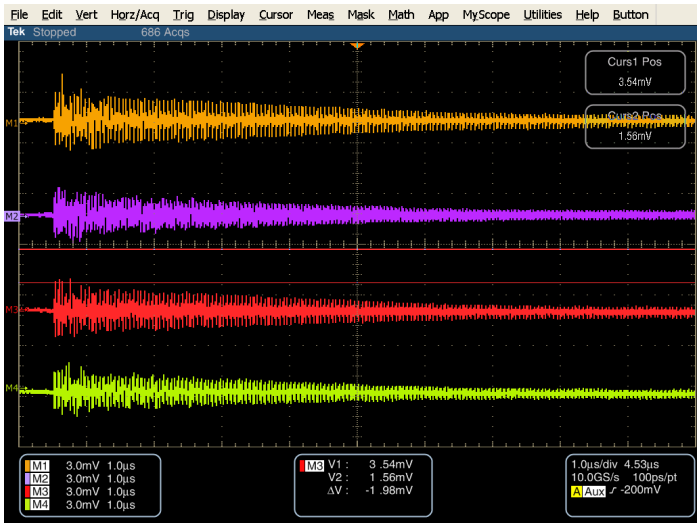

Figure 5.13: BPM traces in cells E12 (upper, orange) to E15 (lower, green) showing over 1000 turns in the EMMA ring.

On August 30th, further measurements were made of the beam position with varying momenta which are suitable for comparison with the results presented earlier in this chapter. The same central momentum of 18.5 MeV/c was used and the BPMs in cells E12 to E18 were measured, this time for two turns in the EMMA accelerator with the RF system off. The same method as before was used both for taking the measurements and to find the horizontal betatron tunes.

5.5.1 Full ring experimental results

The measured horizontal cell tunes using the full EMMA ring over two turns are shown in Fig. 5.14. The tunes measured in this case agree with the ZGOUBI simulation presented earlier and seem to resolve the ambiguity of the low momentum tunes in Fig. 5.11. A detailed comparison of codes for EMMA has been undertaken previously [112]. The predicted tunes using a second simulation code called the Polymorphic Tracking Code (PTC) [113] from the code comparison are included for reference.

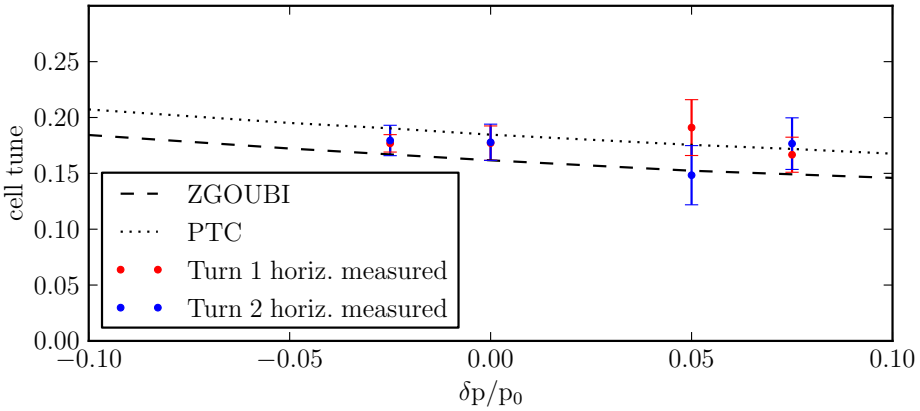

Figure 5.14: Measured horizontal cell tunes over 2 turns in EMMA.

5.6 Discussion of experimental results

The results presented here indicate that, for the most part, the simulated and experimental data for EMMA agree within error. The original low momentum tunes are considered to be unreliable, but later measurements show that the predicted and measured values are in good agreement. This work has been undertaken without the use of the electronic BPM readout system and further clarification of the tunes will be possible once this system is available. Further EMMA commissioning should also clarify the tunes as a function of momentum over the full momentum range and more precisely determine the extent of the agreement between the ZGOUBI model and the real machine.

With regards to PAMELA, this indicates that a reasonable degree of confidence can be placed in the ZGOUBI code and that in practice the results should not differ dramatically from the model.

Chapter 6

The PAMELA CPT facility

For completeness a brief discussion of the main components in the PAMELA facility is given in this chapter. Although this is not the main focus of this thesis, each of the components of the PAMELA facility needs to be studied in detail in order for the project to proceed from conceptual design to engineering design. Different members of the PAMELA collaboration have been involved in developing ideas for the various components. References to the most recent publications or conference proceedings are given for those items which are not the work of this author.

Designs for the main magnets of the two PAMELA accelerating rings are advanced, and conceptual designs exist for the low energy transport, RF cavities, injection and extraction septa and kickers and a possible FFAG gantry. It is shown that each of the components is able to integrate with the lattice designs developed in Chapters 3 and 4.

The main magnet designs are of considerable interest to this work, as they must be able to realise the multipolar fields required to obtain stable betatron tunes. The results of multi-particle tracking through detailed 3D field maps and their implications for the full engineering design and realisation of the PAMELA ns-FFAG are presented.

6.1 Design of the PAMELA facility

6.1.1 Facility layout

A 3D schematic of what the PAMELA facility might look like is in Fig. 6.1. On the left is the injection system including ion sources for both protons and carbon ions, and the two concentric accelerating rings are in the centre of the figure. The extraction lines, transport lines and treatment gantry are not shown here.

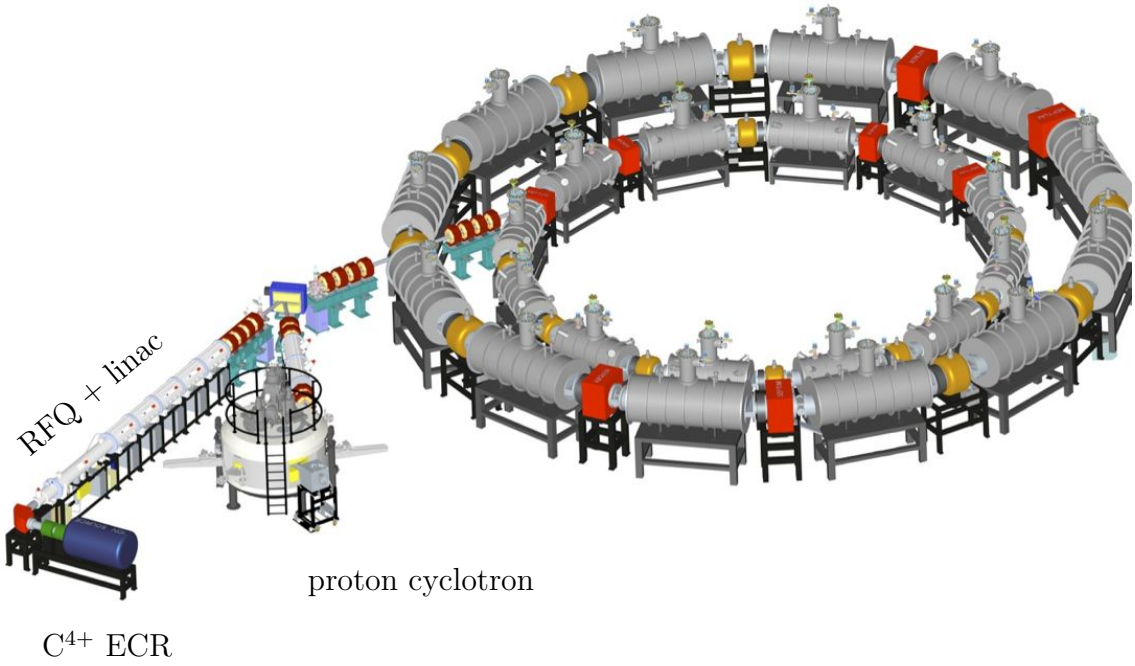

Figure 6.1: Layout of the PAMELA injection system and accelerating rings [114].

6.1.2 Ion sources and low energy transport

The injection system for PAMELA must provide both protons and C^{6+} ions with identical magnetic rigidity for injection into the proton ring. For protons, the system consists of an 'off the shelf' 30-31 MeV cyclotron such as the IBA Cylone 30 ® [115]. For carbon, the injection system is expected to consist of a C^{4+} electron cyclotron

resonance (ECR) ion source providing $8-10\,\mathrm{keV/u}$ C^{4+} beams, such as that presented in Ref. [116]. The emerging beam contains C^{4+} mixed with C^{3+} and C^{5+} so must be separated using a spectrometer dipole and aperture. This is followed by a radio frequency quadrupole (RFQ) to accelerate to $400\,\mathrm{keV/u}$ [117] and a short linac to boost to $8\,\mathrm{MeV/u}$. The linac is followed by a stripping foil to achieve fully stripped ions.

A basic layout of the system as presented in Ref. [3] is shown in Fig. 6.2. It is envisaged that to reduce the overall footprint of the accelerator complex, this could be placed inside the proton ring. The exact layout would depend on the space available in a proposed facility. The integration of this system with the accelerating rings is expected to be straightforward.

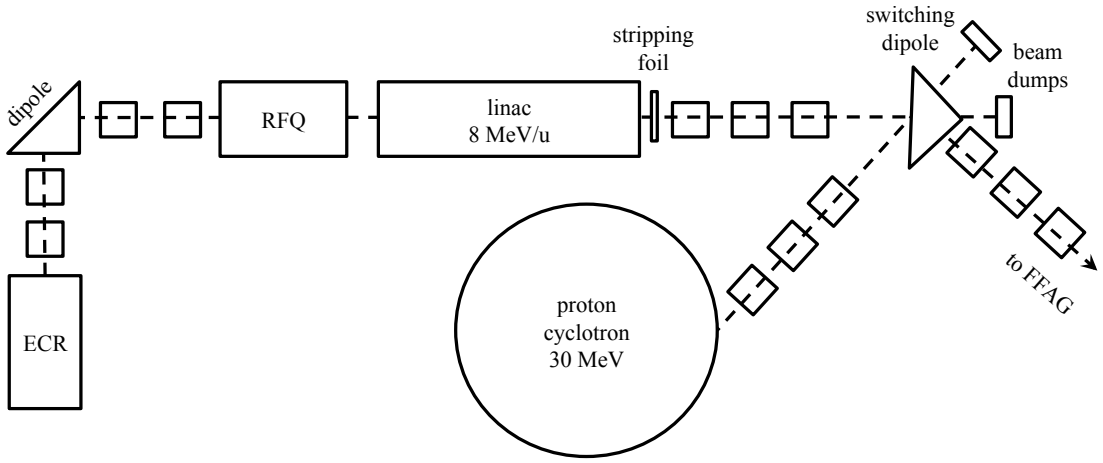

Figure 6.2: Layout of a conceptual PAMELA injection system, adapted from Ref. [3].

6.1.3 Magnets

The main lattice magnets have been developed to produce the complex multipolar field required by the lattice design. The design concept depends on the well-known cosine-theta current distribution of Eqn. 6.1 in which J_z is the current density in the direction tangential to the beam, θ is the azimuthal angle and m is the order of multipole ($m = 1$ for dipole, $m = 2$ for quadrupole, $m = 3$ for sextupole *etc...*).

$$J_z(\theta) = J_0 \cos(m\theta). \tag{6.1}$$

Theoretically it is possible to create any number of multipoles using a single coil. In this case individual multipole coils were adopted in a layered technique to ensure good flexibility in tuning the lattice. Due to the large bore-to-length ratio a 'tilted solenoid' or double helix design is used, as described originally in Ref. [118] and more recently in Ref. [119]. This is shown for a dipole coil in Fig. 6.3.

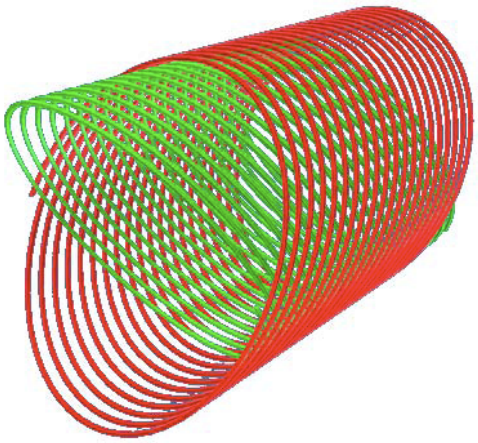

Figure 6.3: 3D image of a double helix dipole coil [3].

The coils are a superconducting air core design using standard NbTi superconducting wire, and will be placed in a warm-bore 4 K liquid helium cryostat.

Due to the complexity of the field produced by the main lattice magnets, it is important to show that it is possible to track through accurate 3D field maps of the magnet design and produce stable betatron tunes which reflect those produced by the ZGOUBI model.

A number of properties of the 3D field maps could be different from the ZGOUBI analytical model. The magnets will have a long fringe field extent due to the large air core and the exact shape and length of these fringe fields is unknown. Additionally, in the double helix magnet design the presence of small field components in the

horizontal and longitudinal directions are observed. Tracking using 3D field maps is the only way to ascertain whether or not these field components are problematic.

To produce the 3D field maps a generator written in MATLAB™ [120] was used to create 3D field maps for the proton lattice, using a simplified model of the magnet design [121]. These maps were then tracked using the TOSCA element in ZGOUBI, which makes a second order polynomial interpolation between the points of the map [75, p.115].

With single particle tracking at the proton lattice reference energy (118 MeV) it was found that the unwanted horizontal and longitudinal field components in the double helix magnet design perturb the beam and no stable closed orbit or stable tunes could be found. An approximate closed orbit was established by minimising the phase space area of single particle tracking through a small number of turns and the position of the vertical closed orbit was assumed to be $y = 0$. A single particle was then tracked until it was lost, shown in Fig. 6.4. Note that in Figs. 6.4 and 6.7 there is a change of reference frame between each cell so the trajectories appear on a straight line, this causes the apparent discontinuity at approximately $x = -0.10$ m.

The horizontal and longitudinal field components can perturb the beam in the vertical plane. This perturbation will also affect the horizontal motion due to the higher order multipole fields. The fields experienced by the particle in the above tracking example are shown in Fig. 6.5. While the horizontal (Fig. 6.5b) and longitudinal (Fig. 6.5c) fields are much lower than the vertical field (Fig. 6.5a) for the first few turns they are not negligible and appear to be the cause of the instability observed in the particle tracking.

This indicates that simple double helix coils may not be suitable for this application. To overcome this issue, the horizontal and longitudinal field components were removed by using a novel helical coil system.

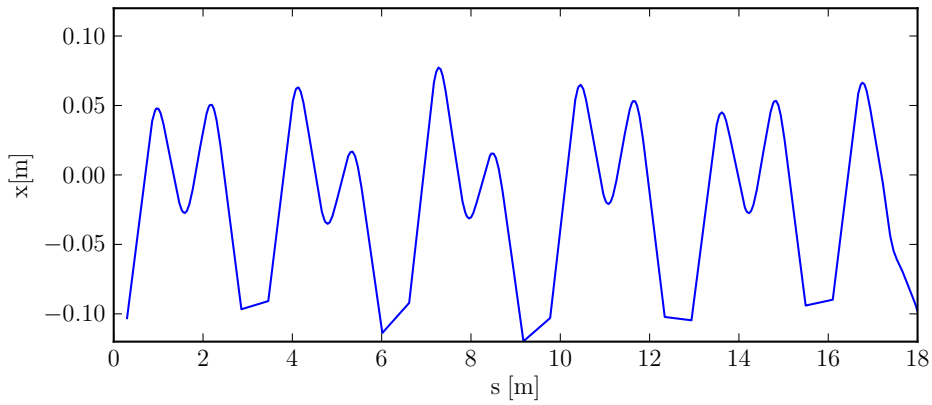

(a)

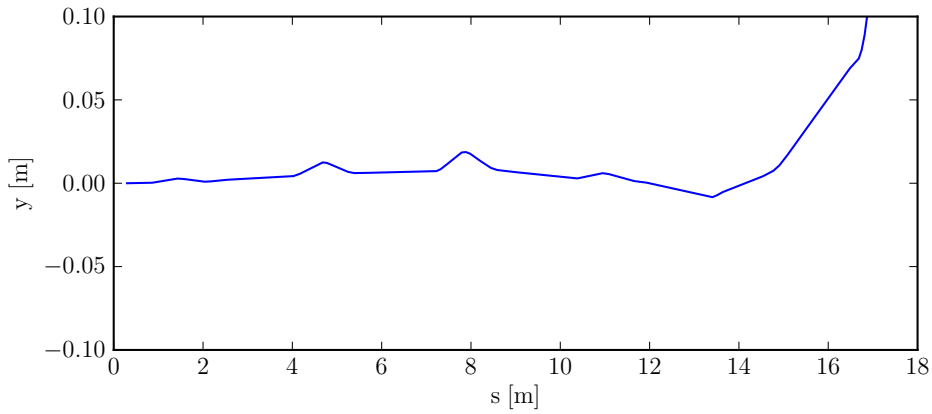

(b)

Figure 6.4: Horizontal (a) and vertical (b) motion of a single particle tracked through 3D field maps of double helix coils.

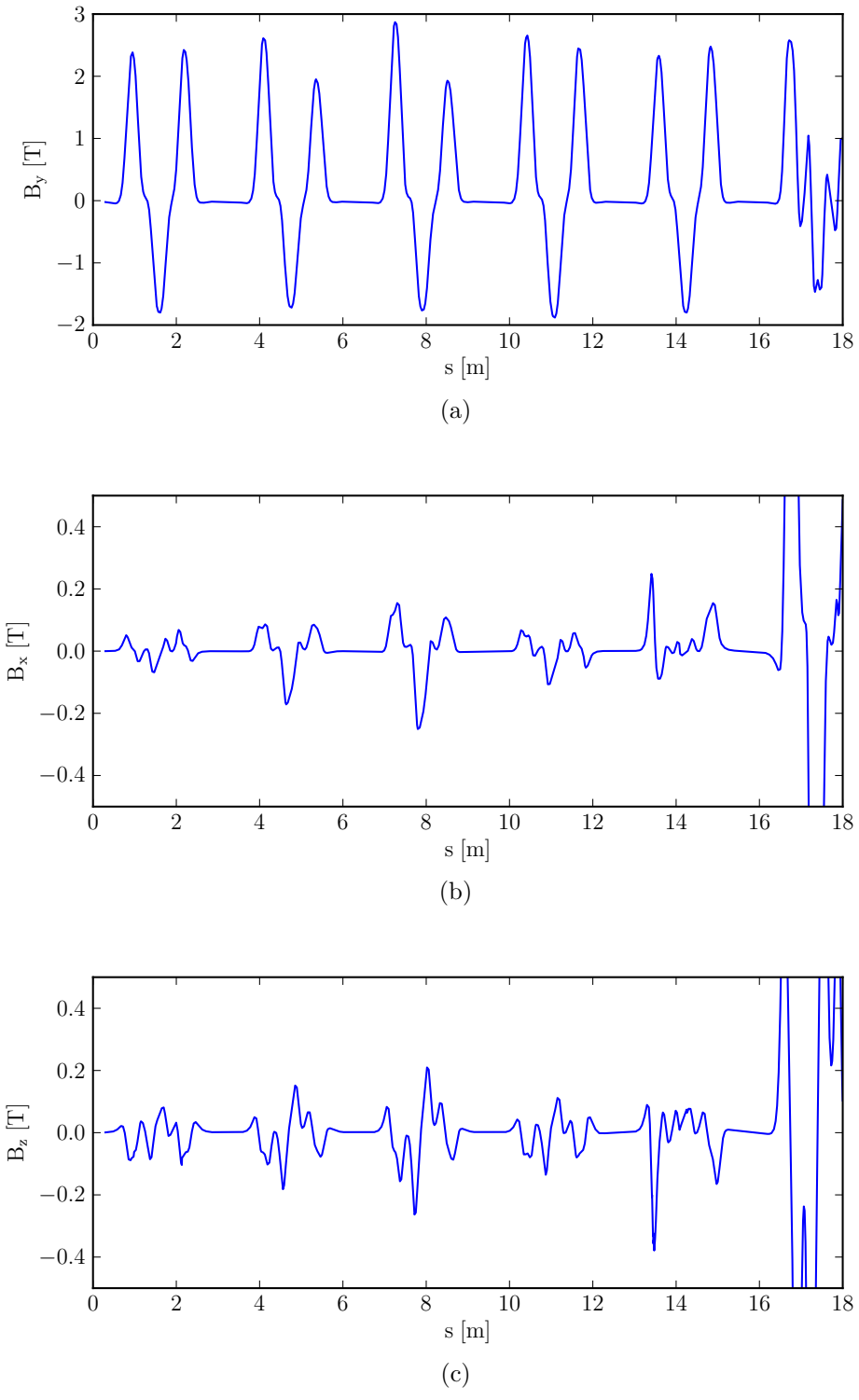

Figure 6.5: Vertical (a) magnetic field experienced by tracked particle and horizontal (b) and longitudinal (c) field components in double helix coil tracking.

Tracking through helical coil magnets

The coil system was developed to remove the horizontal and longitudinal field components and the design has been patented [122]. An example of a PAMELA proton ring coil is shown in Fig. 6.6. This design provides an extra degree of freedom which has enabled the magnet designer to cancel the unwanted field components.

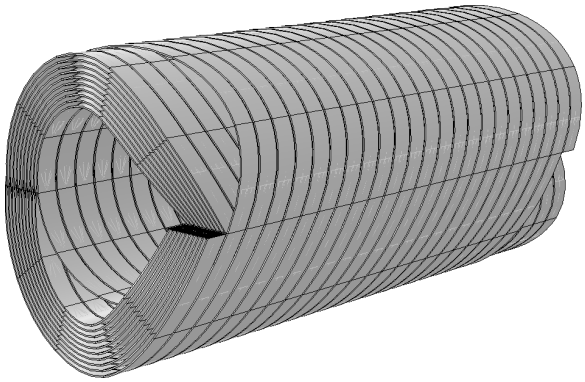

Figure 6.6: 3D image of the coil concept for the PAMELA proton ring [114].

Tracking through the coil field maps was performed using single particle tracking as before. In this case stable closed orbits and tunes were obtained, which indicates that the unwanted field components in the double helix case were indeed problematic. The horizontal motion of a single particle tracked at the reference energy of the proton ring in the 3D field maps is shown in Fig. 6.7. The vertical motion in this case is negligible.

Betatron tunes from 3D field map tracking

Initial tracking results of the 3D field maps for the proton lattice produced stable betatron tunes. However, the design produced tunes which were significantly different from those expected from the optimisation procedure and tracking studies of Chapter 3. Fig. 6.8 shows the tunes as previously given in Chapter 3 together with the initial tunes calculated from tracking of the 3D field maps. After manually changing the ratio of the individual multipole components, a solution was found which produces

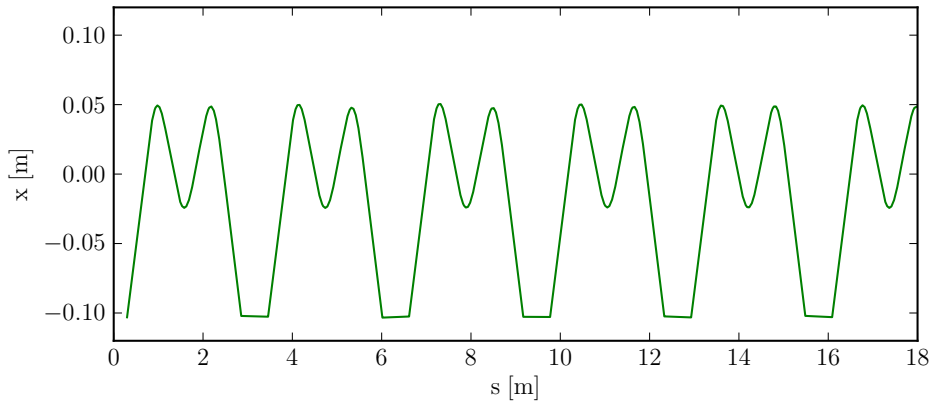

Figure 6.7: Horizontal motion of a single particle tracked through 3D coil field maps.

tunes which are stable throughout the momentum range of the machine and are constrained to within half an integer of total tune. These are shown in Fig. 6.9 [121].

The solution presented here has different tunes from the optimised design with ZGOUBI. The discrepancy between the ZGOUBI model and the 3D field maps is believed to arise from the shape of the fringe fields of the helical coils and is not well understood. This is an item of further work which should be looked at in detail. However, this shows that it is possible to achieve tunes which are constrained to within half an integer in a realistic 3D magnet design.

6.1.4 Radiofrequency (RF) cavities

The RF system for the proton ring has been developed to fit in the 1.2 m long straight sections provided in the lattice while having sufficient aperture to accommodate the orbit shift with acceleration and having the ability to maintain the very high 1 kHz repetition rate. The cavities are two-gap ferrite-loaded RF cavities, although other options including induction cavities and broadband Magnetic Alloy (MA) cavities were considered. Induction cavities were found not to be suitable as the low beam current of PAMELA means that their advantages in terms of low impedance are not utilised. MA cavities were not pursued further due to concerns over high RF power

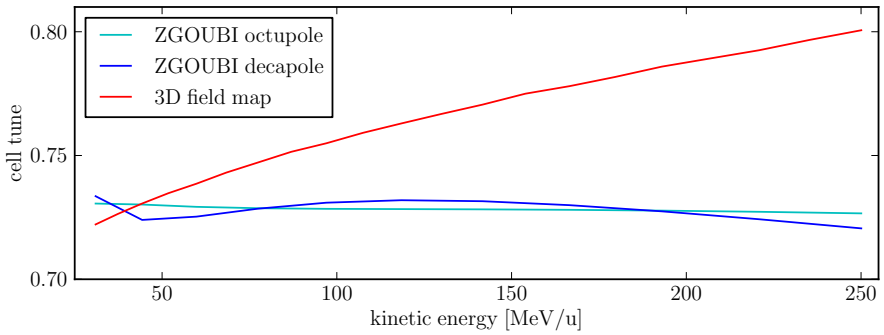

(a)

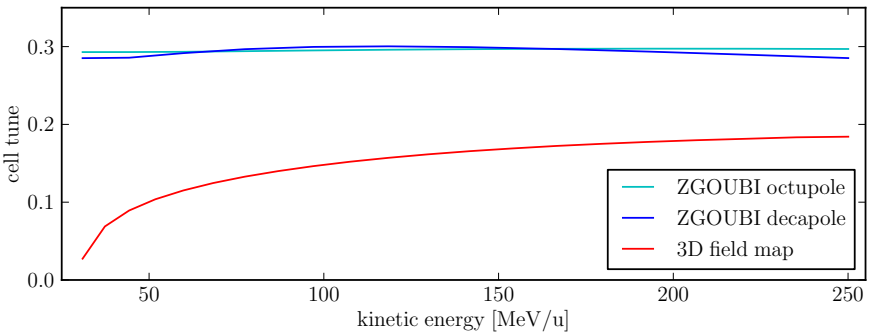

(b)

Figure 6.8: Variation of horizontal cell tune (a) and vertical cell tune (b) for the optimised proton lattice tunes in ZGOUBI compared to the initial results obtained with 3D field map tracking.

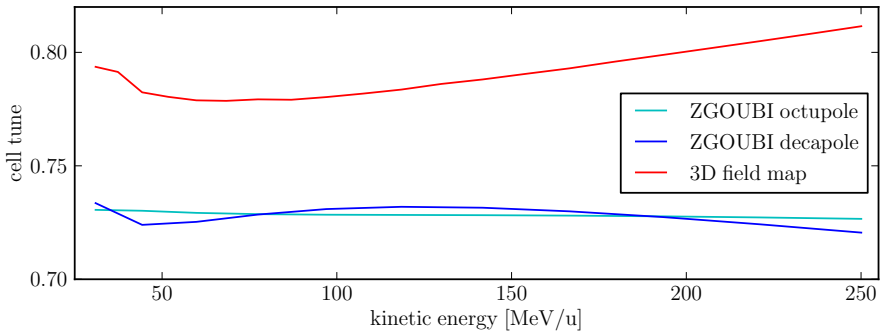

(a)

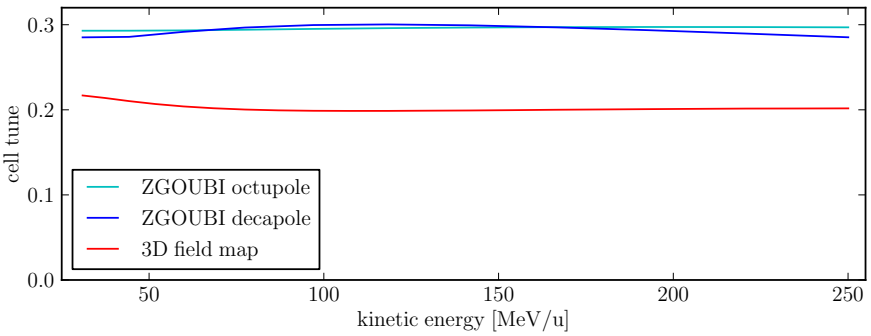

(b)

Figure 6.9: Variation of horizontal cell tune (a) and vertical cell tune (b) for the optimised proton lattice tunes in ZGOUBI compared with the new helical coil field map solution.

requirements and cooling at 1 kHz operation. These issues are discussed further in Ref. [123].

The cavities must provide an energy gain of around 100 keV/turn to achieve the 1 kHz repetition rate and there is space for a maximum of 8 cavities in the 12 cell lattice. The current design is similar to that of the ISIS second harmonic RF cavities [124] shown in Fig. 6.10. The main parameters of both the proton and carbon ring cavities are given in Table 6.1. To make sure that the ferrite rings are able to reach the required acceleration and repetition rate a small sample of the ferrite material (Ferroxcube4D2) [125] has been tested experimentally. The main purpose of these experiments was to see if the Q value of the ferrite is affected by high frequency modulation operation. At this stage, results suggest that this material should be suitable for the PAMELA RF system [126]. To date most of the work on the RF system has focused on the proton ring. The RF cavity design for the carbon ring is less advanced, but is based on the same principles.

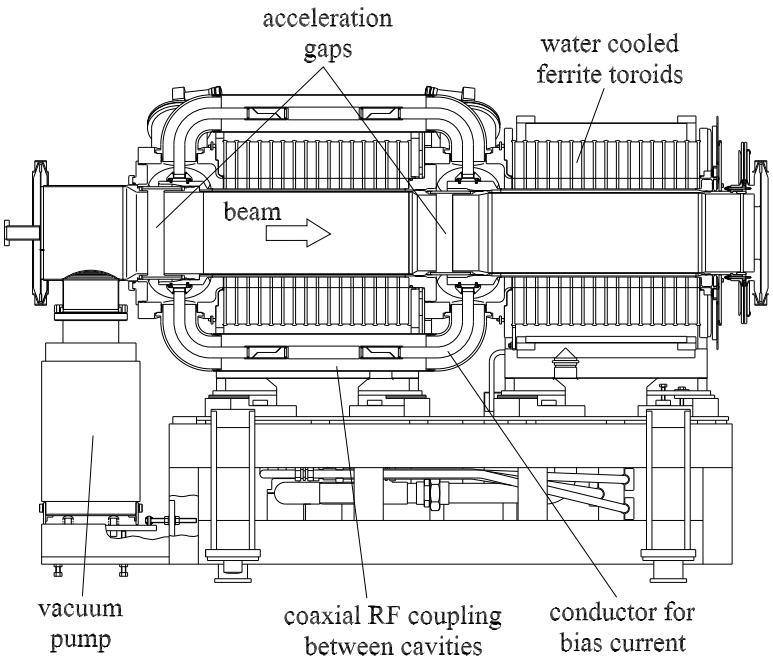

Figure 6.10: Cross-sectional side view of the ISIS second harmonic RF cavity design [127], on which the PAMELA cavities are based.

	Ring 1 $\mathbf{p^+}$	**Ring 1** $\mathbf{C^{6+}}$	**Ring 2** $\mathbf{C^{6+}}$
Harmonic	10	17	10
Low RF frequency [MHz]	19.16	16.69	19.21
High RF frequency [MHz]	45.64	45.80	39.10
Voltage per gap [kV]	6 - 15	6 - 15	6 - 15
Number of 2 gap cavities	8	8	8
Voltage per turn [kV]	96 - 240	96 - 240	96 - 240
Acceleration Time [ms]	0.44	0.44	1.72

Table 6.1: Parameters of the radio frequency system for PAMELA.

6.1.5 Injection and extraction system

The injection and extraction systems for PAMELA will be very similar to each other, with injection systems simply being scaled down by the ratio of the magnetic rigidity from injection to extraction. For each ring the injection scenario is simpler than extraction, primarily because for each ring injection occurs at a single energy. The extraction system for both rings is more difficult to design and is discussed here.

One of the key features of PAMELA is its ability to provide a variable extraction energy, however this is also one of its greatest challenges. A kicker and septum fast extraction system is envisaged, with the kicker and septum being installed in successive long straight sections within the lattice.

With an orbit excursion in the proton ring of around 18 cm and an even larger excursion in the carbon ring, the extraction kickers must have a very large aperture. To ease issues of dispersion at the septum, a vertical extraction system is planned [128]. As the variable energy proton beam would emerge from a pure dipole septum at a varying position and angle, a novel scheme where the septum has a field gradient is under development [129], which would result in extracted beams of all energies emerging with the same angle, but with a dispersion similar to that in the main ring. This could then be matched into the FFAG transport system, discussed below. The research and development into the kicker system is ongoing.

After the extraction system an achromatic dispersion matching section is planned. It is hoped that this will consist of FFAG optics [130] and thereby allow variable energy extraction and transport at the maximum repetition rate of 1 kHz.

The extraction system for the carbon ring poses an even greater challenge than that of the proton ring, by virtue of the larger magnetic rigidity. In this case, the septum must have a field of around 4 Tm to produce the required bending. A two septum approach may be needed in this case.

6.1.6 Transfer line between rings

A transfer line is required to take carbon ions at 68.36 MeV/u from the proton ring and deliver them through an optically matched line into the carbon ring. As injection and extraction from both rings is likely to be vertical, the transfer line must cancel both vertical and horizontal dispersion. The low energy C^{6+} ions from the proton ring will be extracted at an angle of approximately 30° and the transfer line will need to approach the carbon ring at an angle which is sufficiently large to avoid the edge of the magnet cryostat, which is assumed to be 30° also.

A transfer line has been designed which matches the optics of the beam (α, β) of carbon ions from the proton ring to the carbon ring. The layout of this transfer line is shown in Fig. 6.11, where the yellow magnets bend in the vertical plane, the orange dipoles bend in the horizontal plane, the red rectangles are focusing quadrupoles (in the horizontal plane) and blue are defocusing. The beta functions and dispersion in the transfer line are shown in Fig. 6.12. This design allows the proton ring to be placed within the carbon ring, without a vertical displacement between the rings[1].

The variable energy extraction system and beam transport for protons uses the same extraction septum as the carbon beam. To accommodate the FFAG optics of

[1]A vertical displacement has been discussed, as it could ease maintenance access to the inner ring. This design is able to accommodate a vertical displacement between the rings after adjusting quadrupole strengths.

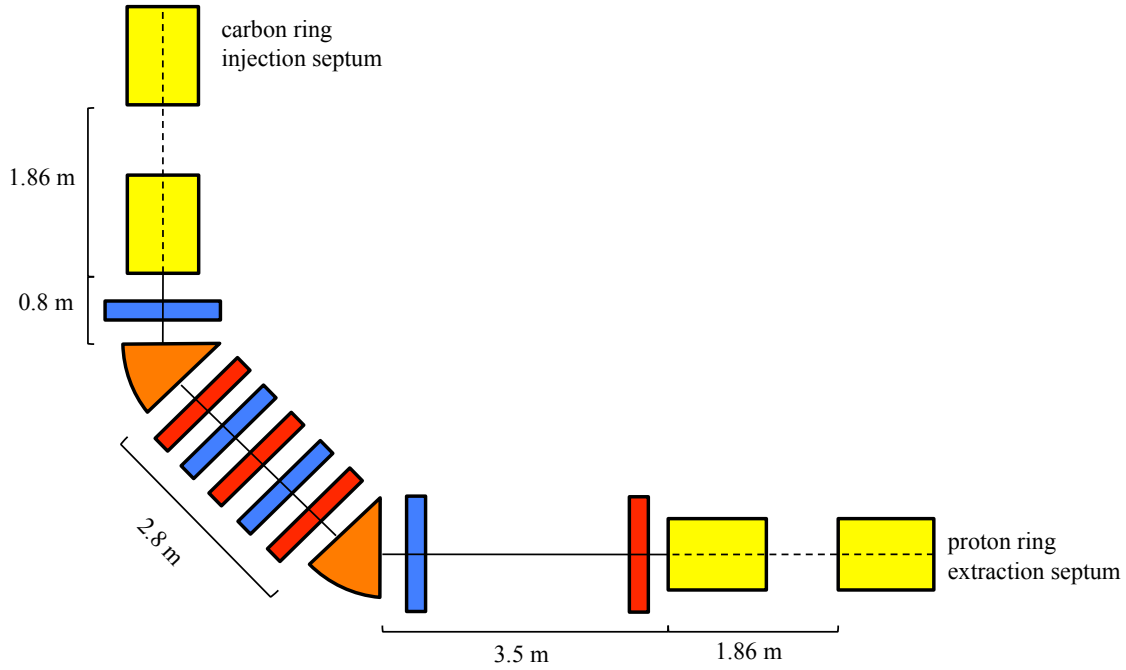

Figure 6.11: Layout of the matched transfer line for 68 MeV/c carbon ions. Vertical bends are shown with dashed lines.

the proton transport to the treatment rooms, the transfer line is designed with a long horizontal drift section soon after extraction from the proton ring. It is envisaged that the beginning of the proton transport line could be integrated into this drift space.

6.1.7 Transport line and rotating gantry

Beam transport

After extraction from either the proton or carbon ring, the particles should be transported through to the treatment rooms where they are used for treatment with either fixed horizontal or vertical beam lines or through a rotating gantry. An idealised layout of a transport line from the accelerator to the treatment rooms is shown in Fig. 6.13.

Given the 1 kHz repetition rate of the accelerator, the transport line and gantry need to be able to accept beams with rapidly varying energy so should also ideally

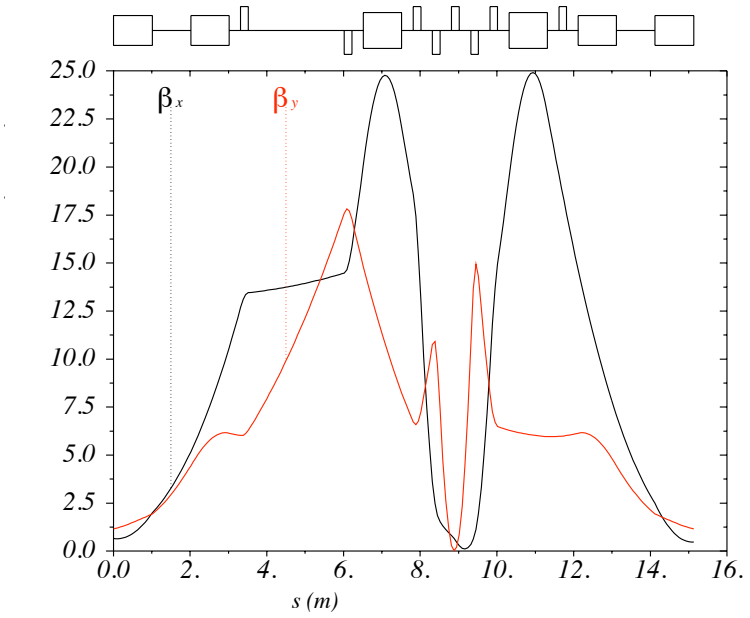

(a)

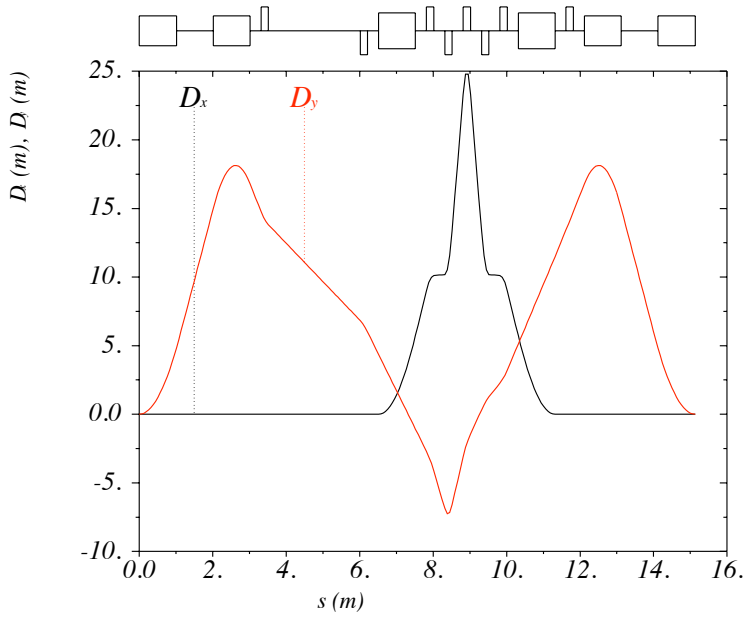

(b)

Figure 6.12: Beta functions (a) and dispersion (b) in the matched transfer line for 68 MeV/c carbon ions.

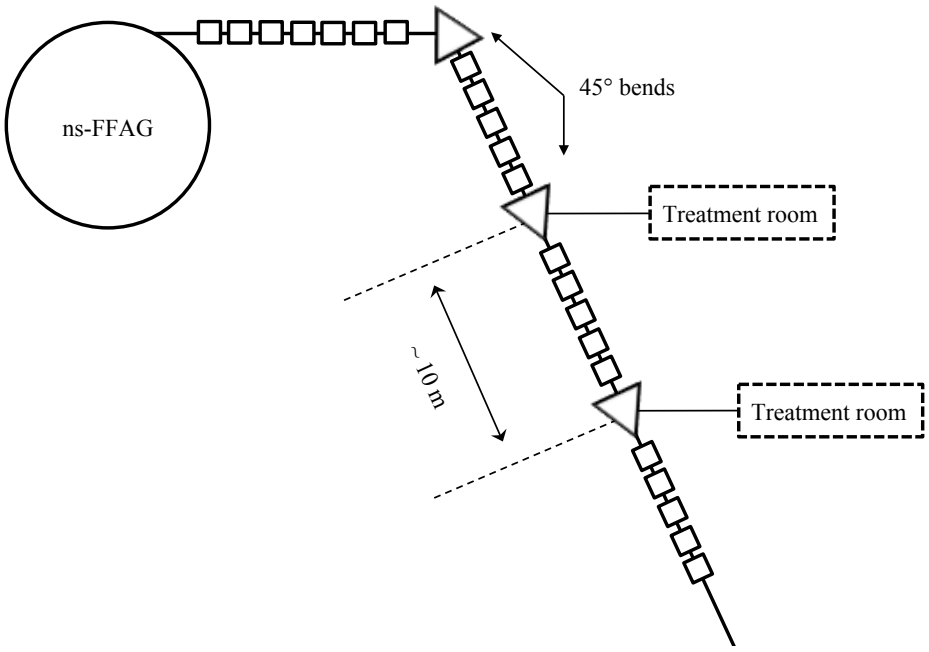

Figure 6.13: Idealised layout of the transport line from the ns-FFAG accelerator to the treatment rooms, adapted from [131].

consist of fixed field components. The limiting factor in the overall speed of energy variation will be any components which require physical movement or field variation, so these should be kept to a minimum.

The conceptual design of a transport line using scaling FFAG magnets is outlined in Ref. [132]. The transport line has an FDDF configuration such that the beam trajectory at the entrance and exit of the structure is designed to be perpendicular to the face of the magnet. This repeated cell structure is 1.6 m in length. The exact total length of transport needed between the accelerator and treatment rooms is unknown as it would be different in each facility. However, it has been shown that a 160 m long transport line using this design (100 cell lengths) has an impressively large acceptance of over $1000\,\pi$ mm mrad.

Dispersion suppressor

An FFAG accelerator or transport line naturally has a change in orbit position with momentum. To overcome this prior to a rotating gantry, a dispersion suppression

section is needed. The design of a dispersion suppressor was also outlined in Ref. [132]. The concept of an FFAG dispersion suppressor follows the same basic principles of the well known missing-dipole dispersion suppression scheme [45, p.124].

In this case, a cell is designed with a 180° phase advance with a field index that is doubled with respect to the normal cells[2]. In a straight FFAG section the horizontal orbit position x of a particle with momentum $p_0 + \delta p$ with respect to the reference orbit x_0 can be expressed as:

$$\frac{x}{x_0} = \left(\frac{p_0 + \delta p}{p_0}\right)^{1/(k+1)}. \tag{6.2}$$

As shown in Appendix B of [132], taking the leading term of the above expression, corresponding to the quadrupole component:

$$x = x_0 + \frac{1}{k/x_0}\frac{\delta p}{p_0}, \tag{6.3}$$

indicates that the dispersion is inversely proportional to k/x_0, so the dispersion function and its derivative in the dispersion suppressor cell are half that of the normal cell. This leads to the approximate cancellation of the dispersion from the normal cell, so that the dispersion D and its derivative D' are both zero after the dispersion suppressor. As the FFAG magnets have field components higher than quadrupole the dispersion suppression is not perfect, but it should be possible to constrain the particle orbits at the end of the transport line to within 0.5 mm in position and 0.025° in angle for the momentum range of the PAMELA proton lattice [133].

[2]In fact the dispersion suppressor needs a field index that is $k_2 = 2(k_1 + 1)$ where k_1 is the normal cell field index and k_2 is that of the dispersion suppressor. In this case the field index used is high enough that this is a negligible difference.

Rotating gantry

A preliminary design for the rotating gantry is described in [130]. Conceptually, it consists of sections of FDF triplet cells similar to those of the main lattice design with triplet dispersion suppressor sections similar to those outlined above. The design is divided into four sections as shown in Fig. 6.14 with four different cell designs which effectively reduce the dispersion throughout the gantry. The cell types of the four sections are outlined in Table 6.2.

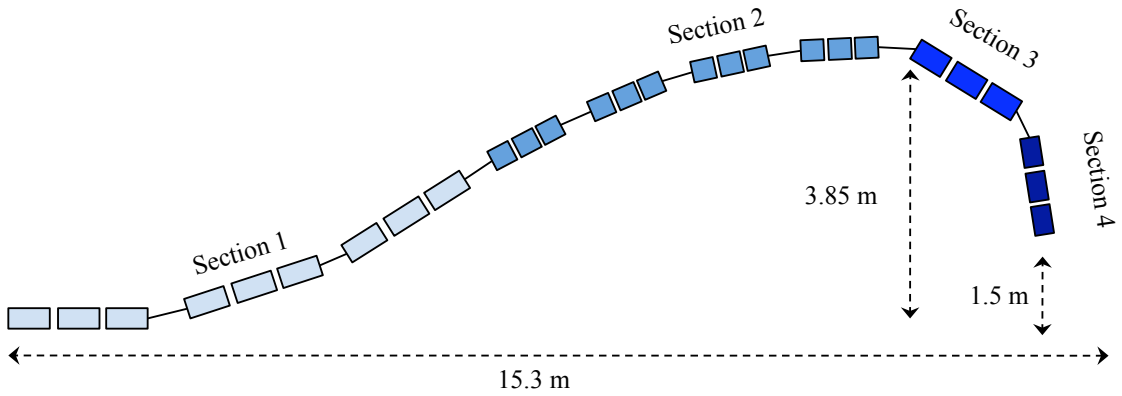

Figure 6.14: Conceptual design of the proton gantry [130].

	Section 1	**Section 2**	**Section 3**	**Section 4**
Number of cells	3	4	1	1
Bend angle [degrees]	10	7.5	60	30
Phase advance	$2\pi/3$	$\pi/2$	n/a	π
Field index, k	2.23	3.69/7.38	3.69	5.72
Magnet length [cm]	66.66	37.5	45	45
Maximum aperture [cm]	29.3	20.75	32.59	22.08
Field at maximum aperture [T]	0.928	-2.149	3.878	3.157

Table 6.2: Parameters of the preliminary rotating proton gantry for PAMELA.

Work on the proton gantry design is ongoing and may change in the future in order to integrate the scanning system. At this stage no design exists for the carbon gantry.

6.1.8 Summary of the PAMELA facility design

The ideas outlined in this chapter show that it is possible to convert the lattice designs presented in this thesis into realistic accelerator components. The majority of the proton lattice components have been designed in some detail, while the carbon ring designs are more challenging and work is ongoing for these components. Many of the designs are advancing rapidly and a full design review of the facility is planned during October 2010.

Chapter 7

Summary and further work

7.1 Summary

This thesis has described the development of a novel non-linear ns-FFAG for charged particle therapy from the lattice design through to the individual accelerator components.

Initial work on an existing ns-FFAG lattice design, the KST lattice, showed that a densely-packed linear ns-FFAG is not suitable for this application, as it is not possible to accelerate quickly enough to overcome the detrimental effects of betatron resonance crossing. The amplification factor for orbit distortion was found to be 336 ± 104 in the horizontal plane and 293 ± 136 in the vertical plane. To accelerate protons from 30.95 to 250 MeV in 1000 turns this would require the components to be aligned to better than $3\,\mu$m, an unrealistic alignment accuracy.

In terms of lattice design, the most plausible solution to overcome this issue was the addition of higher-order magnetic multipoles to reduce the total tune excursion to within half an integer and avoid the resonance crossing problem entirely. This idea led to the development of the novel non-linear ns-FFAG which has formed the major part of this thesis. Two accelerating rings have been designed, one for protons to

250 MeV (and low energy C^{6+} to 68.36 MeV/u) and the other to further accelerate C^{6+} to 400-430 MeV/u.

The first lattice to be developed was for the proton ring. The lattice design concept started from a scaling FFAG with triplet focusing. The design uses the second stability region of Hill's equation and has a number of key differences from a scaling FFAG which make it non-scaling. The changes simplify the engineering design and ease the alignment of the accelerator components, while avoiding resonance crossing and retaining the small orbit excursion characteristic of ns-FFAGs. The resulting lattice design is completely new, as is the design strategy, which can be used to apply this novel concept to accelerators of a wide range of energies.

Detailed studies of this design were undertaken which showed that an alignment accuracy of 50 μm will not have a detrimental effect on the beam. The dynamic aperture for most lattice configurations was found to be greater than 50 π mm mrad normalised in both the horizontal and vertical plane and tracking of a 10 π mm mrad normalised emittance beam showed that the lattice is able to tolerate realistic alignment errors.

The second accelerating ring presented more of a challenge in terms of lattice design. A basic parameter scan showed that only a small range of ring radii, lattice packing factors and field index values could meet the lattice requirements. The optimised solution using the design strategy is for a ring radius of 9.3 m. This is larger than desired as it is comparable with synchrotrons of a similar energy. It does not seem possible to reduce the size of this ring as the lattice design incorporates reverse bending in the FDF triplet configuration. However, the ring is no larger than existing carbon synchrotrons.

The ability to provide fully stripped carbon ions at a repetition rate of up to 1 kHz is unmatchable with synchrotrons and allows for greater flexibility in treatment planning, as it allows for rapid variation in the transverse and longitudinal

planes simultaneously. However, the carbon ring presents a greater challenge in its engineering design than the proton ring; work on this is ongoing within the PAMELA collaboration.

The ZGOUBI simulation code was instrumental in the design of both PAMELA and EMMA. A proposal to commission four out of seven sectors of the EMMA accelerator was adopted by the collaboration and allowed some initial measurements of the betatron tune and dispersion in a small momentum range to be made. While faced with experimental challenges due to the lack of electronic BPM instrumentation and limited beam time, the results from these experiments are encouraging. In the cases where significant beam loss was not an issue, the measured betatron tunes and dispersion matched the simulated results within error. Further work in verification of ZGOUBI using EMMA should be undertaken in the future to clarify this issue.

Finally, it was shown that the lattice design can be translated into realistic concepts for the individual components of the PAMELA facility, though many of the components require further development. Tracking of detailed 3D field maps of the magnet design indicated that a magnet solution can be found which recreates the lattice dynamics and avoids resonance crossing. This will need to be further understood and refined if the design is to progress to construction.

7.2 Further work

While many of the PAMELA components are well advanced, others need significant work in order to integrate them with the rest of the system. Notably, the designs for the carbon ring RF system, extraction kicker and septum are undergoing rapid development. At this stage, the transport line and proton gantry are preliminary and further work in the scanning system prior to the patient may necessitate changes to these designs. The carbon gantry also requires a large amount of work to develop the

ideas of the proton gantry into a realistic solution for carbon ions.

Further effort is required in the detailed tracking of 3D field maps for both the proton and carbon ring designs. In particular, an understanding of how the PAMELA helical coils can produce the prescribed magnetic fields accurately and thereby reproduce the expected lattice dynamics is required.

Finally, once all the PAMELA components have been designed (at least conceptually), full 6D tracking from injection to extraction and a simulation of the beam from the ion source to tumour target volume should be undertaken.

Appendix A

High level software development

During the EMMA four sector commissioning period a basic resonance crossing experiment was planned in order to compare the real orbit distortion with that predicted by ZGOUBI. Unfortunately due to lack of availability of both the BPM system and RF system, this experiment could not be performed. However, a number of pieces of high level software were developed which are applicable to a wide variety of tasks on EMMA and will help to make both commissioning and operation of the full machine simpler and quicker. This software is specific to FFAGs as it must accommodate a closed orbit which is both unknown and changes with energy. For this reason it would be very useful in commissioning a machine like PAMELA, which has a larger orbit excursion than EMMA.

The main development was a method for scanning the aperture and determining from this the centroid of the betatron oscillations or 'closed orbit'. An element of the aperture scanning algorithm was a method for measurement of the position in phase space, discussed first. Both pieces of software are written in Python and interface to the real machine using the Experimental Physics and Industrial Control System (EPICS)[134].

A.1 Phase space measurement

To measure a position in phase space, two BPMs with a known drift space between them are required. There must be no magnetic field present in this drift space so the particles pass between the two BPMs in a straight line. If the position at the first BPM is $[x_1, y_1]$ and at the second BPM a distance d downstream is $[x_2, y_2]$ then the phase space angles denoted by $[x', y']$ at the first BPM can simply be calculated as in Eqn. A.1.

$$x' = \tan^{-1}\left[\frac{x_2 - x_1}{d}\right] \tag{A.1}$$

where the equation for y' takes the same form.

This was used in the four sector setup for cells in which 2 BPMs were present at the start and end of the long drift space. A graphical user interface was developed to plot this easily in real time, as in Fig. A.1.

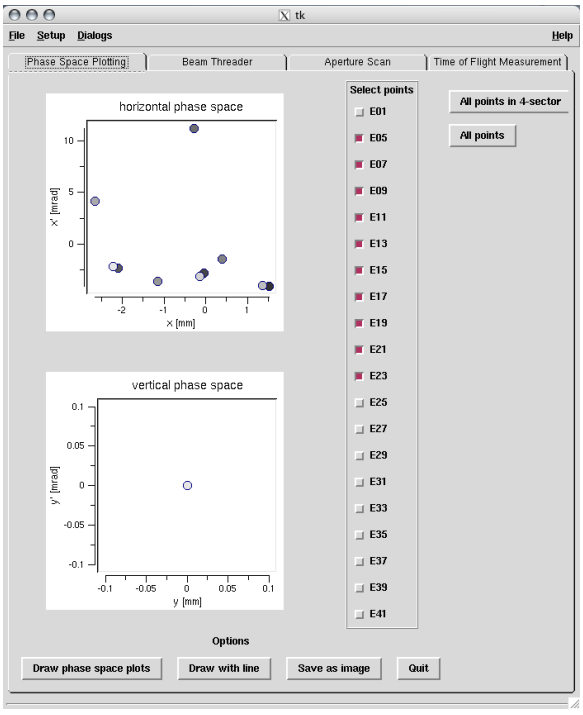

Figure A.1: Phase space software interface.

The method developed for this piece of software was used throughout the four sector commissioning period to assist in mapping the transport of the beam through the end of the injection line and in the first few cells of EMMA. The method was used without the EPICS connection during this period as the BPM system was not connected, as discussed previously.

A.2 Aperture scan

The aim of the aperture scan is to establish the injection settings of the accelerator which result in the beam being transported either to the end of a section (such as the EMMA four sectors) or through a certain number of turns in a circular accelerator. It should also plot BPM data in phase space and be able to establish a closed orbit by minimising the area of oscillations in the phase space[1].

The steps of the aperture scan are as follows:

- Set up the scan by selecting which magnets to vary and the range of variation for the scan. The type of scan (single or multi-turn) can also be selected along with which BPMs to record data from.

- Run scan and record values of beam position at chosen BPMs together with magnet settings which result in the successful transport of the beam.

- Calculate phase space positions of the beam by using phase space plotting method in cells where 2 BPMs exist in a drift section. The phase space can then be plotted for each successful transport setting. The area and centre of the phase space can then be calculated and used to identify optimal injection settings.

[1] In the EMMA four sector resonance crossing experiment this procedure would also be able to establish an approximate 'closed orbit' around which the particles oscillate. Knowledge of this orbit would allow a rough measurement of orbit distortion.

The method can be repeated with a finer range to minimise the phase space area and determine injection settings which bring the beam as close as possible to the 'closed orbit'. The graphical user interface of the aperture scan software is shown in Fig. A.2. This software will be tested when the EMMA electronic BPM cards are on-line.

Figure A.2: Aperture scanning software interface.

References

[1] K. Peach *et al.*, "PAMELA - A model for an FFAG based hadron therapy machine," in *Proceedings of the Particle Accelerator Conference*, (Albuquerque, USA), p. 2880, 2007.

[2] K. Peach *et al.*, "PAMELA Overview: Design Goals and Principles," in *Proceedings of the Particle Accelerator Conference*, (Vancouver, Canada), 2009.

[3] K. Peach *et al.*, "Preliminary PAMELA design review." Internal BASROC/CONFORM document, 2009.

[4] W. Maciszewski and W. Scharf *Eksploatacja i Niezawodnosc*, vol. 4, no. 4, 2003.

[5] W. H. Scharf and O. A. Chomicki, "Medical accelerators in radiotherapy: past, present and future," *Physica Medica*, vol. 12, no. 4, pp. 199–226, 1996.

[6] C. M. Washington and D. T. Leaver, eds., *Introduction to Radiation Therapy*, vol. 1. Mosby-Year Book Inc., 1996.

[7] U. Amaldi, "Nuclear physics applications in diagnostics and cancer therapy," *Nuclear Physics A*, vol. 751, pp. 409c–428c, 2005.

[8] B. W. Stewart and P. Kleihues (editors), "World Cancer Report, International Agency for Research on Cancer," 2003.

[9] NHS Foundation Trust. `http://www.ccotrust.nhs.uk`, August 2009.

[10] Cancer UK. http://info.cancerresearchuk.org/cancerstats/keyfacts, August 2009.

[11] W. C. Röntgen, "On a new kind of rays," *Nature*, vol. 53, no. 1396, pp. 274–275, 1896.

[12] F. M. Kahn, *The Physics of Radiation Therapy*. Williams & Wilkins, second ed., 1994.

[13] S. Webb, *The Physics of Three-Dimensional Radiation Therapy*. IoP Publishing, 1993.

[14] R. R. Wilson, "Radiological use of fast protons," *Radiology*, vol. 47, pp. 487–491, 1946.

[15] R. B. Bonnet *et al.*, "Effects of proton and combined proton/photon beam radiation on pulmonary function in patients with resectable but medically inoperable non-small cell lung cancer," *Chest*, vol. 120, pp. 1803–1810, 2001.

[16] T. DeLaney and H. Kooy, *Proton and Charged Particle Radiotherapy*. Lippincott Williams & Wilkins, 2008.

[17] C. Greco and S. Wolden, "Current status of radiotherapy with proton and light ion beams," *Cancer*, vol. 109, April 2007.

[18] M. Aoki, Y. Furusawa, and T. Yamada, "LET dependency of heavy-ion induced apoptosis in V79 cells," *J. Radiat. Res.*, vol. 41, pp. 163–175, 2000.

[19] M. Belli, A. Campa, and I. Ermolli, "A semi-empirical approach to the evaluation of the relative biological effectiveness of therapeutic proton beams: the methodological framework," *Radiation Research*, vol. 148, pp. 592–598, 1997.

[20] W. K. Weyrather, S. Ritter, M. Scholz, and G. Kraft, "Rbe for carbon track-segment irradiation in cell lines of differing repair capacity," *Int. J. Radiat. Biol.*, vol. 75, no. 11, pp. 1357–1364, 1999.

[21] IBA, "IBA Proton Therapy." `http://www.iba-protontherapy.com`, 2009.

[22] Paul Scherrer Institiute. `http://www.psi.ch/psi-home`, December 2009.

[23] D. J. Brenner and E. J. Hall, "Secondary neutrons in clinical proton radiotherapy: A charged issue," *Radiotherapy and Oncology*, vol. 86, p. 165, February 2008.

[24] D. J. Brenner, C. D. Elliston, E. J. Hall, and H. Paganetti, "Reduction of the secondary neutron dose in passively scattered proton radiotherapy, using an optimized pre-collimator/collimator," *Phys. Med. Biol.*, vol. 54, pp. 6065–6078, 2009.

[25] A. J. Lomax, T. Böhringer, A. Bolsi, *et al.*, "Treatment planning and verification of proton therapy using spot scanning: Initial experiences," *Medical Physics*, vol. 31, no. 11, pp. 3150–3157, 2004.

[26] A. J. Lomax, E. Pedroni, H. Rutz, and G. Goitein, "The clinical potential of intensity modulated proton therapy," *Z Med Phys.*, vol. 14, no. 3, p. 147, 2004.

[27] H. Tsujii *et al.* `http://ptcog.web.psi.ch`, August 2009.

[28] International Commission on Radiation Units and Measurements, "Photon, electron, proton and neutron interaction data for body tissues." Report 46, October 2007.

[29] U. Amaldi, "Cyclinacs: Novel fast-cycling accelerators for hadrontherapy," in *Cyclotrons and Their Applications*, 2007.

[30] U. Amaldi, S. Braccini, *et al.*, "Cyclinacs: Fast-cycling accelerators for hadrontherapy." `http://arxiv.org/pdf/0902.3533`, 2009.

[31] E. O. Lawrence and N. E. Edlefsen, "The production of high speed protons without the use of high voltages," *Science*, vol. 72, pp. 376–7, 1930.

[32] E. Lawrence, "Method and apparatus for the acceleration of ions." U.S. Patent 1948384, 1934.

[33] A. W. Chao and M. Tigner, eds., *Handbook of Accelerator Physics and Engineering*. World Scientific, 3 ed., 2006.

[34] H. Willax, "Proposal for a 500 MeV isochronous cyclotron with ring magnet," in *Proceedings of the International Conference on Sector-focused Cyclotrons and Meson Factories*, vol. CERN 63-19, pp. 386–97, 1963.

[35] D. W. Kerst, K. M. Terwilliger, K. R. Symon, and L. W. Jones, "Fixed field alternating gradient accelerator with spirally ridged poles," *Phys. Rev.*, vol. 98, p. 1153, 1955.

[36] D. P. Vasilevskaya *et al.*, "Start-up of a cyclotron with a spatially varying magnetic field," *Atomic Energy*, vol. 6, no. 6, p. 486, 1959.

[37] G. A. Karamysheva and S. A. Kostromin, "Beam dynamics study in the c235 cyclotron for proton therapy," *Physics of Particles and Nuclei Letters*, vol. 6, no. 1, pp. 84–90, 2009.

[38] Y. Jongen *et al.*, "Current status of the IBA C400 cyclotron project for hadron therapy," in *Proceedings of the European Particle Accelerator Conference*, (Genoa, Italy), pp. 1806–1808, 2008.

[39] M. O. Oliphant, "The acceleration of particles to very high energies." Classified memo submitted to DSIR (1943) now in University of Birmingham Archive, September 1943.

[40] V. Veksler, "Concerning some new methods of acceleration of relativistic particles," *Phys. Rev.*, vol. 69, p. 244, Mar 1946.

[41] E. M. McMillan, "The synchrotron - a proposed high energy particle accelerator," *Phys. Rev.*, vol. 68, pp. 143–144, Sep 1945.

[42] E. M. McMillan, "The origin of the synchrotron," *Phys. Rev.*, vol. 69, p. 534, May 1946.

[43] E. D. Courant, M. S. Livingston, and H. S. Snyder, "The strong-focusing synchrotron - a new high energy accelerator," *Phys. Rev.*, vol. 88, no. 5, p. 1190, 1952.

[44] E. D. Courant and H. S. Snyder, "Theory of the alternating-gradient synchrotron," *Annals of Physics*, vol. 3, no. 1, pp. 1–48, 1958.

[45] S. Y. Lee, *Accelerator Physics*. World Scientific, 1999.

[46] E. Wilson, *An Introduction to Particle Accelerators*. Oxford University Press, 2001.

[47] H. Wiedemann, *Particle accelerator physics*. Springer, 3 ed., 2007.

[48] Accelerator Complex Study Group, "Proton-ion medical machine study." CERN/PS 1999-010, 2000-007, 2000.

[49] Hitachi, "Hitachi website." `http://www.pi.hitachi.co.jp/rd-eng`, April 2010.

[50] F. Noda *et al.*, "Conceptual design of carbon/proton synchrotron for particle beam therapy," in *Proceedings of the Particle Accelerator Conference*, (Vancouver, Canada), 2009.

[51] H. Rohdjeß *et al.*, "Status of the Siemens particle therapy accelerators," in *Proceedings of the Particle Accelerator Conference*, (Vancouver, Canada), 2009.

[52] D. Ondreka and U. Weinrich, "The Heidelberg Ion Therapy (HIT) accelerator coming into operation," in *Proceedings of the European Particle Accelerator Conference*, (Genoa, Italy), pp. 979–981, 2008.

[53] G. Kraft *et al.*, "The heavy ion therapy project at GSI," *Int. J. Radiation Applications and Instrumentation. Part D. Nuclear Tracks and Radiation Measurements*, vol. 19, no. 1-4, pp. 911–914, 1991.

[54] U. Amaldi, "The Italian hadrontherapy project CNAO," *Physica Medica*, vol. 27, no. Supplement 1, p. 33, 2001.

[55] E. Griesmayer, T. Schreiner, and M. Pavlovic, "The MedAustron project," *Nuclear Instruments and Methods in Physics Research B*, vol. 258, pp. 134–138, 2007.

[56] A. Kolomensky and A. N. Lebedev, *Theory of cyclic accelerators*. Amsterdam: North-Holland Pub. Co., 1966.

[57] T. Ohkawa in *Proceedings of the annual meeting of JPS*, 1953.

[58] K. R. Symon, D. W. Kerst, L. W. Jones, L. J. Laslett, and K. M. Terwilliger, "Fixed-field alternating-gradient particle accelerators," *Phys. Rev.*, vol. 103, pp. 1837–1859, Sep 1956.

[59] A. A. Kolomensky, "Accelerators with similar orbits," *ZhETF*, vol. 33298, pp. 1371–8, 1957.

[60] D. W. Kerst, H. J. Hausman, R. O. Haxby, L. J. Laslett, F. E. Mills, T. Ohkawa, F. L. Peterson, A. M. Sessler, J. N. Snyder, and W. A. Wallenmeyer, "Operation of a spiral sector fixed field alternating gradient accelerator," *Review of Scientific Instruments*, vol. 28, no. 11, pp. 970–971, 1957.

[61] F. T. Cole, R. O. Haxby, L. W. Jones, C. H. Pruett, and K. M. Terwilliger, "Electron model fixed field alternating gradient accelerator," *Review of Scientific Instruments*, vol. 28, no. 6, pp. 403–420, 1957.

[62] Y. Mori, "FFAG proton driver for muon source," *Nuclear Instruments and Methods in Physics Research Section A: Accelerators, Spectrometers, Detectors and Associated Equipment*, vol. 451, no. 1, pp. 300 – 303, 2000.

[63] S. Machida and D. J. Kelliher, "Orbit and optics distortion in fixed field alternating gradient muon accelerators," *Phys. Rev. ST Accel. Beams*, vol. 10, p. 114001, Nov 2007.

[64] M. Aiba, K. Koba, S. Machida, Y. Mori, R. Muramatsu, C. Ohmori, I. Sakai, Y. Sato, A. Takagi, R. Ueno, T. Yokoi, M. Yoshimoto, and Y. Yuasa, "Development of a FFAG proton synchrotron," in *Proceedings of the European Particle Accelerator Conference*, (Vienna, Austria), pp. 581–583, 2000.

[65] M. Yoshimoto, T. Adachi, *et al.*, "Recent beam studies of the POP FFAG proton synchrotron," in *Proceedings of the Particle Accelerator Conference*, (Chicago, USA), p. 51, 2001.

[66] T. Adachi, M. Aiba, *et al.*, "A 150 MeV FFAG synchrotron with return-yoke free magnet," in *Proceedings of Particle Accelerator Conference*, (Chicago, USA), p. 3254, 2001.

[67] K. Okabe, Y. Mori, and M. Muto, "An intense neutron source with emittance recovery internal target (ERIT) using ionisation cooling," in *Proceedings of the European Particle Accelerator Conference*, (Genoa, Italy), pp. 3512–3514, 2008.

[68] M. Tanigaki, K. Mishimi, *et al.*, "Construction of FFAG accelerators in KURRI for ADS study," in *Proceedings of the European Particle Accelerator Conference*, (Lucerne, Switzerland), p. 2676, 2004.

[69] C. Johnstone, W. Wan, and A. Garren, "Fixed field circular accelerator designs," in *Proceedings of the Particle Accelerator Conference*, (New York, USA), p. 3069, 1999.

[70] M. Craddock, "The rebirth of the FFAG," *CERN Courier*, vol. 6, p. 23, 2004.

[71] E. Keil, A. M. Sessler, and D. Trbojevic, "Hadron cancer therapy complex using nonscaling fixed field alternating gradient accelerator and gantry design," *Phys. Rev. ST Accel. Beams*, vol. 10, p. 054701, May 2007.

[72] F. Schmidt, *MAD-X Manual*. CERN, 2008.

[73] F. Méot, "The ray-tracing code Zgoubi," *Nuclear Instruments and Methods in Physics Research A*, vol. 427, pp. 353–356, 1999.

[74] H. A. Enge, "Effect of extented fringe fields on ion-focusing properties of deflecting magnets," *Review of Scientific Instruments*, vol. 35, no. 3, p. 278, 1964.

[75] F. Méot and S. Valero, *Zgoubi Users' Guide*. CEA Saclay, DSM/DAPNIA/SEA, January 2008.

[76] R. Baartman, "Fast crossing of betatron resonances." presented at FFAG'04 workshop, `http://www.triumf.ca/ffag2004`, 2004.

[77] S. Koscielniak and R. Baartman, "Analysis of rapid betatron resonance crossing," in *Proceedings of the Particle Accelerator Conference*, (Knoxville, USA), p. 3206, 2005.

[78] E. Keil, A. M. Sessler, and D. Trbojevic, "Three ring FFAG complex for H^+ and C^{6+} therapy," in *Proceedings of the European Particle Accelerator Conference*, (Edinburgh, Scotland), p. 1681, 2006.

[79] D. Trbojevic, "Small proton therapy accelerator by non-scaling FFAG." presented at FFAG'08 workshop, Manchester, `http://www.cockcroft.ac.uk/events/FFAG08/programme.htm`, 2008.

[80] S. L. Sheehy and D. J. Kelliher, "Effects of alignment errors in proton non-scaling FFAGs," in *Proceedings of FFAG'09, to appear in Int. J. Mod. Phys. A*, 2010.

[81] C. Johnstone and S. Koscielniak, "Tune-stabilised linear-field FFAG for carbon therapy," in *Proceedings of the European Particle Accelerator Conference*, (Edinburgh, Scotland), pp. 2290–2292, 2006.

[82] S. Machida, "Resonance crossing and dynamic aperture in nonscaling fixed field alternating gradient accelerators," *Phys. Rev. ST Accel. Beams*, vol. 11, no. 9, p. 094003, 2008.

[83] J. Kiusalaas, *Numerical methods in engineering with Python*. Cambridge University Press, 2005.

[84] S. Machida, "FFAGs for proton acceleration." presented at FFAG'08 workshop, Manchester, `http://www.cockcroft.ac.uk/events/FFAG08/programme.htm`, 2008.

[85] S. L. Sheehy, K. J. Peach, H. Witte, D. J. Kelliher, and S. Machida, "Fixed field alternating gradient accelerator with small orbit shift and tune excursion," *Phys. Rev. ST Accel. Beams*, vol. 13, no. 040101, 2010.

[86] S. L. Sheehy, K. J. Peach, H. Witte, T. Yokoi, D. J. Kelliher, and S. Machida, "PAMELA: lattice design and performance," in *Proceedings of the Particle Accelerator Conference*, (Vancouver, Canada), 2009.

[87] Wolfram Research Inc., "Wolfram Mathematica." `http://www.wolfram.com/products/mathematica/index.html`, 2010.

[88] S. Machida, "Modelling of a nonscaling FFAG and findings with the new code," in *ICFA Beam Dynamics Newsletter* (C. R. Prior, ed.), no. 43, (`http://icfa-usa.jlab.org/archive/newsletter.shtml/`), p. 54, 2007.

[89] J. Fourrier, F. Martinache, F. Méot, and J. Pasternak, "Spiral FFAG lattice design tools. Application to 6-D tracking in a proton-therapy class lattice," *Nucl. Instrum. Methods Phys. Res., Sect. A*, vol. 589, pp. 133–142, 2008.

[90] D. Wilson, I. Martin, and A. Bell, "Survey and alignment update from the Diamond Light Source," in *9th International Workshop on Accelerator Alignment*, (Menlo Park, California), p. TU009, September 2006.

[91] IAEA, "Relative biological effectiveness of ion beam therapy." IAEA Technical Report No. 461, 2008.

[92] T. Misu, Y. Iwata, A. Sugiura, S. Hojo, N. Miyahara, M. Kanazawa, T. Murakami, and S. Yamada, "Design study of compact medical fixed-field alternating-gradient accelerators," *Phys. Rev. ST Accel Beams*, vol. 7, no. 094701, 2004.

[93] H. Witte, T. Yokoi, S. Sheehy, J. Cobb, and K. Peach, "Pamela magnets - design and performance," in *Proceedings of the Particle Accelerator Conference*, (Vancouver, Canada), 2009.

[94] R. Edgecock *et al.*, "EMMA- the world's first non-scaling FFAG," in *Proceedings of the European Particle Accelerator Conference*, (Genoa, Italy), pp. 3380–3382, 2008.

[95] R. Edgecock, "EMMA - the world's first non-scaling FFAG," in *Proceedings of the Particle Accelerator Conference*, (Albuquerque, USA), pp. 2624–2626, 2007.

[96] N. Bliss *et al.*, "Technical description and status of the EMMA non-scaling FFAG," in *Proceedings of Cyclotrons and their Applications*, p. 183, 2007.

[97] R. Edgecock *et al.*, "The EMMA non-scaling FFAG," in *Proceedings of the International Particle Accelerator Conference*, (Kyoto, Japan), pp. 4266–4268, 2010.

[98] J. S. Berg, Y. Giboudot, D. J. Kelliher, S. Machida, F. Méot, B. Shepherd, and S. Tygier, "Recent developments on the EMMA on-line commissioning software," in *Proceedings of the International Particle Accelerator Conference*, (Kyoto, Japan), pp. 4325–4327, 2010.

[99] ICFA, "FFAG accelerators," in *ICFA Beam Dynamics Newsletter* (C. R. Prior and W. Chou, eds.), vol. 43, 2007.

[100] S. L. Smith, "The status of the Daresbury Energy Recoverly Linac Prototype (ERLP)," in *Proceedings of ICFA Beam Dynamics Workshop on Energy Recovery Linacs*, (Daresbury, UK), pp. 6–10, 2007.

[101] J. M. Garland, H. L. Owen, B. D. Muratori, and J. W. McKenzie, "Characterisation of the ALICE accelerator as an injector for the EMMA ns-FFAG,"

in *Proceedings of the International Particle Accelerator Conference*, (Kyoto, Japan), p. 4343, 2010.

[102] C. Beard *et al.*, "The current status of the ALICE (Accelerators and Lasers In Combined Experiments) facility," in *Proceedings of FEL'09*, (Liverpool, UK), pp. 333–335, 2009.

[103] Y. Saveliev *et al.*, "Recent developments on ALICE (Accelerators and Lasers in Combined Experiments) at Daresbury Laboratory," in *Proceedings of the International Particle Accelerator Conference*, (Kyoto, Japan), p. 2350, 2010.

[104] ASTEC, "EMMA manual." `http://projects.astec.ac.uk/EMMAManual/index.php/YAG_screens`, July 2010.

[105] A. Kalinin, R. Smith, and P. A. Macintosh, "Diagnostic system commissioning of the EMMA ns-FFAG facility at Daresbury Laboratory," in *Proceedings of the International Particle Accelerator Conference*, (Kyoto, Japan), pp. 1134–1136, 2010.

[106] A. Kalinin, "Towards sub-micrometer resolution of single shot strip line BPM," in *Proceedings of the European Particle Accelerator Conference*, (Genoa, Italy), pp. 1152–1154, 2008.

[107] A. Kalinin and S. Artinian, "Investigation of precise pipeline-type ADCs in a burst regime for a single-shot BPM," in *Proceedings of DIPAC*, (Basel, Switzerland), pp. 68–70, 2009.

[108] I. Kirkman, "private communication," July 2010.

[109] D. Garreta and J. C. Faivre, "First version of zgoubi." DPh-N, CEA-Saclay, 1972.

[110] F. Lemuet and F. Méot, "Developments in the ray-tracing code Zgoubi for 6-D multiturn tracking in FFAG rings," *Nucl. Instrum. Methods A*, vol. 547, pp. 638–651, 2005.

[111] J. S. Berg, "The EMMA main ring lattice," *Nucl. Instrum. Methods A*, vol. 596, pp. 276–284, 2008.

[112] E. Keil, "Comparison of EMMA parameter predictions," Tech. Rep. CERN-BE-2010-006, CERN, February 2010.

[113] E. Forest, F. Schmidt, and E. McIntosh, "Introduction to the Polymorphic Tracking Code," Tech. Rep. CERN-SL-2002-044, CERN, 2002.

[114] K. Peach, J. Cobb, S. Sheehy, H. Witte, T. Yokoi, *et al.*, "PAMELA overview and status," in *Proceedings of the International Particle Accelerator Conference*, (Kyoto, Japan), pp. 112–114, 2010.

[115] IBA, "IBA Cylotron Solutions." `http://www.iba-cyclotron-solutions.com/`, 2009.

[116] A. Kitagawa *et al.*, "Status report on ECR ion sources at HIMAC," *Review of Scientific Instruments*, vol. 75, no. 5, pp. 1476–1478, 2004.

[117] M. J. Easton, M. Aslaninejad, S. Jolly, and J. Pozimski, "RFQ design optimisation for PAMELA injector," in *Proceedings of the Particle Accelerator Conference*, (Vancouver, Canada), 2009.

[118] D. I. Meyer and R. Flasck, "A new configuration for a dipole magnet for use in high energy physics applications," *Nucl. Instrum. Methods*, vol. 80, no. 2, pp. 339–341, 1970.

[119] C. Goodzeit, R. Meinke, and M. Ball, "Combined function magnets using double-helix coils," in *Proceedings of the Particle Accelerator Conference*, (Albuquerque, USA), pp. 560–562, 2007.

[120] The MathWorks, "MATLAB R2009b." `http://www.mathworks.com`, September 2009.

[121] H. Witte, "private communication," January 2010.

[122] Isis innovation limited. U.K. Patent No. GB0920299.5, January 2010.

[123] T. Yokoi *et al.*, "PAMELA: development of the RF system for a non-relativistic non-scaling FFAG," in *Proceedings of the Particle Accelerator Conference*, (Vancouver, Canada), 2009.

[124] A. Seville *et al.*, "First results from the use of dual harmonic acceleration on the ISIS synchrotron," in *Proceedings of the Particle Accelerator Conference*, (Knoxville, USA), p. 1871, 2005.

[125] Ferroxcube, "Ferroxcube website." `http://www.ferroxcube.com/`, August 2010.

[126] I. Gardner, "private communication," February 2010.

[127] J. Thomason, C. Warsop, *et al.*, "A 300 μA Upgrade for the ISIS accelerator," *Neutron News*, vol. 15, no. 2, pp. 13–16, 2004.

[128] T. Yokoi, K. Peach, and H. Witte, "Beam extraction in PAMELA NS-FFAG," in *Proceedings of the International Particle Accelerator Conference*, (Kyoto, Japan), pp. 567–569, 2010.

[129] K. Peach and H. Witte, "private communication," August 2010.

[130] R. Fenning *et al.*, "A non-scaling FFAG gantry design for the PAMELA project," in *Proceedings of the International Particle Accelerator Conference*, (Kyoto, Japan), pp. 4593–4595, 2010.

[131] R. Fenning *et al.*, "An FFAG transport line for the PAMELA project," in *Proceedings of the Particle Accelerator Conference*, (Vancouver, Canada), 2009.

[132] S. Machida and R. Fenning, "Beam transport line with scaling fixed field alternating gradient type magnets," *Phys. Rev. ST Accel. Beams*, vol. 13, no. 084001, 2010.

[133] R. Fenning and S. Machida, "private communication," August 2010.

[134] A. Johnson, "The experimental physics and industrial control system website." `http://www.aps.anl.gov/epics`, September 2010.